# CONTROLLED-SOURCE ELECTROMAGNETICS FOR RESERVOIR MONITORING ON LAND

# CONTROLLED-SOURCE ELECTROMAGNETICS FOR RESERVOIR MONITORING ON LAND

PROEFSCHRIFT

ter verkrijging van de graad van doctor
aan de Technische Universiteit Delft,
op gezag van de Rector Magnificus prof. ir. K.C.A.M. Luyben,
voorzitter van het College voor Promoties,
in het openbaar te verdedigen
op woensdag 22 februari 2012 om 10.00 uur

door

**Marwan WIRIANTO**

Magister Sains Matematika,
Institut Teknologi Bandung, Indonesië

geboren te Jakarta, Indonesië

Dit proefschrift is goedgekeurd door de promotoren:
Prof.dr. W.A. Mulder
Prof.dr.ir. E.C. Slob

Samenstelling promotiecommissie:

| | |
|---|---|
| Rector Magnificus | voorzitter |
| Prof.dr. W.A. Mulder | Technische Universiteit Delft, promotor |
| Prof.dr.ir. E.C. Slob | Technische Universiteit Delft, promotor |
| Prof.dr.ir. A. Gisolf | Technische Universiteit Delft |
| Prof.dr.ir. C. Vuik | Technische Universiteit Delft |
| Prof.dr.ir. P.M. van den Berg | Technische Universiteit Delft |
| Prof.dr. R.J. Arts | TNO |
| Dr. M. Darnet | Nederlandse Aardolie Maatschappij B.V. |

*This thesis is dedicated to*
*Gérard C. Herman (1954–2006)*

# Contents

# 1 **Introduction**

In order to assess the hydrocarbon content of potential reservoirs, an image of the subsurface is needed that indicates the chemical nature of the substances in the reservoir. The controlled-source electromagnetic (CSEM) method is one of the tools for obtaining these images. CSEM data can provide resistivity maps of the subsurface. Because the bulk resistivity depends on the pore fluid resistivity, these maps may enable us to estimate the nature of the fluid content in the reservoir. The method was introduced initially to study resistivity of the oceanic lithosphere for environmental purposes. Nowadays, the exploration of oil and gas is the most common application of the CSEM method. In this thesis, we also consider the potential of the CSEM method for monitoring a hydrocarbon reservoir during production.

## 1.1   INTRODUCTION TO THE CSEM METHOD

To appreciate the value of the CSEM method for hydrocarbon exploration, it should be positioned relative to the seismic method, which is the mainstream geophysical tool in the oil and gas industry for obtaining images of the subsurface.

The seismic method employs elastic or acoustic waves to delineate boundaries between materials with different seismic properties (Yilmaz, 2001). One measures the time required for a seismic pulse to reach the surface after reflection from boundaries between lithologic units. Variations in these reflection times, recorded on the surface, are then processed to map the reflection events to boundaries at depth. Usually, a quantitative interpretation is further carried out on the amplitude of the imaged data to estimate the seismic velocity and density at potential targets (Gisolf and Verschuur, 2010). In this way, the seismic method can provide the structural features of the strata below in detail.

However, the seismic method has difficulty distinguishing the nature of the fluid content in the host rocks. The reason is the low sensitivity of the seismic velocity and density to variations in fluid saturation (Castagna and Backus, 1993; Debski and Tarantola, 1995; Plessix and Bork, 2000). A porosity greater than 30% is required to have a significant velocity difference between a water- and hydrocarbon-saturated reservoir. Although with high quality seismic data and sophisticated seismic inversion saturation effects can sometimes be observed, the uncertainty is usually high. It is obvious that we should look for additional data

sets to complement the seismic method, such that we know before drilling whether the target reservoirs contain commercial quantities of hydrocarbons or not. One option is a controlled-source electromagnetic (CSEM) data set.

In geophysical applications, CSEM data directly respond to the resistivity of host rocks. This fact has at least two advantages. Firstly, because the bulk resistivity depends on the resistivity of the pore fluid (Archie, 1942), these data may enable us to estimate the nature of the fluid content in the host rocks. Secondly, the resistivity of rocks evidently has a high sensitivity to the variations in fluid saturation. When the pore fluid within a host rock varies gradually between water and hydrocarbons, the resistivity values of the rock change significantly. Although other physical properties of the rock also change, the resistivity is most affected. As an example, Figure 1.1 shows that the resistivity difference between hydrocarbons-saturated and saline-water-saturated rock is as much as two orders of magnitude, while it has little effect on acoustic impedance. These effects have made the CSEM method a valuable complement to the seismic method.
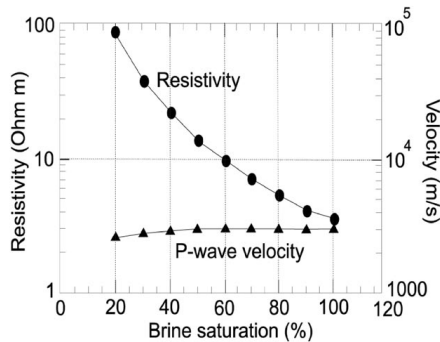


**Fig. 1.1**    Variation of resistivity and P-velocity with respect to brine saturation for a sandstone core. (after Wilt and Alumbaugh, 1998)

## 1.2    OVERVIEW OF THE CSEM METHOD

The CSEM method is primarily used to determine the resistivity distribution of the subsurface. The method measures the time-varying Earth response excited by a source current. Then follows a combination of preprocessing, forward modelling, hypothesis testing, and inversion to extract the resistivity of targets from the data. Understanding how CSEM data are acquired and processed is essential to better exploit the method and to help the interpretation. In this section, we present a brief review of typical acquisition and processing of CSEM data. No attempt is made to review all the advancements in CSEM technology

for hydrocarbon applications. For this, we refer the reader to Ward and Hohmann (1987), Avdeev (2005), Edwards (2005), Constable and Srnka (2007), Constable (2010), Zhdanov (2010), Börner (2010), and the references cited therein.

### 1.2.1 CSEM Acquisition

Acquisitions with the CSEM method can principally be divided into frequency-domain (FDEM) and time-domain (TDEM) systems. In FDEM systems, we measure electromagnetic signals generated by a periodic, alternating source current that employs one or a few frequencies (typically between 0.1 and 10 Hz). In TDEM systems, we measure electromagnetic signals induced by a certain combination of step-on or step-off source currents, repeated several times and stacked together to improve the signal-to-noise ratio. TDEM systems are also widely known as transient EM (TEM) systems.
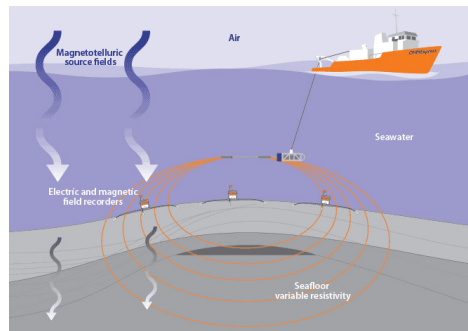


**Fig. 1.2**    Schematic diagram of a typical marine CSEM survey. A mobile horizontal electric dipole (HED) is used as a source, emitting a periodic, alternating source current that operates with a frequency between 0.1 and 10 Hz. This source is towed 20 to 40 m above the seabed to maximize the energy that couples to the seafloor rocks and sediments and minimize coupling with the air. An array of stationary multi-channel EM receivers, deployed on the sea bottom and spaced at various ranges, records the time-varying source signal. Typically, these receivers include one or two pairs of orthogonal electric sensors and one or two pairs of magnetic sensors. (Image obtained from `www.ohmsurveys.com`)

Typical operations with the FDEM and TDEM method are depicted in Figures 1.2 and 1.3, respectively. FDEM systems are preferably used in deep-marine environments, with a water depth of at least 300 m, where the thick layer of sea water effectively shields the measurements from EM noise present at the surface, whereas TDEM systems are more appropriate in shallow water and on land because of the much stronger EM noise. Nevertheless, both techniques can be carried out either for marine or land applications.
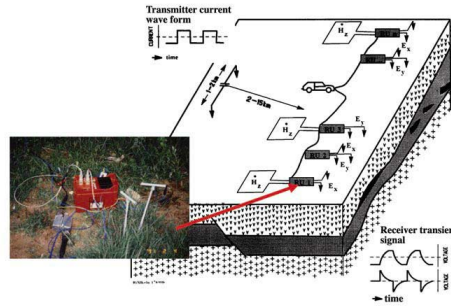
**Fig. 1.3**    Schematic diagram of a land EM survey. A dipole electrode source is buried just below the surface, while an array of multi-channel receivers are placed on the surface, or sometimes in a well. The source employs a high-powered direct current that is suddenly switched on or off. In this way, the field resulting from the source induces a current in the receiver coil and in the earth. The response of the earth also induces an electric current in the receiver sensors. Measurements are typically taken during the off-time, repeated several times, and summed up to increase the signal-to-noise ratio. (Image taken from `www.kmstechnologies.com`)

Regardless of the acquisition systems, the main principle exploited in CSEM methods for exploration is the fact that hydrocarbon-saturated reservoirs are typically 5 to 100 times more resistive than the host sediments. Their presence causes the electromagnetic energy to be reflected. It then diffuses back to the receivers at the sea bottom or on the land surface, where it can be detected as an anomalous signal in addition to the background signal passing through the host sediments. Practically, the presence of anomalous bodies is usually determined by comparing data at large source-receiver distances to reference data, measured in a nearby area or computed for an accurate background model without those bodies.

Nowadays, various CSEM acquisition systems exist. For land applications, they include, for instance, long-offset TEM (LOTEM) (Strack, 1992), Circular Electrical Dipole (CED) (Mogilatov and Balashov, 1996), multi-channel TEM (MTEM) (Wright *et al.*, 2002), and focused-source EM (FSEM) (Davydycheva *et al.*, 2006; Davydycheva and Rykhlinski, 2009). For marine applications, Edwards (2005) reported some variants of the CSEM method. They use uncommon source configurations, namely, vertical electric and horizontal magnetic dipoles. These sources are in particular used to overcome the so-called airwave. The latter is the electromagnetic field that propagates in the air with the speed of light and almost without any attenuation. The airwave appears as the predominant signal, suppressing the subsurface signals, and therefore requires careful treatment.

Although each method acquires data in a different way, they all share the same characteristic of working in a regime where the propagating part of the EM fields has a negligible contribution to the total field. The resulting fields are primarily dominated by the dissipative part, the diffusive electromagnetic field. Consequently, resolution with these methods will always be poor compared to what can be obtained with the seismic reflection method (Løseth *et al.*, 2006; Constable, 2010).

### 1.2.2 EM Modelling

Once data have been acquired, the geophysicist should be able to draw conclusions from these data about the resistivity distribution in the subsurface. The reconstruction usually involves a 'trial-and-error' process, finding the best model that explains the data. This can be achieved only if we have an efficient modeling algorithm.

Since early 1990's, important progress in EM modelling has been made for accurately solving Maxwell's equations (see Avdeev, 2005; Börner, 2010, and the references listed therein). These authors employed a finite-difference, finite-volume, finite-element, or an integral-equation method. Each approach has his advantages and disadvantages. Finite-difference and the closely related finite-volume methods are the easiest to grasp and relatively straightforward to implement, but numerical accuracy requires dense grids, affecting the memory requirements and computation time. Finite-element methods on unstructured grids allow for better gridding near sharp contrast, but have a larger overhead and may result in a large sparse linear system that is more difficult to solve. Integral-equation methods have the advantage over finite-difference or finite-element methods that they restrict the computational domain to the domain of scatterer, but the matrices arising in these methods are always full and more costly to solve.

### 1.3 RESEARCH CHALLENGES

### 1.3.1 Motivation for EM monitoring

Marine CSEM surveying, as used today for hydrocarbon exploration, is not a new technology. The method was originally developed by the Scripps Institution of Oceanography (Cox, 1981; Cox *et al.*, 1986; Constable *et al.*, 1987; Evans *et al.*, 1991), the University of Toronto (Edwards and Chave, 1986; Cheesman *et al.*, 1987), and the University of Cambridge (later Southampton) (MacGregor and Sinha, 2000). On land, CSEM surveys have even a longer history and have been carried out in, for instance, Russia, China, and India (see Spies, 1983;

Strack, 1992; Strack and Vozoff, 1996; Wright *et al.*, 2002; He *et al.*, 2007; Strack and Pandey, 2007). However, it was just after the success of a pilot CSEM experiment for detecting thin resistive hydrocarbon reservoirs located off-shore Angola (Ellingsrud *et al.*, 2002), that the CSEM method received more and more attention from the oil and gas industry. Now, more than 10 years after the Angola field-test survey, the CSEM method has established its position as an exploration tool next to seismic (Eidesmo *et al.*, 2002; Darnet *et al.*, 2007; MacGregor *et al.*, 2007).

Given the fact that it directly responds to resistivity of the subsurface, the CSEM method has a potential for monitoring a hydrocarbon reservoir during the recovery process. Water flooding or steam injection for oil production creates resistivity changes and these changes can potentially be detected by time-lapse CSEM measurements. Moreover, the presence of seismic and well information, usually obtained at the early stages of production, makes the monitoring problem well suited for CSEM technology, because a background resistivity model can be generated from an interpretation of the available seismic and well data (MacGregor and Cooper, 2010).

### 1.3.2   Research Objectives

These considerations led us to further investigate the EM monitoring problem. We tried to answer two questions: are the time-lapse changes in the reservoir detectable, particularly in the presence of noise, and if so, could we use time-lapse signals to locate where the time-lapse changes happened in the subsurface? In EM, spatial resolution will always be poor due to the diffusive character of EM signals in the earth at the low frequencies required to reach sufficient depth. However, EM measurements are more sensitive to fluid properties than seismic measurements, especially when comparing highly resistive oil to low-resistivity brine.

### 1.4   OUTLINE OF THIS THESIS

This thesis consists of two parts. The first part covers several aspects of numerical modelling, namely, finding an efficient time-domain EM (TDEM or TEM) modelling approach, investigating the effect of time-weighting on time-domain inversion, and applying an alternative interpolation method to obtain recorded electromagnetic response near strong resistivity contrasts. The second part discusses an application of the CSEM method. Here, we focus on using CSEM as a tool for hydrocarbon reservoir monitoring during production.

In more detail, the outline of this thesis can be summarized as follows.

The current chapter, **Chapter 1**, serves as an introduction to the subject of electromagnetics and as a motivation for our research.

In **Chapter 2** we review a number of numerical time-domain electromagnetic (TEM) modelling. We employ complexity analysis, measuring the computational cost in terms of the number of unknowns, to compare the computational cost of different methods.

In **Chapter 3**, we investigate the effect of time-weighting on the time-domain EM inversion. The motivation for this work was an apparent thought among EM practitioners in the geophysical community who commonly agree that the early time of transient EM data carries no information about deeper targets. In this chapter, we show that simply muting the early-time time-domain EM data may lead to unsatisfactory inversion results.

In **Chapter 4,** we present an alternative interpolation of modelled EM responses. The motivation was the fact that, near sharp resistivity contrasts, the field component perpendicular to the interface that separates the two resistivities is discontinuous and a tri-linear interpolation scheme may lead to large errors in that case. We propose to use the essentially non-oscillatory (ENO), piecewise polynomial interpolation scheme, designed for piecewise smooth functions that contain discontinuities in the function itself or in its first or higher derivatives.

In **Chapter 5**, we investigate the feasibility of using the CSEM method for monitoring changes in the subsurface. We considered land CSEM for a deeper target with oil and brine in a complex 3D resistivity model.

In **Chapter 6**, we carried out numerical experiments to understand how to optimize the acquisition to best capture the time-lapse signal.

In **Chapter 7**, we propose a simple and effective method to remove the primary airwave from the data, which we call 'partial airwave removal'. The idea of the removal was motivated by the fact that the airwave will still provide sufficient illumination of the target at larger distances. The repeatability errors in the primary airwave, however, can destroy the signal-to-noise ratio of the time-lapse data. Thus, we need a method that can reduce or remove the contribution due to the primary airwave generated by the source, while maintaining the part of the airwave that is transmitted into the ground.

While our results in Chapters 5, 6, and 7 indicate that the time-lapse difference of electromagnetics fields can reveal the outline on the surface of the resistivity changes in a hydrocarbon reservoir under production, direct interpretation of time-lapse difference data set can be difficult because the resistivity structure may be quite complex. Applying EM inversion for time-lapse data may provide better results. In **Chapter 8**, we investigate if non-linear inversion can use time-lapse responses to characterize the subsurface resistivity changes.

The chapter titled **Conclusion and Future outlook** summarizes conclusions about the forward modelling method and the electromagnetic monitoring problem. It also provides recommendations on the possible extension of the current results.

This thesis comprises several published papers. These were slightly modified to be more consistent with the notation and language in the rest of the document.

# Part I

# Numerical EM Modelling

# 2 Time-domain modeling of electromagnetic diffusion with a frequency-domain code

**SUMMARY**

We modeled time-domain electromagnetics (TDEM) measurements of induction currents for marine and land applications with a frequency domain code. An analysis of the computational complexity of a number of numerical methods shows that frequency-domain modeling followed by a Fourier transform is an attractive choice if a sufficiently powerful solver is available. A recently developed, robust multigrid solver meets this requirement. An interpolation criterion determined the automatic selection of frequencies. The skin depth controlled the construction of the computational grid at each frequency. Tests of the method against exact solutions for some simple problems and a realistic marine example demonstrate that a limited number of frequencies suffice to provide time-domain solutions after piecewise-cubic Hermite interpolation and a fast Fourier transform.

## 2.1  INTRODUCTION

Controlled-source EM measurements of induction currents in the earth can provide resistivity maps for geophysical prospecting. In marine environments, the current source often uses one or a few frequencies. In shallow seawater or on land, the response of air is dominant, and time-domain measurements are more appropriate. Because EM signals in the earth are strongly diffusive, direct interpretation of measured data can be difficult. Inversion of the data for a resistivity model may provide better results. We therefore need an efficient modeling and inversion algorithm.

For time-domain modeling, there is a number of options. The simplest one uses explicit time stepping, but this is rather costly. The Du Fort-Frankel (1953) method is more efficient, but it involves an artificial light-speed term. Implicit methods can compete only if a fast solver is available. Haber *et al.* (2002, 2004) provide examples for time-domain modeling. Druskin and Knizhnerman (1994) propose a technique based on Lanczos reduction and matrix exponentials. Obviously, the Fourier transform of results from a frequency domain code can also provide time-domain solutions. Newman *et al.* (1986) present examples for horizontally layered media. For general resistivity models, a finite-difference, finite-volume, or finite-element discretization of the governing equations requires an efficient solver. The multigrid method (Mulder, 2006, 2008) allows for a reasonably fast solution of the discretized equations when used as a preconditioner for BiCGStab2 (van der Vorst, 1992; Gutknecht, 1993), a conjugate-gradient iterative method. With stronger grid stretching, we can apply a more robust multigrid variant based on semicoarsening and line relaxation (Mulder, 2007).

Here we compare the computational cost of these methods by complexity analysis. The complexity of an algorithm measures its computational cost in terms of the number of unknowns — in this case, the electric field components on a grid. Because it ignores the constants that define the actual run time of a code on a computer, complexity analysis provides a crude way of comparing algorithms. Our analysis suggests that the frequency-domain approach is attractive. Next, we describe the issues arising when using a frequency domain code for time-domain modeling. These involve the choice of frequencies, the choice of the discretization grid at each frequency, interpolation of earlier results to obtain a good initial guess and thereby accelerate the convergence of the solution, and the need for a robust solver. We present a number of examples to illustrate the method's performance.

## 2.2 COMPUTATIONAL COMPLEXITY

There are various methods for the numerical modeling of transient electromagnetic signals. Here we consider an explicit time-stepping scheme, the Du Fort-Frankel method, implicit schemes, matrix exponentials and Lanczos reduction, and the Fourier transform of frequency-domain solutions. Complexity analysis provides a cost estimate of a numerical method in terms of the number of unknowns, without the constants that determine the actual computer run-time. If $N$ is the number of unknowns, the required computer time can be expressed as $Cf(N)$, where $f(N)$ describes the dependence on the number of unknowns. The constant $C$ is primarily determined by the algorithm, but also by its implementation and by the specific hardware. The determination of the constant $C$ requires tedious counting of operations. Alternatively, we can determine the constant by implementing the algorithm and running the code. Complexity analysis derives an expression for $f(N)$ and can serve as a crude tool to distinguish between the cost of various algorithms. However, there are algorithms that have a very bad $f(N)$ but still perform very well on practical problems. A well-known example is Dantzig's 1947 simplex algorithm (Dantzig, 1963) for linear-programming problems, which has an exponential complexity with $f(N) = O(2^N)$, but still is quite efficient in many cases.

Here, we review the complexity of various time-domain methods for a 3D problem with $N = O(n^3)$ unknowns, where $n$ is the number of grid points in each coordinate. An explicit time-stepping scheme is the simplest to implement. Unfortunately, it is only stable if the time step $\Delta t \leq ch^2$, where $c$ is a constant depending on the material properties and the discretization, and $h$ is the smallest grid spacing used in the problem. We assume that $h = O(1/n)$. The cost of a single time step is $O(n^3)$, so the overall complexity for computing the solution over a given, fixed time span $T$ is $(T/\Delta t)O(n^3) = O(n^5)$. In practice, this is too slow for practical purposes, except perhaps on massively parallel computers.

The Du Fort-Frankel (1953) method offers one way to get around the restrictive stability limit. An artificial light speed is introduced with size $h/(\Delta t\sqrt{2})$ that allows the time step to grow with the square root of time, without doing too much harm to the accuracy of the solution. Geophysical applications of this method to time-domain electromagnetic problems can be found in, for instance, papers by Oristaglio and Hohmann (1984) for the 2D case and Wang and Hohmann (1993) and Commer and Newman (2004) for 3D problems. Maaø (2007) presents an interesting variant. The cost of the Du Fort-Frankel method is of $O(n^4)$, as shown in the appendix.

An implicit scheme can avoid the $O(h^2)$ stability limit as well. The price paid is

the solution of a large sparse linear system, which may be costly. With a sufficiently powerful solver, one or a few iterations can be enough (Haber *et al.*, 2002, 2004). For $O(n^0) = O(1)$ iterations, the cost of solving the time-domain equations is $O(n^3)$ per time step. Together with a time step that scales with the square root of time, this method has the same complexity as the Du Fort-Frankel scheme, although the cost per step will be larger by at least an order of magnitude because of the work required by the iterative solver. The method does not require an artificial light-speed term, which may allow for larger time steps without harming the accuracy.

Druskin and Knizhnerman (1994) and Druskin *et al.* (1999) proposed a technique that appears to be attractive for 3D applications. The Lanczos method was applied to reduce the original sparse matrix **A** that describes the linear problem to a dense but much smaller matrix. The latter was used to quickly compute the time evolution using matrix exponentials. Remis (1998) investigated this method in his PhD thesis.

The Lanczos method constructs the small matrix iteratively. Druskin and Knizhnerman (1994) show that accurate results can be obtained by performing $m$ iterations, where $m = O(n\sqrt{T \log n})$. As before, $T$ is the length of time for which the solution needs to be computed, and $n$ is the number of grid points in one of the spatial coordinates. Because the number of non-zero elements of **A** for a 3D problem is $O(n^3)$, the cost of the Lanczos decomposition will be of order $n^4\sqrt{\log n}$ for a given time span $T$.

One can compute time-domain solutions by first selecting a number of frequencies, then solving the frequency-domain problem at those frequencies, and finally performing an inverse Fourier transform to the time domain. For $n_f$ frequencies and assuming the availability of an efficient solver that requires $O(1)$ iterations, the complexity is $O(n_f n^3)$.

Comparison of the above methods shows that two of them have an asymptotic complexity of $O(n^4)$: the Du Fort-Frankel method and an implicit scheme with an optimal solver that convergences in $O(1)$ iterations. The method based on Lanczos reduction has an additional logarithmic factor, which in practical applications may be small enough to be neglected. The application of a frequency-domain method with an optimal solver results in a complexity of $O(n_f n^3)$, which can be favorable if $n_f$ is small relative to $n$.

These are only asymptotic results. In practice, the performance will depend on the details of the implementation and the actual constants in the complexity estimates.

The choice of grid is another topic. Diffusion problems typically have length scaling with the square root of time. This implies that accurate modeling of a

problem with a point-like source in space and time requires an initial grid that is very fine close to the source and gradually becomes less fine. Dynamic local adaptive grid refinement will accomplish this, but leads to complicated software. Also, the Lanczos decomposition cannot be used with dynamic adaptive grid refinement. In the Fourier domain, the computational grid should depend on the skin depth and therefore on the frequency (Plessix *et al.*, 2007). Each frequency requires a different grid, but that is easier accomplished than time-dependent adaptive local grid refinement.

Although it remains to be seen which of the four methods requires the least computer time for a given accuracy, the frequency-domain approach appears to be attractive. Next, we discuss some aspects of the method.

## 2.3  METHOD

We summarize the governing equations and their discretization. Next, we review the multigrid solver (Mulder, 2006, 2008). Because the standard approach breaks down on stretched grids, a variant based on semi-coarsening and line relaxation was designed (Jönsthövel *et al.*, 2006; Mulder, 2007). The version in the earlier paper (Jönsthövel *et al.*, 2006) was slow. Here, we describe the acceleration of the line relaxation by a non-standard Cholesky decomposition. Then, we describe the automatic selection of frequencies, followed by a discussion on how the skin depth at each frequency determines the computational grid.

The Maxwell equations and Ohm's law for conducting media in the frequency domain are

$$\imath\omega\mu_0\tilde{\sigma}\hat{\mathbf{E}} - \nabla \times \mu_r^{-1}\nabla \times \hat{\mathbf{E}} = -\imath\omega\mu_0\hat{\mathbf{J}}_s. \qquad (2.1)$$

The vector $\hat{\mathbf{E}}(\omega, \mathbf{x})$ represents the electric field components as a function of angular frequency $\omega$ and position $\mathbf{x}$. The current source is $\hat{\mathbf{J}}_s(\omega, \mathbf{x})$. The quantity $\tilde{\sigma}(\mathbf{x}) = \sigma - \imath\omega\varepsilon_0\varepsilon_r$, with $\sigma(\mathbf{x})$ the conductivity, $\varepsilon_r(\mathbf{x})$ the relative permittivity, $\mu_r(\mathbf{x})$ the relative permeability, and $\varepsilon_0$ and $\mu_0$ their absolute values in vacuum. We adopt the Fourier convention

$$\mathbf{E}(t, \mathbf{x}) = \frac{1}{2\pi} \int_{-\infty}^{\infty} \hat{\mathbf{E}}(\omega, \mathbf{x})e^{-\imath\omega t}d\omega.$$

We will use SI units in the examples.

Mulder (2006, 2008) presented a numerical method for solving the system of equations 2.1 in the frequency domain. The Finite-Integration Technique (Weiland, 1977) provided a finite-volume discretization of the equations. A multigrid solver acted as preconditioner for the iterative BiCGStab2 scheme (van der Vorst,

1992; Gutknecht, 1993). On an equidistant grid, the method converged in a fixed number of steps, independent of the number of grid points. With grid stretching, however, we lost this $O(1)$ number of iterations. The more severe the stretching, the larger the number of iterations. Also, this number increased for a larger number of grid points. The grid stretching is necessary because we have to include artificial boundaries when we truncate the computational domain to a finite size.

The use of semi-coarsening and line relaxation led to a more robust solver (Jönsthövel *et al.*, 2006). During a single multigrid cycle, the grid was only coarsened in two of the three coordinate directions. We applied the line relaxation in the same two directions. The direction that was not coarsened alternated among the three coordinate directions between subsequent multigrid cycles. We always applied three multigrid cycles as a single preconditioning step for BiCGStab2 to ensure the invariance of the preconditioner. For the results in that paper, we used a generic subroutine for solving complex-valued band matrices. Here, we replaced this routine by a non-standard Cholesky decomposition.

The standard decomposition factors a hermitian matrix $\mathbf{A}$ into $\mathbf{LL}^{\mathsf{H}}$, where $\mathbf{L}$ is a lower triangular matrix and $\mathbf{L}^{\mathsf{H}}$ is its complex conjugate transpose. In our case, the Finite Integration Technique provides a matrix $\mathbf{A}$ that is not hermitian but complex-valued and symmetric: $\mathbf{A} = \mathbf{A}^{\mathsf{T}}$, where the superscript $^{\mathsf{T}}$ denotes the transpose. The non-standard Cholesky decomposition factors the matrix into $\mathbf{LL}^{\mathsf{T}}$. In the line relaxation scheme, the matrix $\mathbf{A}$ is a band matrix with eleven diagonals. We only need its main diagonal and five lower diagonal elements. The Cholesky decomposition replaces this matrix by $\mathbf{L}$, also containing six diagonals. We found a speed-up by a factor of about 7 after replacing the generic band matrix solver by the non-standard Cholesky decomposition.

Here, we used the simpler solver if the grid stretching was mild and the more robust solver if the grid stretching was more severe. On equidistant or mildly stretched grids, the number of BiCGStab2 iterations required to solve the equations at a given frequency is typically around four with the standard multigrid method, independent of the number of unknowns. One BiCGStab2 iteration involves two multigrid preconditioning steps. The more powerful method based on semi-coarsening and line-relaxation is less sensitive to grid stretching but the required computer time per full BiCGStab2 iteration is almost 11 times larger. The number of BiCGStab2 iterations is typically around two. One iteration now involves two preconditioning steps consisting of a total of 6 multigrid cycles.

The time-domain solutions require a large number of frequencies. We chose an adaptive approach. Following, for instance, Newman *et al.* (1986) and Gupta *et al.* (1989), we selected frequencies $f_k$ on a logarithmic grid: $f_k = 10^{q_k}$, with
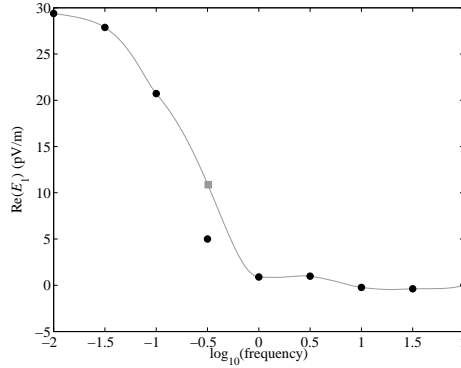
**Fig. 2.1** Example displaying the adaptive selection of frequencies. The black dots represent the real part of the horizontal component of the electric field at a given receiver for an equidistant grid of $q = \log_{10} f$ between $-2$ and $2$ with spacing $\Delta q = 0.5$ ($f$ is the frequency in Hz). We can remove one point, here at $q = -0.5$, and predict its value by shape-preserving piecewise-cubic Hermite interpolation through the remaining points. If the difference between the interpolated and actual value is too large, we add two new frequencies by selecting $q = -0.5 \pm \frac{1}{2}\Delta q$, in this case $q = -0.75$ and $q = -0.25$.

$q_k = q_0 + k\Delta q$, $k = 0, \ldots, n_f - 1$. The frequency-domain solutions provided the electric field components at the receivers. Shape-preserving piecewise-cubic Hermite interpolation (Fritsch and Carlson, 1980) mapped these data points to an equidistant grid of frequencies. A fast Fourier transform provided the response in the time domain.

Instead of using an equidistant grid of values for $q_k$, an adaptive selection of values will reduce the required computer time. Given a minimum and maximum frequency $f_{\min}$ and $f_{\max}$, we chose values of $q = q_0 + m\Delta q^{(0)}$, $m = 0, \ldots, M-1$, where $q_0 = \log_{10} f_{\min}$ and $\Delta q^{(0)} = (M-1)^{-1}\log_{10}(f_{\max}/f_{\min})$. We then computed the solutions for these $M$ frequencies and stored them on disk. This included both the full solutions on the computational grid and the recorded electric field components at the receivers. Next, we selected frequencies at an interval $\frac{1}{2}\Delta q^{(0)}$ in an adaptive manner.

Figure 2.1 serves as an example to explain one step of the adaptive frequency-selection procedure. The dots represent the real part of the computed electric field component in the $x$-direction. Suppose we have results for $q = -2$ to $2$ at an interval of $\Delta q = 0.5$. We remove one point, for instance at $q = -0.5$, and perform shape-preserving piecewise-cubic Hermite interpolation through the remaining points, resulting in the gray curve in Figure 2.1. The value at $q = -0.5$, marked by the square, is different from the actual value indicated by the dot.

If the difference exceeds a certain threshold, for instance 1% of the maximum absolute value in the plot, we select values of $q$ for the next finer level with $\Delta q = 0.25$ on the left and on the right side of $q = -0.5$, so at $q = -0.75$ and $q = -0.25$. We repeat this procedure for the real and imaginary part of all electric field components at all receivers for all values of $q = -1.5, -1.0, \ldots, 1.0, 1.5$ of the original set, excluding end points. This will produce a set of new $q$-values on a grid with spacing $\Delta q = 0.25$. We then solve the problem at those frequencies. Then, new frequencies are selected in the same way as before to find $q$-values on a grid with a spacing $\Delta q = 0.125$. We repeat this process until the differences between interpolated and computed values are smaller than the given tolerance.

To describe this procedure in a general way, we define $\Delta q^{(l)} = \Delta q^{(0)}/2^l$, $l = 1, 2, \ldots, l_{\max}$. Suppose we move to a new level $l$ and previously obtained solutions at smaller values of $l$ are available on disk. We select an existing solution at some frequency defined by $q_m^{(l')}$, $l' < l$, and determine a prediction for the receiver data by shape-preserving piecewise-cubic Hermite interpolation based on the frequencies $10^q$ rather than $q$ itself. For this interpolation, we exclude the result at $q_m^{(l')}$. If the difference between the interpolated and actual value exceeds a prescribed tolerance, we select the two neighboring frequencies at $q_m(l') \pm \Delta q^{(l)}$, except at the end points where only the one inside the defined range of $q$ is taken. In this way, we find a number of frequencies on level $l$ and then compute solutions for these frequencies.

We could reduce the number of iterations for the frequency-domain method by determining an initial guess based on cubic Lagrange interpolation from existing solutions at the four nearest frequencies. Here 'nearest' refers to distance on a logarithm scale. If solutions for less than four frequencies were available, we switched to lower-order interpolation.

The physics of the problem dictate that at high frequencies, only a small portion of the earth affects the recorded electric field, whereas at lower frequencies, a larger part of the earth is seen. The length scale at a frequency $f$ is controlled by the skin depth $\Delta_s = 1/\sqrt{\pi f \mu \sigma}$, where $\sigma$ is the conductivity and $\mu$ the magnetic permeability. If we take the vacuum value $\mu_0 = 4\pi \times 10^{-7}$ H/m for the latter, we obtain the well-known expression $\Delta_s = 503/\sqrt{\sigma f}$, all in SI units.

Several conflicting requirements guide the choice of the grid (Plessix *et al.*, 2007). First, numerical accuracy requires three to eight points per skin depth. Second, the grid should be sufficiently fine to honor the details of the resistivity model close to the source and the receivers. Third, a point-dipole or finite-length line source generates a singular solution. For receivers at a short distance from the source, the singularity must be resolved with sufficient accuracy, requiring a fine

grid. For receivers further away, the solution can have sufficient accuracy without resolving the details of the singularity, thereby requiring a less fine grid around the source. Finally, as we use perfect electric conductor boundary conditions, a boundary strip of about five skin depths is added around the model to avoid undesirable boundary effects. For the air layer, an even thicker layer is added.

The well-known primary-secondary formulation may offer an advantage in some cases. If we abbreviate Equation 2.1 as $\mathbf{L}\hat{\mathbf{E}} = \hat{\mathbf{f}}$, we can split the linear operator into $\mathbf{L} = \mathbf{L}_p + \mathbf{L}_s$ and the solution into $\hat{\mathbf{E}} = \hat{\mathbf{E}}_p + \hat{\mathbf{E}}_s$ such that $\mathbf{L}_p\hat{\mathbf{E}}_p = f$ and $\mathbf{L}_p$ can be easily solved. The secondary solution then should obey $\mathbf{L}\hat{\mathbf{E}}_s = -\mathbf{L}_s\hat{\mathbf{E}}_p$. If the secondary problem has the same relative magnetic permeability as the primary problem, then $\mathbf{L}_s = \imath\omega\mu_0(\tilde{\sigma} - \tilde{\sigma}_0)$. The secondary problem is as difficult to solve as the original one, but the advantage is a potentially more accurate solution. If the source resembles a delta function, the solution will be singular close to the source. If a receiver is located close to the source, a rather fine grid is required to resolve the singular behavior of the electric field. If the formation has a conductivity $\tilde{\sigma}_0$ around the source and $\mathbf{L}_s = \imath\omega\mu_0(\tilde{\sigma} - \tilde{\sigma}_0)$ is non-zero sufficiently far away from the source and does not have the character of an isolated point scatterer, the secondary field will generally be less singular. In that case, we can use a different grid that does not require very small cells close to the secondary source.

## 2.4  EXAMPLES

Here we present examples that highlight some of the issues.

### 2.4.1  Homogeneous formation

The first example is a point-current source $\mathbf{J}_s = \mathbf{j}_s\delta(\mathbf{x}, t)$, $\mathbf{j}_s = (1, 0, 0)^\mathsf{T}$ Ams, in a homogeneous formation with a conductivity of $\sigma = 1$ S/m. We computed frequency-domain solutions on a grid that was adapted to the skin depth and finest near the source. We applied power-law grid stretching (Mulder, 2006) away from the source. The grid was different for each frequency. The BiCGStab2 iterations stopped as soon as the norm of the residual dropped below $10^{-6}$ times the norm of the residual obtained for a zero electric field. Figure 2.2 shows the real and imaginary parts of $E_1$, the $x$-component of the electric field, measured by a single receiver at 900 m distance from the source at the same depth. The computational grid had $128^3$ cells. First, we computed solutions at five frequencies $f = 10^q$ Hz, with $q = -2, -1, 0, 1, 2$, so $\Delta q = 1$. We set the initial values for the electric fields to zero. Next, the computed values of the electric field recorded
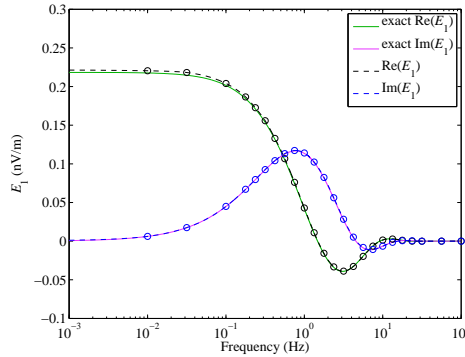
**Fig. 2.2**   Real (black) and imaginary (blue) part of $E_1$ for various frequencies. The
circles indicate the computed values, the lines were determined by shape-
preserving piecewise-cubic interpolation. The real and imaginary parts of the
exact solution are drawn as well.

at the receiver for each frequency $f_m$ were compared to a prediction based on
piecewise-cubic Hermite interpolation using the values at the other frequencies $f_k$
and excluding the one for which the prediction was made ($k \neq m$). If the relative
difference between the interpolated and actual value exceeded 1%, frequencies
at $q = q_m \pm \frac{1}{2}\Delta q$ were selected for the next level of computations. The circles
in Figure 2.2 show that all four intermediate values $q = -1.5, -0.5, 0.5, 1.5$
were included. We now determined initial values for the electric fields from
cubic interpolation of the solutions for the four frequencies nearest to the current
one. Next, the relative difference between interpolated and computed receiver
values was considered again for all available frequencies, and new neighboring
values for $q$ at a spacing of $\Delta q = 1/4$ were selected if the relative difference
exceeded 1%. Figure 2.2 shows that all new values between $-1$ and 2 were
selected. This procedure was repeated until all relative differences were less than
1%. At $\Delta q = 1/8$, only nine new frequencies were added and at $\Delta q = 1/16$ no
new ones were needed. Figure 2.2 shows the resulting values for the in-line electric
field component $E_1$ as circles, together with the curves obtained by interpolation
and the exact solution which can be found in, for instance, the chapter by Ward
and Hohmann (1987).

Table 2.1 lists iteration counts for the various frequencies. Note that the
iteration of BiCGStab2 can terminate half way through a full iteration, hence
the half counts. The parameter $\alpha$ measures the amount of grid stretching. The
maximum ratio between the widths of neighboring cells is $1 + \alpha$. If $\alpha$ exceeded
0.04, we switched to the more expensive multigrid preconditioner based on line
relaxation and semi-coarsening. For the latter, iterations counts and measured cpu
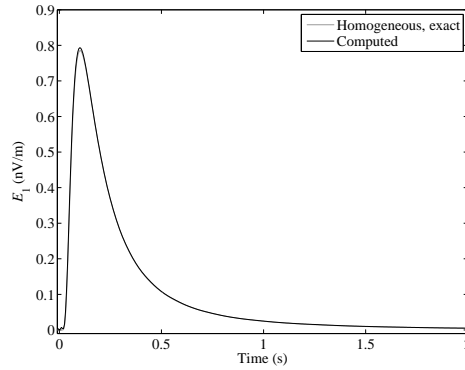
**Fig. 2.3**   Time-domain solution for the homogeneous problem. The black curve repre-
sents the numerical solution of the in-line component of the electric field, the
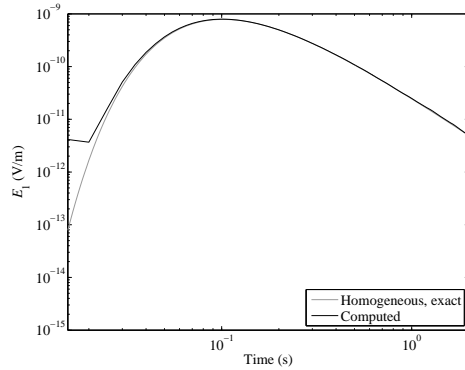gray one is the exact solution. The peak value has an error of about 1%.



**Fig. 2.4**   The same time-domain solution for the homogeneous problem as in the
previous figure, but now on a logarithmic scale.

times are marked by an asterisk. The results are listed in the order in which they
were computed. The effect of using interpolated values as initial guess instead of
zero values can be deduced from the iteration counts further down in the table.
The speed up is not dramatic, but it helps.

   The data points were interpolated by piecewise-cubic Hermite interpolation
(Fritsch and Carlson, 1980) to an equidistant grid of frequencies and transformed
to time by a fast Fourier transform. A comparison to the exact time-domain
solution, which can also be found in the chapter by Ward and Hohmann (1987),
is shown in Figures. 2.3 and 2.4. The error are largest at early and late times, due
to lack of the lowest and highest frequencies. Also, there is a difference between
the peak values of about 1% visible in Figure 2.3.

### 2.4.2   Scatterer in a homogeneous formation

The next example is a resistive scatterer in a homogeneous background with a conductivity of 1 S/m. A rectangular scatterer with $x$ between $-300$ and $300$ m, $y$ between $-200$ and $200$ m, and $z$ between $400$ and $600$ m has a conductivity of $0.1$ S/m. Figure 2.5 displays the layout. The source is the same as in the previous example. The grid, however, is different. It is equidistant inside the scatterer and hyperbolic cosine stretching (Mulder, 2006) is applied away from the object. In this case, we used a primary-secondary formulation in which the homogeneous

**Table 2.1**   Iteration counts at various frequencies.  The asterisk denotes counts obtained for the more expensive multigrid variant with line relaxation and semi-coarsening. The parameter $\alpha$ measures the amount of grid stretching. The required cpu time in seconds is included.

| $\Delta q$ | $q$ | $f$ (Hz) | $\alpha$ | iterations | cpu (s) |
|---|---|---|---|---|---|
| 1 | 2 | 100 | 0.032 | 3.5 | 292 |
| | 1 | 10 | 0.010 | 3.5 | 301 |
| | 0 | 1 | 0.022 | 3.5 | 303 |
| | $-1$ | 0.1 | 0.045 | 1.5* | 1393* |
| | $-2$ | 0.01 | 0.069 | 2.0* | 1879* |
| 0.5 | 1.5 | 31.6 | 0.020 | 4.0 | 344 |
| | 0.5 | 3.16 | 0.012 | 3.5 | 304 |
| | $-0.5$ | 0.316 | 0.034 | 7.0 | 599 |
| | $-1.5$ | 0.0316 | 0.057 | 1.5* | 1419* |
| 0.25 | 1.75 | 56.2 | 0.026 | 3.0 | 259 |
| | 1.25 | 17.8 | 0.015 | 3.5 | 304 |
| | 0.75 | 5.62 | 0.0076 | 3.0 | 260 |
| | 0.25 | 1.78 | 0.017 | 3.0 | 259 |
| | $-0.25$ | 0.562 | 0.028 | 5.0 | 429 |
| | $-0.75$ | 0.178 | 0.040 | 8.5 | 739 |
| | $-1.25$ | 0.0562 | 0.051 | 1.0* | 927* |
| | $-1.75$ | 0.0178 | 0.063 | 1.0* | 931* |
| 0.125 | 1.375 | 23.7 | 0.018 | 3.0 | 264 |
| | 1.125 | 13.3 | 0.0013 | 2.5 | 215 |
| | 0.875 | 7.50 | 0.0082 | 2.5 | 217 |
| | 0.625 | 4.22 | 0.0099 | 3.0 | 262 |
| | 0.375 | 2.37 | 0.015 | 2.0 | 174 |
| | 0.125 | 1.33 | 0.020 | 3.0 | 259 |
| | $-0.125$ | 0.750 | 0.025 | 3.5 | 307 |
| | $-0.375$ | 0.422 | 0.031 | 5.0 | 430 |
| | $-0.625$ | 0.237 | 0.037 | 6.5 | 562 |
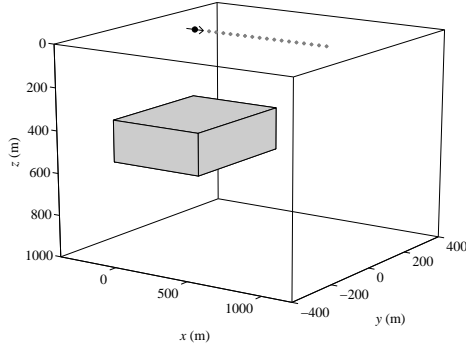
**Fig. 2.5**    Resistive scatterer in a homogeneous formation. The arrow and black dot mark
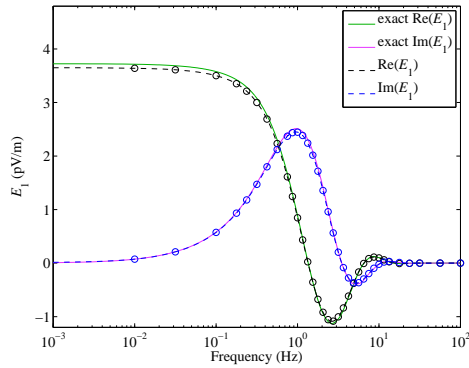the point-current source and the other dots indicate the receiver positions.



**Fig. 2.6**    The secondary solution in the frequency domain for the in-line electric field.

response is subtracted so that the source term and its singular response is replaced
by a source term that involves the exact solution.

Figure 2.6 displays the secondary frequency-domain solution for a source at the
origin and a receiver located at $(900,0,0)$ m and computed on a grid with $128^3$ cells.
For comparison, we computed the full electric field for the homogeneous medium
with the scatterer and subtracted the numerical solution for the homogeneous
medium without the scatterer. Figure 2.7 shows the difference. Since we have
subtracted the numerical primary field, its numerical errors in both computations
cancel, even when large. This explains the small differences between the figures.
Note that the adaptive procedure selected frequencies for the full field that are
different from those for the secondary field. The reason is that the primary
solution dominates the full field.

Figure 2.8 shows the time-domain response of the secondary, scattered field for
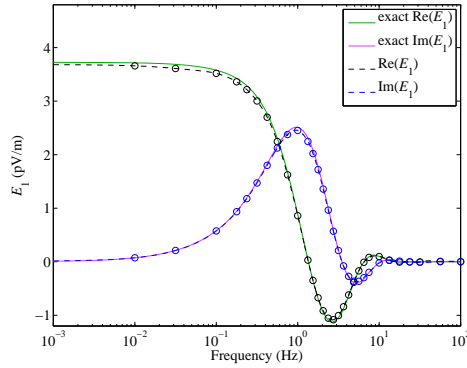
**Fig. 2.7**    Response for the in-line electric field, obtained by taking the difference between the full numerical solutions with and without scatterer.
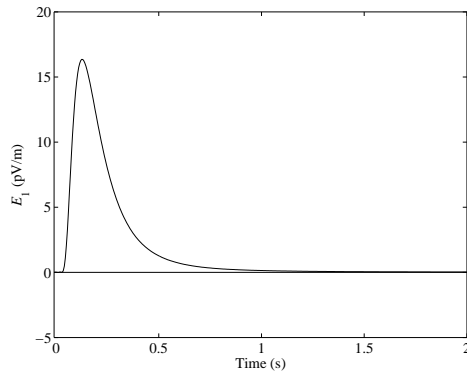


**Fig. 2.8**    The time-domain secondary solution for the scatterer computed with the primary-secondary formulation on a grid with $128^3$ cells.

the primary-secondary formulation.

### 2.4.3   Three layers

A slightly less trivial test problem consists of three layers: air, water, and sediments. These layers have a conductivity $\sigma$ of 0, 3, and 0.5 S/m, respectively, and a relative permittivity $\varepsilon_r$ of 1, 80, and 17. The water depth is 200 m. A dipole source in the $x$-direction at a depth of 175 m generates the in-line field shown in Figures. 2.9 and 2.10 for a frequency of 0.5 Hz. The figures demonstrate that the code provides reasonably accurate answers in this case.
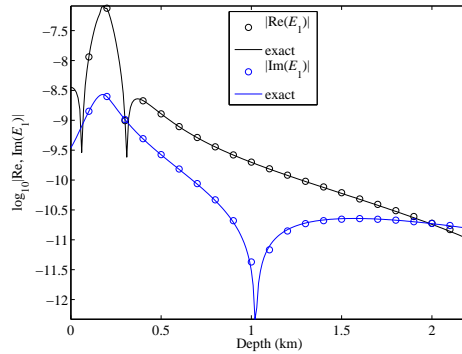
**Fig. 2.9**   In-line electric field at various depths at a horizontal in-line distance of 100 m from the source.



**Fig. 2.10**   The in-line electric field on the sea bottom.



**Fig. 2.11**   Logarithm of the resistivity ($\log_{10} \sigma^{-1}$, SI units) for a model with a salt body.

### 2.4.4   Shallow marine problem

The SEG/EAGE salt model (Aminzadeh *et al.*, 1997) served as a template for a realistic subsurface model. This model was designed for simulating seismic wave

**Fig. 2.12**    Frequency response for $E_1$, for a source at (6500,6500,50) m and a receiver
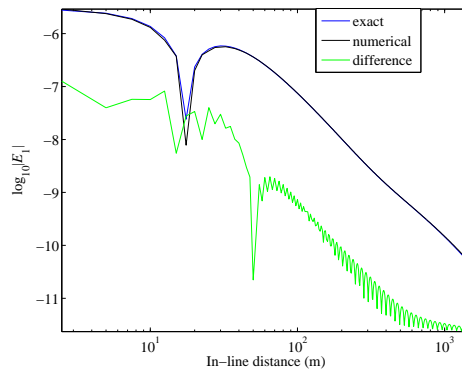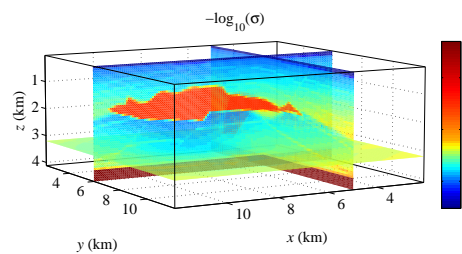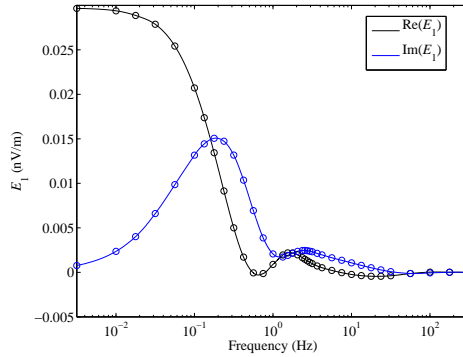at (9000,6500,100) m on the sea bottom.
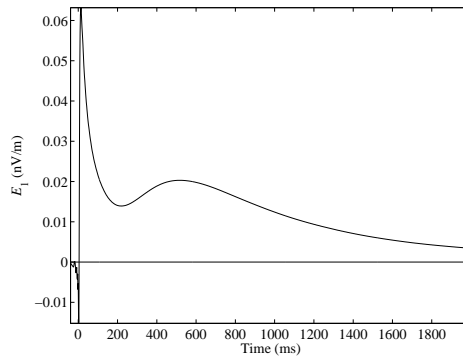


**Fig. 2.13**    Time response for the in-line field component $E_1$, for a 200-m finite-length
source centered at (6500,6500,50) m and a receiver at (9000,6500,90) m on
the sea bottom.

propagation and contains a complex salt body surrounded by sediments.  The
sea water has depths around 120 m.  Its dimensions are 13,500 by 13,480 by
4,680 m.  We replaced the seismic velocities of the model by resistivities ($\sigma^{-1}$).
For the water velocity of 1500 m/s, we chose a resistivity of 0.3 Ωm.  Velocities
above 4000 m/s, indicative of salt, were replaced by 30 Ωm.  Basement, beyond
3660 m depth, was set to 500 Ωm.  We determined the resistivity of the sediments
by $(v/1700)^{3.88}$ Ωm, with the velocity $v$ in m/s.  The paper of Meju *et al.* (2003)
motivated this choice.  For air, we used a resistivity of $10^8$ Ωm.  Figure 2.11 displays
the resistivity on a logarithmic scale.

We positioned a finite-length current source between (6400,6500,50) and
(6600,6500,50) m.  The receivers were placed on the sea bottom.  Initial solutions
were computed at frequencies $10^q$ Hz, with $q$ between $-2.5$ and 2.5 at a 0.5

increment. The adaptive scheme added more frequencies where needed. As before, cubic interpolation or extrapolation of solutions for other frequencies provided an initial guess for the iterative solution method. The spatial grid was again based on a balance between the skin depth at the given frequency and the details of the model. In the water layer, the grid was equidistant in the vertical direction and we used power-law stretching away from the surface and the maximum depth of the water layer. In the horizontal directions, we applied power-law stretching away from the center of the source.

Figure 2.12 shows one of the frequency-domain solutions and Figure 2.13 displays the time-domain response. The airwave shows up as an early peak. Of course, the air interface will also affect diffusion fronts that come in later. The anti-causal part must be caused by missing high frequencies and numerical errors in the higher frequencies.

## 2.5   CONCLUSIONS

Complexity analysis of time-domain methods for modeling electromagnetic diffusion shows that some popular methods have an $O(n^4)$ complexity, where $n$ is the number of points per spatial coordinate. Synthesizing time-domain solutions by using a frequency-domain method has a complexity of $O(n_f n^3)$, with $n_f$ the number of frequencies, if the solver convergences in a fixed number of iterations. We accomplished this on stretched grids with a multigrid variant based on line relaxation and semi-coarsening. On uniform or mildly stretched grids, we used a simpler multigrid scheme.

When the number of frequencies, $n_f$, is small relative to $n$, this frequency-domain method appears to be attractive. However, as our complexity analysis only provides estimates in terms of the number of unknowns and the actual required computer time will also depend on the constants in the estimates, a true comparison of methods should involve the operation count or the cpu time measured for an actual implementation. Also, $n_f$ might become as large as the number of time steps required for an implicit time-domain code for complex resistivity models. Furthermore, if early times are not recorded and the receivers are not too close to the source, the initial time-step size can be relatively large, leading to a smaller number of time steps (Haber *et al.*, 2002, 2004). Note that the time-domain computations do not require complex arithmetic. Therefore, an implicit method may compete or even be more efficient. In the frequency domain, however, it is easier to adapt the grid to the characteristic length scales of the solution.

We included examples to show how frequencies can be selected and how

time-domain solutions can be obtained by monotone piecewise-cubic Hermite interpolation and a fast Fourier transform.

## APPENDIX 2.1:
## TIME STEP INCREASING WITH THE SQUARE ROOT OF TIME

For accuracy reasons, we let the time step grow proportional to the square root of time. An explicit time-stepping scheme has $\Delta t_{\text{expl}} = C\mu\sigma h^2$ for the diffusive case, where the $O(1)$-constant $C$ depends on the number of spatial dimensions. Here $\mu$ is the magnetic permeability and $\sigma$ the conductivity. If the first-time step is chosen to be the same as for an explicit scheme, then we have $\Delta t = \sqrt{\Delta t_{\text{expl}} t}$. The time interval after $k$ steps is denoted by $t_k$. The above choices imply $t_0 = 0$, $t_1 = \Delta t_{\text{expl}}$, and $t_{k+1} = t_k + \sqrt{\Delta t_{\text{expl}} t_k}$ for $k \geq 1$. Let $t_k = \Delta t_{\text{expl}} u_k$. Then $u_1 = 1$ and $u_{k+1} = u_k + \sqrt{u_k}$, resulting in $u_2 = 2$, $u_3 = 2 + \sqrt{2}$, and so on. It can be seen from Figure 2.14 that $u_k \sim k^2/4$ for large $k$. A time span $T$ will require $n_t \simeq \sqrt{4T/\Delta t_{\text{expl}}}$ time steps. Using $h = O(1/n)$, we obtain $n_t \sim O(n)$ and an overall cost of $O(n^4)$ for 3D problems.
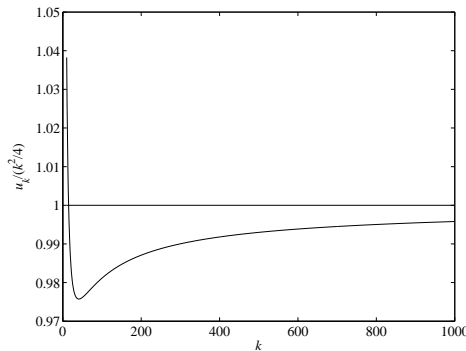


**Fig. 2.14**   The graph of $u_k/(k^2/4)$ as a function of $k$ shows that $u_k \sim k^2/4$ for large $k$.

# 3 Inversion of 3D TDEM data: The effect of time-weighting

**SUMMARY**

In order to mitigate the airwave problem, caused by the interaction between source-excited electromagnetic fields and the air, controlled-source electromagnetic surveys on land are almost exclusively implemented as a transient electromagnetics system (TEM), typically measuring step-off or step-on responses. In this way, the earth response can be well separated from the air response, as the latter primarily arrives at very early times and is then followed by the earth response. Because the air response carries no information about deeper targets, the early-time data are often considered useless and are removed in processing and inversion. In this chapter, we show that simply muting the early-time TEM data may lead to unsatisfactory inversion results. Without the early-time response, inversion cannot retrieve the resistivity of the near surface. Due to the diffusive nature of the electromagnetic fields, this also affects the reconstruction of the resistivity at larger depths. We illustrate this with a synthetic example.

## 3.1  INTRODUCTION

The controlled-source electromagnetics (CSEM) method is considered to be a useful geophysical tool for oil and gas exploration (Ellingsrud *et al.*, 2002). The reason is that CSEM data can provide resistivity maps of the subsurface, hence may allow us to estimate the prospect resistivity, thereby reducing the exploration risk in finding commercial hydrocarbon deposits. Nowadays, the CSEM method is widely used in: deep marine, shallow water, and land environments.

Acquisitions with the CSEM method can principally be subdivided into two: frequency-domain (FDEM) and time-domain (TEM) systems. In frequency-domain systems, we typically measure electromagnetic signals generated by a periodic, alternating source current that employs one or a few frequencies. In TEM systems, we measure electromagnetic signals induced by a certain combination of step-on or step-off source currents, repeated several times and stacked together to improve the signal-to-noise ratio. FDEM systems are preferably used in deep-marine environments where the thick layer of sea water effectively shields the measurements from EM noise present at the surface, whereas TEM systems are more appropriate in shallow water and on land because of the much stronger EM noise.

The interaction between the source-excited EM fields and the air creates a source-induced airwave component. This airwave may dominate the EM field measurements at any frequency, making the signal from the subsurface hard to distinguish in a frequency-domain approach. The airwave propagates in the air with the speed of light, whereas the electromagnetic fields diffuse into the earth. The part that propagates along the surface is called a lateral wave. It sends an electromagnetic field into the ground with an almost vertical diffusion direction (Baños, 1966; King *et al.*, 1992). A similar effect can be observed for a source at the interface between two conducting layers, where the fast diffusive medium (low conductivity) generates a field in the slow diffusive medium (high conductivity) that diffuses in the direction of the normal to the interface. With step-off or step-on sources in a TEM system, the earth response can generally be well separated from the air response in the time domain, since the latter, propagating with the speed of light, primarily arrives at a very early time and is then followed by the earth response. Hence, in the processing we could boost the late-time data to extract the information of the deeper targets.

The TEM signal that carries deep-target information is often weaker than the EM noise. Measurements need to be repeated and stacked together to obtain TEM data with a good enough signal-to-noise ratio. After this acquisition procedure, the earth response can generally be well separated from the air response. This time

separation requires a large enough frequency band, otherwise the signal is not sufficiently localized in time. This means that measuring the data misfit between modeled and observed data in the frequency domain is not well suited for inversion. A time-domain formulation is preferred. However, the interpretation of measured TEM data can still be difficult. As the early-time data carry no information about deeper targets, they are often considered useless and removed in processing and inversion. However, this may harm the resistivity estimate. Muting the early-time responses may remove information about the shallow resistivity variations. In the later time responses, shallow and deep resistivity variations are mixed because of the strongly diffusive nature of electromagnetic signals in the earth.

In this chapter, we study the early-time muting of TEM data in a time-domain inversion scheme. We investigate some time weighting approaches and their effect on the final resistivity images. We first explain the implementation of the time-domain inversion. For efficiency, the time-domain responses are obtained by Fourier transforms of a limited number of frequency-domain responses, using a logarithmic fast-Fourier transform. Then, we present an example showing that simply muting the early times of TEM data can lead to unsatisfactory results.

## 3.2   METHOD

We formulate the resistivity imaging of TEM data as an inverse problem. With the observed electric and magnetic time series, $e_{s,r}^{\mathrm{obs}}(t)$ and $h_{s,r}^{\mathrm{obs}}(t)$, generated at the source positions $\mathbf{x}_s$ and observed at the receiver positions $\mathbf{x}_r$, the inverse problem consists of finding a resistivity $\rho$ that minimizes the weighted least-squares functional

$$J(\rho) = \frac{1}{2} \sum_{s,r} \int_0^T \left\{ \|w_{s,r}^e(t)\Delta e_{s,r}(t;\rho)\|^2 + \|w_{s,r}^h(t)\Delta h_{s,r}(t;\rho)\|^2 \right\} \, dt \quad (3.1)$$

where

$$\Delta e_{s,r}(t;\rho) = e_{s,r}(t;\rho) - e_{s,r}^{\mathrm{obs}}(t), \quad \text{and}$$
$$\Delta h_{s,r}(t;\rho) = h_{s,r}(t;\rho) - h_{s,r}^{\mathrm{obs}}(t).$$

Here, $T$ is the maximum recording time, $e_{s,r}$ and $h_{s,r}$ represent the computed electric and magnetic responses, and $w_{s,r}^e$ and $w_{s,r}^h$ are data weights depending on source and receiver locations and time.

Following closely the approach of Plessix and Mulder (2008), we minimize $J$ in Equation 3.1 with a quasi-Newton optimization, a limited-memory version

of the Broyden-Fletcher-Goldfarb-Shanno (BFGS) method (Byrd *et al.*, 1995). We follow the classic inverse problem formulation where the gradient of the least squares functional is computed with the adjoint method. We apply a regularization term in order to stabilize the optimization process. As with each gradient-based optimization, our approach requires an efficient 3D numerical solver.  In the following paragraph, we describe how we tackle this issue.

For time-domain EM modeling, there are a number of options.  The most prominent methods are explicit Du Fort-Frankel time-stepping schemes, implicit schemes, Lanczos-based reduction and matrix exponential schemes, and Fourier-transform-based methods. However, by comparing the computational complexity of these methods, the previous chapter shows that frequency-domain modeling followed by a Fourier transformation is an attractive choice. The computational cost of a time-domain solution with this approach is determined mostly by the number of frequencies. With parallel computers, this leads to an efficient solver for time-domain EM modeling since different frequencies can be treated simultaneously.  Here, we adopt this approach.  The frequency responses are computed with an efficient iterative method preconditioned by one cycle of a multigrid solver (Mulder, 2006).

The choice of the frequency discretization remains to be decided. Because of the diffusive nature, it is generally recognized that a time-domain EM response is well represented by a set of frequencies on a regularly spaced logarithmic frequency axis.  Since we need to compute the responses over a large frequency band, say between 0.01 and 100 Hz, a logarithmic scale saves a considerable amount of computations compared to a linear scale. Mulder *et al.* (2008), for instance, used an approach that consists of computing the responses on a set of frequencies regularly spaced on a logarithmic axis, then interpolating the responses with cubic Hermite interpolation to a set of frequencies regularly spaced on a linear axis, and finally computing the time-domain response with a standard Fast Fourier Transformation (FFT). This approach is simple and straightforward. However, the use of the standard FFT for time-domain EM modeling is rather costly. FFT requires a dense sampling in order to capture the early-time data, (namely the high frequencies), which increases the number of points and makes the standard FFT expensive. The use of a Fourier transform on a logarithmic axis is therefore an attractive choice, which we adopt here (Talman, 1978; Haines and Jones, 1988). Our implementation is as follows. First, we compute the frequency responses on a regularly spaced logarithmic frequency axis, then we determine the time responses with a logarithmic Fourier transform. The resulting time responses are discretized on a regularly spaced logarithmic time axis. Finally, we interpolate the time responses on a regularly spaced linear time axis with cubic interpolation.
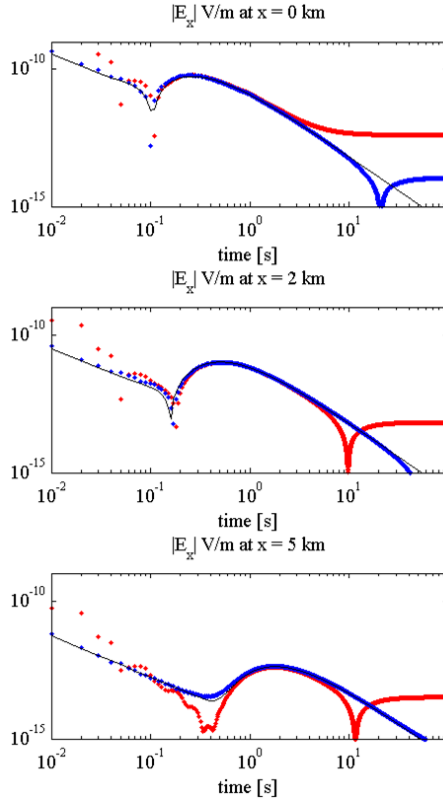
**Fig. 3.1**  Time response of $E_x$, generated by an $x$-directed point source located at the origin of the model on the surface. The three receivers are also located on the surface with the following lateral coordinates $(x, y) = (0,2)$ km (top), (2,2) km (middle), and (5,2) km (bottom). The red dots corresponds to the estimated solution with the standard FFT, the blue dots to the solution when with the logarithmic Fourier transformation, and the black line to the exact analytical solution.

## 3.3  RESULTS

### 3.3.1  Modeling test

We start by showing the relevance of our modeling approach by comparing our estimated time response with the exact analytical solution. We consider a homogeneous half-space model with a resistivity of $0.5\,\Omega$m. The source is an in-line electrical point dipole source placed on the surface. Three receivers are placed on the surface at $(x, y) = (0,2)$ km, (2,2) km, and (5,2) km, respectively, measuring the in-line electric field. The time-domain solution is sampled at a rate
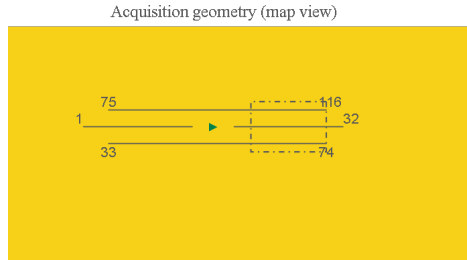
Acquisition geometry (map view)

**Fig. 3.2**    The dash line indicates the lateral position of hydrocarbon target. The green triangle indicates the lateral position of a source. Solid lines show the receiver configuration, consisting of 32 receivers per line. Numbers indicates receiver indexes. Receivers 1–32 are placed in an in-line configuration, while 33–74 and 75–116 have a broad-side configuration.

of 0.01 s within the range [0,100] s.

The results are displayed in Figure 3.1. The red dots represent the solutions computed with the standard FFT. In this approach, the interpolation to a regular linear sampling is done in the frequency domain. The blue dots represent the solutions with the logarithmic FFT. Now, the interpolation to a regular linear sampling is done in the time domain. For comparison, we have plotted the exact analytical solution with black lines. Although some inaccuracies are visible at very late times, the use of the logarithmic Fourier transformation clearly provides more accurate solutions at the early and late times compared to the ones obtained by standard FFT. In this test, we have used the same number of frequency-domain responses in both approaches. To obtain a better results with the standard FFT approach, a much larger numbers of frequency-domain responses would need to be evaluated. This would considerably increase the computational time.

### 3.3.2    Inversion problem

We carried out a small synthetic time-domain inversion. The time-domain responses were computed with the multigrid-based frequency-domain solver and the logarithmic FFT as explained in the previous section. The "true" model consists of a $0.5\,\Omega$m half-space background resistivity and a $100\,\Omega$m resistor located at 1 km depth below the surface. The dimension of the resistor is 2 km by 2 km by 100 m. The top panel of Figure 3.3 shows a vertical cross section of the resistivity model. The acquisition geometry is displayed in Figure 3.2. We consider three receiver lines with a 1 km spacing between the lines. Each line contains 32 receivers spaced at 200 m. Only the in-line electric components are recorded. We considered two source positions with a spacing of 4 km. Each source
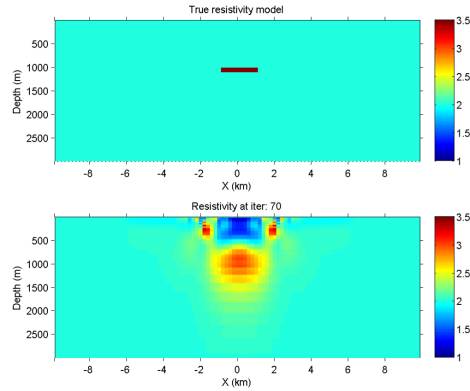
**Fig. 3.3**  The bottom panel shows the optimal resistivity model after 70 iterations, while the top panel shows the true model used to generate data. The resistivity values are clipped at 3.5 Ωm
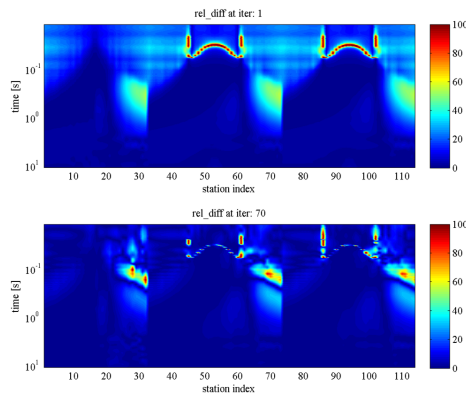


**Fig. 3.4**  The normalized misfit between the data and the computed responses. The scale is in percent. Top and bottom panels are misfit at iteration 1 and 70, respectively.

is laterally located at 1 km from the edge of hydrocarbon target. The maximum recording time is 10 s and the sampling rate 0.01 s.

For the first inversion example, we take the full time responses into account, including early and late times. The initial model is a 0.5 Ωm homogeneous half-space resistivity model. We did not apply any data weights or depth weighting. The top panel of Figure 3.4 shows the normalized difference between the data and the computed responses with the initial resistivity model. A large anomaly can be observed between 0.1 s and 2 s for the receivers located above the target.

The final resistivity model, plotted in the bottom panel of Figure 3.3, was

**Fig. 3.5**   The bottom panel shows the resistivity model after 20 iterations, while the top panel shows the true model used to generate data. The resistivity values are clipped at 3.5 Ωm

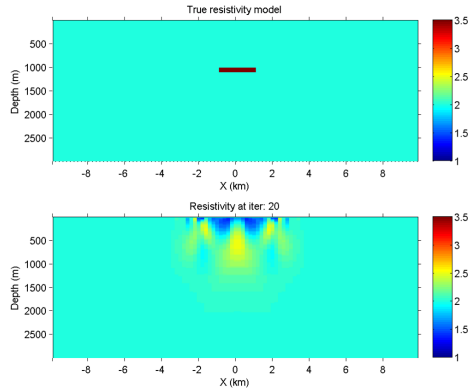obtained after 70 iterations. The deep resistive zone is well retrieved. Due to the diffusive nature of the EM inversion, the resolution is poor, as expected. The final normalized data misfit is shown in the bottom panel of Figure 3.4. The misfit is significantly reduced, indicating that the final model correctly interprets the data. Some overshoots in the final normalized differences are due to division by small numbers. A single inversion iteration took a bit more than 30 minutes, computing 40 frequencies in parallel on 40 cores, and required 80 forward and 40 backward modeling steps. We needed twice the number of forward computations, because we did not store the forward fields for the gradient. Instead, after having computed the data residual, we recomputed the forward fields for the correlation with the backward fields. The convergence rate of the inversion may be sped up by applying suitable depth and data weighting, but we did not consider that here.

### 3.3.3   The effect of time weighting

The previous result shows that the resistivity model can be well retrieved with a time-domain EM inversion and the full time series. In real cases, using the early times may not be possible. The airwave may not be correctly sampled or its amplitude may be clipped. In a second inversion, we investigate the effect of removing/blanking the early times. We use the same dataset as in the previous example. Because the large anomaly coming from the deep resistor was observed after 0.1 s, we decided to mute the data from 0 to 0.1 s, as shown in Figure 3.6 by a yellow box. Then, we ran the inversion with the same parameters as the previous example. The data misfit decreased very slowly. We stopped the inversion

after 20 iterations. The bottom panel of Figure 3.5 shows the resistivity model and the bottom panel of Figure 3.6 shows the normalized data misfit. We notice that the inversion starts to explain the data for late times. However, significant shallow artifacts appear in the resistivity map. Removing the early-time data makes the non-uniqueness of the inversion worse. It apparently enlarges the null space of the misfit function. In the previous inversion, the early times helped to constrain the shallow part of the resistivity. Because of the diffusive nature of the electromagnetic fields, there is a trade-off between the shallow and deep part of the model. When the shallow part cannot be correctly constrained or estimated, the deep part is not retrieved satisfactory. This behaviour is somewhat similar to the static shift phenomena common to EM measurements. A local high-resistivity contrast in the near surface biases the interpretation of the resistivity in the deeper part of the earth.
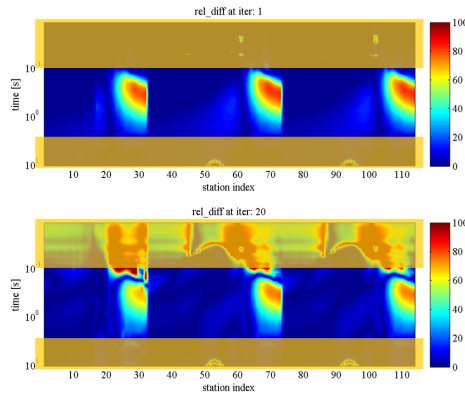


**Fig. 3.6**    The normalized data misfit. The yellow box indicates data clipping. The scale is in percent.

## 3.4    CONCLUSION AND FUTURE OUTLOOK

We have studied some effects of time weighting on time-domain EM inversion. The results show that simply muting the early-time TEM data may lead to unsatisfactory results because it makes the non-uniqueness worse. Inversion cannot retrieve the resistivity of the near surface, which makes the interpretation of the resistivity map at depth difficult, if not impossible. The use of offset and depth weighting may mitigate this problem. However, not constraining or estimating the shallow part of the resistivity model may bias the results.

# 4 Applying ENO interpolation to CSEM modelling

**SUMMARY**

Modelling and inversion of controlled-source electromagnetic fields requires accurate interpolation of modelled results near strong resistivity contrasts. There, simple linear interpolation may produce large errors, whereas higher-order interpolation may lead to oscillatory behaviour in the interpolated result. We propose to use the essentially non-oscillatory (ENO), piecewise polynomial interpolation scheme designed for piecewise smooth functions that contain discontinuities in the function itself or in its first or higher derivatives. The scheme uses a non-linear adaptive algorithm to select a set of interpolation points that represents the smoothest part of the function among the sets of neighbouring points.

We present numerical examples to demonstrate the usefulness of the scheme. The first example shows that the ENO interpolation scheme better captures an isolated discontinuity. In the second example, we consider the case of sampling the electric field computed by a finite-volume CSEM code at a receiver location. In this example, the ENO interpolation performs quite well. However, the overall error is dominated by the discretisation error. The other examples consider the comparison between sampling with ENO interpolation and existing interpolation schemes. In these examples, ENO interpolation provides more accurate results than standard interpolation, especially near discontinuities.

## 4.1   INTRODUCTION

The marine controlled-source electromagnetic (CSEM) method was introduced in the late 1970s to study the resistivity of the oceanic lithosphere (Cox, 1981; Constable and Srnka, 2007). The method was originally intended as a complement to magnetotelluric (MT) measurements to obtain data at relatively higher frequencies than present in the MT signal after travelling through the sea water. As EM measurements enable a distinction between highly resistive bodies and their surrounding structures, the method attracted the attention of the oil industry because hydrocarbon reservoirs are far more resistive than brine-filled formations. As reported by many authors, controlled-source electromagnetic (CSEM) measurements may indicate the presence of hydrocarbons (Eidesmo *et al.*, 2002; Ellingsrud *et al.*, 2002; Amundsen *et al.*, 2004; Carazzone *et al.*, 2005; Srnka *et al.*, 2006; Choo *et al.*, 2006; Darnet *et al.*, 2007; MacGregor *et al.*, 2007). Moreover, CSEM data and inversion results have nowadays found their use for derisking potential prospects, complementary to seismics. Comprehensive overviews can be found in, for instance, the October 2000 issue of Inverse Problems, the March–April 2007 issue of Geophysics, and the March 2007 issue of The Leading Edge.

Marine CSEM surveys typically employ a high-powered electric source close to the seafloor to induce low-frequency EM signals that penetrate into the subsurface. An array of EM receivers placed on the seafloor records the horizontal electric and magnetic field components. In many cases, the presence of hydrocarbons may be inferred by comparing the EM response to a reference data-set corresponding to a background resistivity model without hydrocarbon reservoirs. However, other types of resistive structures, such as gas hydrates or anhydrite layers, may lead to false positives. In this case, full-scale inversion of the EM data for the subsurface resistivity is preferred (Plessix and Mulder, 2008). This requires an accurate numerical scheme.

Various approaches for accurately solving Maxwell's equations exist. They employ a finite-difference, finite-volume, finite-element, or an integral-equation method. Each approach has his advantages and disadvantages. Finite-difference and the closely related finite-volume methods are the easiest to grasp and relatively straightforward to implement, but numerical accuracy requires dense grids, affecting the memory requirements and computation time. Finite-element methods on unstructured grids allow for better gridding near sharp contrast, but have a larger overhead and may result in a large sparse linear system that is more difficult to solve. For an overview of developments in numerical EM modelling, we refer to Avdeev (2005), Börner (2010), and the references listed therein.

Each method will have various sources of numerical errors that may or may

not be easy to control. The numerical solution of the Maxwell equations for a general subsurface resistivity model with a finite-difference, finite-element, or finite-volume method generally involves three steps: discretisation of the equations on a grid, their numerical solution, and interpolation of solution from grid points to receiver positions. Because of limitations in computational resources, each step will contribute to the numerical error in the final result. The discretisation error tends to decrease with some power of the grid spacing, often with the power two for common choices that are therefore called second-order schemes. The numerical solution of the discrete equations for large-scale 3D problems is usually obtained with an iterative method as direct methods tend to be too costly. The iterative method will terminate with a residual error, but with a proper algorithm, the effect on the solution will be small compared to the discretisation error. Finally, the sampling of the resulting gridded solution on receiver locations will introduce an interpolation error. The subject of this chapter is the accurate interpolation of the electric field components that may be discontinuous across resistivity contrasts.

We employed a finite-volume discretisation of the Maxwell equations (Weiland, 1977) that represents the electric field components as edge averages on the edges of regular Cartesian, possibly stretched, grid of rectangular cells. The direction of each electric field component agrees with that of the edge it is assigned to. The discretisation provides second-order accuracy for the solution if the material properties are constant (Monk and Süli, 1994). When the material properties vary across the domain, the discretisation, in general, leads to a first-order error in the solution (van Rienen, 2001). We solved the discrete equations with BiCGStab2 (van der Vorst, 1992; Gutknecht, 1993), preconditioned by a multigrid solver (Mulder, 2006). We will assume that the contribution to the numerical error of the solution method is negligible. What remains is the interpolation error that occurs when the edge averages of the electric field components are interpolated to the receiver positions. Tri-linear interpolation is the simplest approach on the grids we use. When the solution is smooth, it adds a second-order contribution to the discretisation error, caused by the linear interpolation as well as the second-order difference between edge-averages and point values. Near sharp resistivity contrasts, the field component perpendicular to the interface that separates the two resistivities is discontinuous and the linear interpolation scheme may lead to large errors in that case. Since the computational cost of interpolation is much smaller than that of the solver, the use of a more accurate interpolation scheme appears to be worthwhile.

We want to have an interpolation scheme that can deal with edge averages as well as point values and that can handle discontinuities in the field components or their spatial derivatives. A scheme with these properties was already devised

by Harten *et al.* (1997) and named essentially non-oscillatory (ENO) interpolation. The method was originally designed to improve the numerical accuracy of Godunov's scheme (Godunov, 1959) for compressible flow computations with shock waves and contact discontinuities. The original Godunov scheme is a finite-volume method that represents the solution by piecewise constant values per grid cell. Time-stepping requires fluxes at the boundaries between neighbouring cells. These are determined from the exact solution of the so-called Riemann problem. Although the scheme avoids the numerical oscillations that plague central difference schemes, it is only first-order accurate. The numerical error can be interpreted as artificial diffusion, causing discontinuities to be smeared out. Van Leer (1979) proposed a higher-order extension of the method that constructs piecewise polynomials per cell from the given cell averages in such a way that over- and undershoots during time stepping are avoided. A piecewise linear scheme, for instance, may lead to numerical oscillations if the slope inside a cell is too steep. By reducing its size, the oscillation can be avoided. The ENO scheme is a further generalisation that allows for numerical oscillations but requires them to be of the same size as the numerical discretisation error. Shu (1998) lists applications in many different fields, as part of the discretisation of the governing equations as well as a post-processing tool for interpolating solutions to a given set of points. The last option will be considered here. In this chapter, we consider the application of ENO interpolation to determine the electric field components at arbitrary receiver locations in the computational domain from their computed edge averages. We investigate the accuracy of this interpolation scheme in relation to the overall error of the CSEM modelling. The outline of the chapter is as follows. We first list Maxwell's equations for a conducting medium and give the main steps in the numerical solution procedure, the details of which can be found elsewhere (Mulder, 2006). The ENO interpolation scheme is reviewed in Appendix 4.1. We present a number of examples to illustrate its performance in CSEM applications. Finally, we summarize our conclusions.

## 4.2   THE METHOD

We briefly review Maxwell's equations for a conducting medium, which are assumed to be isotropic, time-invariant, and arbitrarily inhomogeneous.

Let $\mathbf{x} = (x_1, x_2, x_3)$ denote the Cartesian coordinate vector and let $t$ denote time. As usual, the $x_3$-axis is pointing downward. Maxwell's equations for conducting media in the presence of an electric current source $\mathbf{J}_s$ can be written

as (Ward and Hohmann, 1987; Jackson, 1999; Griffiths, 1999)

$$\partial_t \mathbf{B}(\mathbf{x}, t) + \nabla \times \mathbf{E}(\mathbf{x}, t) = 0, \tag{4.1}$$

$$\nabla \times \mathbf{H}(\mathbf{x}, t) - \partial_t \mathbf{D}(\mathbf{x}, t) = \mathbf{J}_c(\mathbf{x}, t) + \mathbf{J}_s(\mathbf{x}, t), \tag{4.2}$$

where the conduction current, $\mathbf{J}_c$, obeys Ohm's law,

$$\mathbf{J}_c(\mathbf{x}, t) = \sigma(\mathbf{x})\mathbf{E}(\mathbf{x}, t).$$

Here, $\sigma(\mathbf{x})$ is the conductivity, $\mathbf{E}(\mathbf{x}, t)$ is the electric field and $\mathbf{H}(\mathbf{x}, t)$ is the magnetic field. The electric displacement $\mathbf{D}(\mathbf{x}, t) = \varepsilon(\mathbf{x})\mathbf{E}(\mathbf{x}, t)$ and the magnetic induction $\mathbf{B}(\mathbf{x}, t) = \mu(\mathbf{x})\mathbf{H}(\mathbf{x}, t)$. Parameters $\varepsilon$ and $\mu$ are respectively the permittivity and the magnetic permeability. Both parameters are usually expressed as $\varepsilon = \varepsilon_r \varepsilon_0$ and $\mu = \mu_r \mu_0$, where $\varepsilon_r$ and $\mu_r$ are their relative values, and $\varepsilon_0$ and $\mu_0$ their absolute values in vacuum. Non-conductive media have extremely small value of $\sigma$, which are idealized as $\sigma = 0$.

Using Equation 4.1, we can eliminate the magnetic field from Equation 4.2, yielding the second-order parabolic system of equations,

$$\mu_0 \varepsilon \partial_t \partial_t \mathbf{E} + \mu_0 \sigma \partial_t \mathbf{E} + \nabla \times \mu_r^{-1} \nabla \times \mathbf{E} = -\mu_0 \partial_t \mathbf{J}_s.$$

To transform from the time domain to the frequency domain, we define the temporal Fourier transform of a space- and time-dependent vector field $\mathbf{E}(\mathbf{x}, t)$ as

$$\hat{\mathbf{E}}(\mathbf{x}, \omega) = \int_{-\infty}^{\infty} \mathbf{E}(\mathbf{x}, t)e^{\imath \omega t}\, dt,$$

where $\imath$ is the imaginary unit and $\omega$ the angular frequency. The resulting system of equations is

$$\imath \omega \mu_0 \tilde{\sigma} \hat{\mathbf{E}} - \nabla \times \mu_r^{-1} \nabla \times \hat{\mathbf{E}} = -\imath \omega \mu_0 \hat{\mathbf{J}}_s, \tag{4.3}$$

where $\tilde{\sigma} = \sigma - \imath \omega \varepsilon$.

To compute a numerical solution of Equation 4.3 for a given conductivity and source term, we discretised the equations on a stretched grid with the Finite Integration Technique (Weiland, 1977) and solved the resulting system of equations with an iterative method using a multigrid solver as preconditioner (Mulder, 2006). For an assessment of the method's performance, we refer to earlier papers (Mulder, 2006, 2008; Mulder *et al.*, 2008). The method is matrix-free: we never explicitly form the large sparse linear matrix that describes the discretised problem, but only evaluate its action on the latest estimate of the solution, thereby reducing storage requirements.

The discretisation starts with a grid of block-shaped cells. The three electromagnetic field components are represented as average values on edges, the $x$-components on edges parallel to the $x$-direction and the $y$- and $z$-components parallel to their corresponding directions. This approach can be interpreted as a finite-volume generalisation of the scheme by Yee (1966). Perfectly electric conducting (PEC) boundary conditions are used where the model is truncated. To reduce the influence of these unrealistic boundary conditions on the resulting solution, we applied grid stretching to move them sufficiently far away from the region of interest.

The discretisation with the Finite Integration Technique provides a representation of the electric field components as edge averages. Since the receivers can be located at arbitrary positions relative to the computational grid, interpolation is required. Here, we propose to use the ENO interpolation scheme. Like standard Newton interpolation, ENO interpolation starts with calculating a table of divided differences. Instead of selecting points symmetrically around the point where the interpolated value is needed, ENO interpolation applies an adaptive algorithm, choosing a stencil – a set of subsequent points – in such a way that the resulting interpolating polynomial does not have large oscillations. If, for instance, we want to perform quadratic interpolation to a given point, we can select the nearest grid point and its left and right neighbours. ENO considers the two grid points on both sides of the given point and chooses the third grid point either to the left or to the right of the other two, preferring the choice with the smallest values of the divided differences. We refer to Appendix 4.1 for details.

## 4.3   EXAMPLES

We present a number of examples that highlight the difficulties related to interpolating averaged field values on a non-uniformly sampled grid for piecewise continuous fields. We first illustrate the performance of ENO interpolation when reconstructing a simple function with an isolated discontinuity. We then consider the accuracy improvement provided by ENO interpolation when applied to a simple electromagnetic test problem. Finally, we investigate the performance of ENO interpolation in CSEM modelling of a marine configuration with a lateral discontinuity in the sea bed.

The values of all quantities are given in SI units, except for the first test where dimensionless values are used.
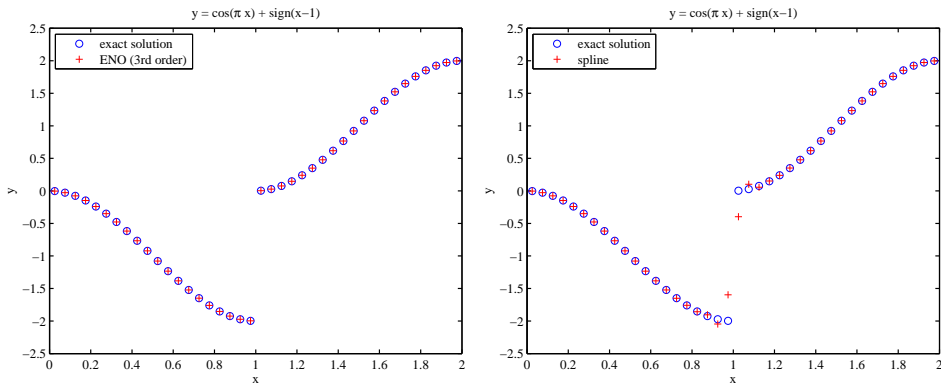
**Fig. 4.1** Result for the cubic ENO interpolation scheme (left) and for standard cubic-spline interpolation (right) of a function with an isolated discontinuity.

## Simple test problem

To illustrate the performance of ENO interpolation, we first consider the reconstruction of the function $y(x) = \cos(\pi x) + \text{sign}(x - 1)$, $0 \le x \le 2$. We divide the interval $[0, 2]$ into $N$ equidistant cells and define the grid points,

$$x_i = i \cdot \frac{2}{N}, \quad i = 0, 1, \ldots, N.$$

We compute cell averages and interpolate to point values at cell centres. Table 4.1 lists the number of cells and errors.

The error is calculated in the 2-norm and maximum norm. If the grid has $N$

**Table 4.1** Solution error for a function reconstruction test problem with an increasing numbers of cells, $N$. The relative errors $\varepsilon_{r;2}$ and $\varepsilon_{r;\infty}$ were obtained with cubic ENO interpolation (ENO$_3$) or with standard cubic-spline interpolation.

| | $\varepsilon_{r;2}$ - ERROR | | $\varepsilon_{r;\infty}$ - ERROR | |
| --- | --- | --- | --- | --- |
| $N$ | ENO$_3$ | Spline | ENO$_3$ | Spline |
| 20 | $0.115 \times 10^{-5}$ | 0.105 | $0.156 \times 10^{-5}$ | 0.201 |
| 40 | $0.579 \times 10^{-7}$ | 0.074 | $0.109 \times 10^{-6}$ | 0.200 |
| 80 | $0.273 \times 10^{-8}$ | 0.053 | $0.697 \times 10^{-8}$ | 0.200 |
| 160 | $0.129 \times 10^{-9}$ | 0.037 | $0.439 \times 10^{-9}$ | 0.200 |

number of cells, the error in the 2-norm is defined as

$$\varepsilon_2 = \left[ \sum_{i=1}^{N} (\tilde{y}_i - y_i)^2 \right]^{1/2},$$

and the relative error as

$$\varepsilon_{r;2} = \varepsilon_2 \left[ \sum_{i=1}^{N} y_i^2 \right]^{-1/2},$$

where $\tilde{y}_i \equiv \tilde{y}(x_{c;i})$ denotes the numerical solution and $y_i \equiv y(x_{c;i})$ the function values, calculated at cell centres $x_{c;i} = (x_i + x_{i-1})/2$. For the maximum norm, we have

$$\varepsilon_\infty = \max_{i=1,\dots,N} |\tilde{y}_i - y_i|,$$

and the relative error is

$$\varepsilon_{r;\infty} = \varepsilon_\infty \left[ \max_{i=1,\dots,N} |y_i| \right]^{-1}.$$

Table 4.1 lists the relative errors for various numbers of cells, given by $N$. Figure 4.1 shows the result of cubic ENO interpolation when $N$ is set to 40. When compared to standard cubic-spline interpolation, we clearly see that the ENO scheme better captures the discontinuity.

**Artificial test problem**

The finite-volume multigrid solver provides the solution of the EM problem as edge-averaged components of the electric field, where the coordinate direction of the component agrees with the direction of the edge. We can apply ENO interpolation to map the edge averages to point values. Here, we investigate the accuracy of the interpolation scheme.

We repeated the artificial test problem of Mulder (2008). It is based on eigenfunctions that obey the PEC boundary conditions. We consider a domain $\Omega = [0, 2\pi]^3 \text{ m}^3$ and split it into two parts, $\Omega_1$ with $z < \pi$ and $\Omega_2$ for $z > \pi$. The conductivity $\sigma = 10 + (x + 1)(y + 2)(z - \pi)^2$ S/m in $\Omega_1$ and $\sigma = 10$ S/m in $\Omega_2$. We set $\varepsilon_r = 0$, which is unphysical, $\mu_r = 1$, and $\omega = 10^6$ rad/s. We define the exact solution as

$$E_1 = -2\partial_x \psi, \quad E_2 = -2\partial_y \psi, \quad E_3 = \partial_z \psi,$$

where $\psi = \sin x \cdot \sin y \cdot \sin z$. We computed edge averages of the current source, $\mathbf{J}_s = -\tilde{\sigma}\mathbf{E} + \nabla \times (\imath\omega\mu)^{-1}\nabla \times \mathbf{E}$, by integrating the substituted exact solution.

Table 4.2 lists the errors in the numerical solution after interpolation of the edge averages of the three electric field components to point values at the midpoints of the edges where the components are assumed to live. The first component, $E_1$, is represented on edges parallel to the $x$-direction, $E_2$ lives on midpoints of edges parallel to the $y$-direction, and $E_3$ on edges parallel to $z$. The errors were measured by the 2-norm and the maximum norm, using the same definitions as Mulder (2008). The norms are measuring the difference between the numerical value and the exact value at the grid points. Since the numerical values are obtained as edge averages, we used the ENO interpolation to map it to the point values at the same grid points. The number of cells in each coordinate direction is given by $N_x = N_y = N_z = N$. We compared the error in the numerical solution with cubic spline (superscript $n$) interpolation and with ENO (superscript $ne$) interpolation. To distinguish between the contribution of the discretisation error and the interpolation error, we also applied ENO interpolation to the exact solution, represented in the form of edge averages. The results in Table 4.2 are marked by the superscript $ee$.

The discretisation scheme in our modelling code leads to a solution with

**Table 4.2**  Solution errors for the artificial test problem with an increasing number, $N \times N \times N$, of cells. The relative errors $\varepsilon_{r;2}$ and $\varepsilon_{r;\infty}$ were obtained with standard cubic-spline interpolation applied to the numerical solution (superscript $n$), with cubic ENO interpolation (ENO$_3$) applied to the numerical solution (superscript $ne$) or the exact solution (superscript $ee$).

| | | L$_2$ - ERROR | | |
|---|---|---|---|---|
| $N$ | $h_{\max}$ | $\varepsilon^n_{r;2}/h^2_{\max}$ | $\varepsilon^{ne}_{r;2}/h^2_{\max}$ | $\varepsilon^{ee}_{r;2}/h^4_{\max}$ |
| 16 | 0.39 | $8.6 \times 10^{-2}$ | $7.5 \times 10^{-2}$ | $1.5 \times 10^{-2}$ |
| 32 | 0.20 | $8.8 \times 10^{-2}$ | $7.7 \times 10^{-2}$ | $1.3 \times 10^{-2}$ |
| 64 | 0.098 | $8.9 \times 10^{-2}$ | $7.8 \times 10^{-2}$ | $1.0 \times 10^{-2}$ |
| 128 | 0.049 | $8.9 \times 10^{-2}$ | $7.8 \times 10^{-2}$ | $0.8 \times 10^{-2}$ |

| | | L$_\infty$ - ERROR | | |
|---|---|---|---|---|
| $N$ | $h_{\max}$ | $\varepsilon^n_{r;\infty}/h^2_{\max}$ | $\varepsilon^{ne}_{r;\infty}/h^2_{\max}$ | $\varepsilon^{ee}_{r;\infty}/h^4_{\max}$ |
| 16 | 0.39 | 0.21 | 0.19 | 0.03 |
| 32 | 0.20 | 0.24 | 0.21 | 0.04 |
| 64 | 0.098 | 0.24 | 0.22 | 0.04 |
| 128 | 0.049 | 0.24 | 0.22 | 0.04 |

second-order accuracy, confirmed by the observed $\varepsilon_{r;2}^n$ and $\varepsilon_{r;\infty}^n$ in Table 4.2. The errors were divided by the square of the largest cell width $h_{\max}$, which is the maximum value over all the cell widths in the three coordinate directions. The results in Table 4.2 show that the ENO interpolation reduces the overall errors, compared to standard cubic-spline interpolation, although the results are still second-order accurate. If we compare this to the result of ENO interpolation on the exact solution, marked by the superscript $ee$ and which is normalized to $h_{\max}^4$, we can conclude that the main contribution to the error is due to the numerical discretisation. Here, we used cubic ENO interpolation. The resulting interpolation errors reduce proportional to the fourth power of the step size, provided exact function values are given on the original grid.

We also investigated the effect of ENO interpolation when grid stretching was applied. The grid stretching is carried out in such a way that the ratio between neighbouring cell widths in each direction is $1 + \alpha$ when marching away from the origin. An equidistant grid is obtained for $\alpha = 0$. Table 4.3 lists the result for grid stretching with $\alpha = 0.04$. Similarly to the results without grid stretching in Table 4.2, the error is mainly caused by the numerical discretisation.

In these examples, we observe that the interpolation error is small relative to the second-order numerical discretisation error. Still, ENO interpolation provides some improvement over standard cubic-spline interpolation.

**Table 4.3**  As Table 4.2, but for a stretched grid.

| | | L$_2$ - ERROR | | |
|---|---|---|---|---|
| $N$ | $h_{\max}$ | $\varepsilon_{r;2}^n/h_{\max}^2$ | $\varepsilon_{r;2}^{ne}/h_{\max}^2$ | $\varepsilon_{r;2}^{ee}/h_{\max}^4$ |
| 16 | 0.45 | $8.2 \times 10^{-2}$ | $7.0 \times 10^{-2}$ | $1.3 \times 10^{-2}$ |
| 32 | 0.26 | $8.0 \times 10^{-2}$ | $6.9 \times 10^{-2}$ | $1.3 \times 10^{-2}$ |
| 64 | 0.17 | $7.4 \times 10^{-2}$ | $6.6 \times 10^{-2}$ | $1.1 \times 10^{-2}$ |
| 128 | 0.13 | $6.9 \times 10^{-2}$ | $6.3 \times 10^{-2}$ | $0.8 \times 10^{-2}$ |
| | | L$_\infty$ - ERROR | | |
| $N$ | $h_{\max}$ | $\varepsilon_{r;\infty}^n/h_{\max}^2$ | $\varepsilon_{r;\infty}^{ne}/h_{\max}^2$ | $\varepsilon_{r;\infty}^{ee}/h_{\max}^4$ |
| 16 | 0.45 | 0.18 | 0.16 | 0.03 |
| 32 | 0.26 | 0.16 | 0.14 | 0.03 |
| 64 | 0.17 | 0.15 | 0.13 | 0.03 |
| 128 | 0.13 | 0.14 | 0.13 | 0.04 |

**Layered models with current source**

The computational cost of the multigrid solver is typically of $O(N^3)$, meaning that the cost increases 8 times when the number of grid cells $N$ in each coordinate direction is doubled or the cell width is halved. For large-scale problems that require a relatively fine grid to accurately capture the solution, the cubic scaling with grid spacing may be an issue. Because the interpolation scheme is much cheaper than solving the equations on a finer grid, ENO interpolation may be useful. To assess the potential usefulness of ENO interpolation for obtaining the electric field at the receiver positions, we compared the result of ENO interpolation for a solution with a certain grid sampling to the result obtained by standard linear interpolation on a grid with a finer sampling.

For this comparison, we considered a homogeneous half space with a conductivity $\sigma$ of 0.5 S/m for $z \geq 0$ and zero elsewhere. A point dipole-source in the $x$-direction was placed at the surface. The frequency was set to 1 Hz. We computed the electric field with the multigrid solver on two different grids, containing either $128^3$ or $256^3$ cells. Both required five BiCGStab iterations to have the residual drop to $10^{-7}$ of its original value. This took about 35 minutes for the grid with $128^3$ cells and 6 hours for the one with $256^3$ cells. Next, we applied the cubic ENO interpolation and the standard linear interpolation scheme. Figure 4.2 shows the amplitude-versus-offset behaviour of the inline electric field, plotted together with its numerical error. Figure 4.2 confirms that the code provides a reasonably accurate solution, particularly for offsets larger than 100 m. The large error for the near field is due to the source modelling. To represent the point source on the grid, we used a Gaussian distribution of small width, centred at the source position. The standard deviation was set to 0.5 m. We interpolated the solution to the 400 points used in the graph by standard linear interpolation and also by ENO interpolation on the solution obtained for the $128^3$ grid cells.

In the example, the same interpolation scheme applied to the solution on the finer grid results in a smaller error than obtained for the coarser grid, particularly at the far offsets where the grid spacing differed significantly between the coarse and fine grid. We also find that the ENO interpolation on the solution obtained for $128^3$ cells produces a more accurate result than the standard linear interpolation applied to the solution on $256^3$ cells. Given the relatively low computational cost of the ENO interpolation, the usefulness of the method is clear.

The next example is a three-layer problem. We considered the performance of the ENO interpolation in a simple geophysical configuration with air, water, and sediments. The layers have a conductivity $\sigma$ of 0, 3, and 0.5 S/m, respectively, and a relative permittivity $\varepsilon_r$ of 1, 80, and 17. The water depth is 200 m. A dipole
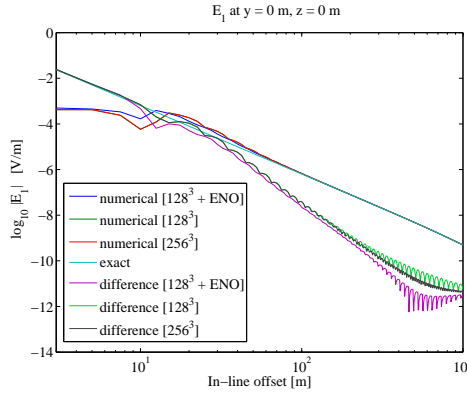
**Fig. 4.2**   Inline electric field component computed on two different grids. The numerical solutions match the exact solution, except close to the source. The difference between the numerical and exact solution is smallest with cubic ENO interpolation.

source in the $x$-direction is located at a depth of 175 m. The frequency is set to 0.5 Hz.

Here, we focus on the vertical electric field component along a vertical line because this component has discontinuities at the interfaces that separate two different resistivities and the ENO interpolation can be used to capture the discontinuities. Since we would like to avoid the error that comes from the numerical method, we used the exact solution. We first define an equidistant grid along the $z$-direction with a grid sampling of 10 m. The grid sampling is set in such a way that the interface of the discontinuity coincides with a grid point. We derived the exact solution, given in Appendix 4.2, by solving Maxwell's equations in the wave number domain and then taking the inverse Fourier transform to go back to the spatial domain (Ward and Hohmann, 1987).

Figure 4.3 shows the comparison. We plot the vertical electrical field component along a vertical line at position $x = 200$ m and $y = 0$ m. In the figure, we can see clearly that the vertical electrical field component has a discontinuity exactly at $z = 200$ m, the depth of the interface between the water and sediment layer. The zoomed figure in the right panel shows that the ENO interpolation captures the discontinuity quite well, whereas the standard cubic-spline interpolation produces an oscillation. The error also appears when we use the standard linear interpolation.
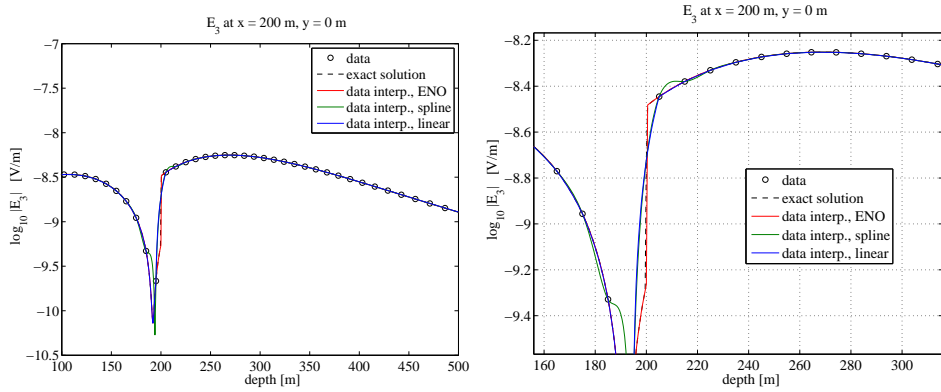
**Fig. 4.3** The vertical electric field component at $x = 200$ m and $y = 0$ m. The right panel shows an enlargement around the discontinuity.

**Modified three-layer problems**

In the previous example, the material discontinuities matched grid lines so they could be accurately represented in the numerical scheme. ENO interpolation then helps to capture the discontinuities in the solution. In general, the discontinuities will not be aligned with the lines of a Cartesian grid. The projection of the material properties onto the grid will then require some averaging. The averaging will affect the numerical solution. We investigate this case next. The previous three-layer problem is modified by having an abrupt change in water depth following a grid line. The numerical solution and interpolation results are then compared to the same problem where the grid is rotated relative to the model, so that the jump in water depth does not follow a grid line.

We added a simple bathymetry model to the previous three-layer problem by setting the water depth at either 200 m or 150 m with a jump at $x = 250$ m from deeper to shallower water when $x$ increases (see Figure 4.4). A dipole source in the $x$-direction was positioned at a depth of 175 m and at a 250 m distance from the jump in the water depth. We used the same frequency as before. An array of receivers was located at a depth of 200 m. We defined the grid points in such a way that the interface of the jump coincided with the grid lines (see the left panel of Figure 4.5). We will refer to this model as the regular configuration. Secondly, we used the same configuration but rotated the the grid lines by 30 degrees so that the interface of the jump no longer coincided with the grid lines (see the right-hand panel of Figure 4.5). The rotation centre is at the source location. We will call this the rotated configuration.

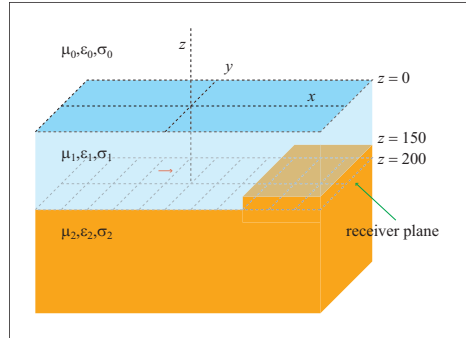We computed the numerical solution for the regular configuration with the

**Fig. 4.4**  A three-layer configuration with air, sea-water, and sediments and simple bathymetry.
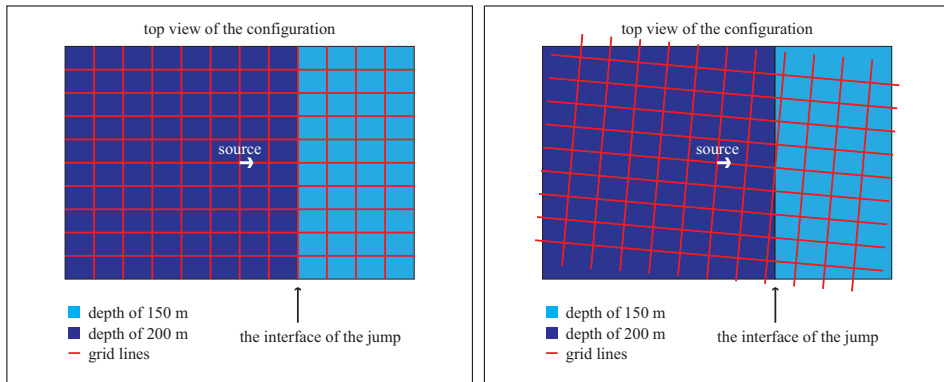


**Fig. 4.5**  The left panel shows a top view of a configuration where the grid is aligned with the jump in the sea bottom depth. The alignment is lost when the grid is rotated, as shown in the right panel.

multigrid solver containing $128^3$ cells, with cell widths varying from 25 m to about 5 km, and interpolated the result to the receiver locations with cubic ENO interpolation. Figure 4.6 shows the result at a depth of 200 m. As expected, the cubic ENO interpolation captures the discontinuity at the in-line distance of 250 m quite well. Further on, we will use this result as a reference to make a comparison between different interpolation methods.

We repeated the computations for the rotated configuration and interpolated the results to the same receiver locations as before. Figure 4.7 shows the result at a depth of 200 m for tri-linear and Figure 4.8 for cubic ENO interpolation. The difference between the solutions on the regular, aligned grid and the rotated one is indicative of the numerical error in the solution. The largest difference occurs near
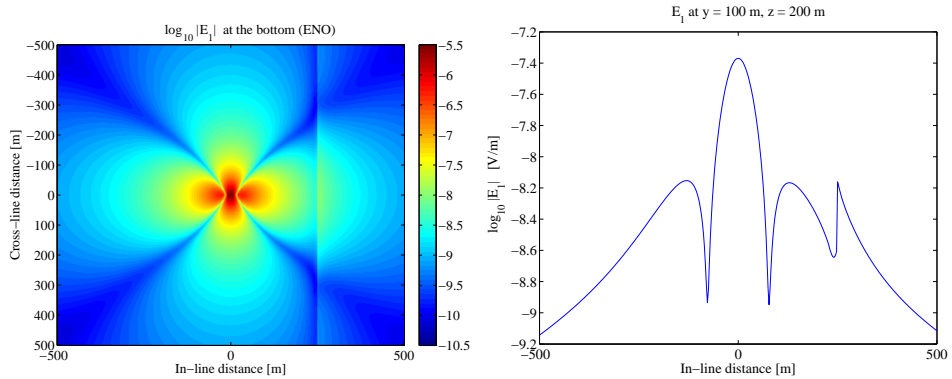
**Fig. 4.6**   The in-line electric field component at a depth of 200 m obtained with the aligned grid. The right panel shows the values along $y = 100$ m. Of course, sea bottom receivers can only be found for an in-line distance less than 250 m.

the discontinuity, where the tri-linear nor the cubic ENO interpolation can recover the jump in the solution. On the rotated grid, the jump is actually smoothed. In our modelling, the material parameters are assumed to be given as averages per cell. The projection of the original model to the rotated grid introduces some smoothing when computing these cell averages. This, is turn, causes the solution to be smoothed. ENO interpolation cannot remove this smoothing when used as a post-processing operation and hardly performs better than tri-linear interpolation in this case. Comparing Figures 4.7 and 4.8, we observe that the tri-linear interpolation produces a difference that is more oscillatory than obtained with the cubic ENO interpolant. This is due to the fact that the latter, which was also used for the reference curve, introduces more small-scale details than tri-linear interpolation.

## 4.4   CONCLUSIONS

The computation of accurate solutions to CSEM problems requires an accurate discretisation, a robust solver, and an accurate interpolation scheme to sample the numerical solution at receiver locations. We used a numerical scheme that provides the numerical solution as edge averages of the electric field components, each component living on the edges of cells that are parallel to the component's orientation. The interpolation of the edge averages of the possibly discontinuous field components to receiver positions was carried out with the ENO interpolation scheme, because this method can handle edge averages as well as discontinuities in the solution or derivatives of the solution.
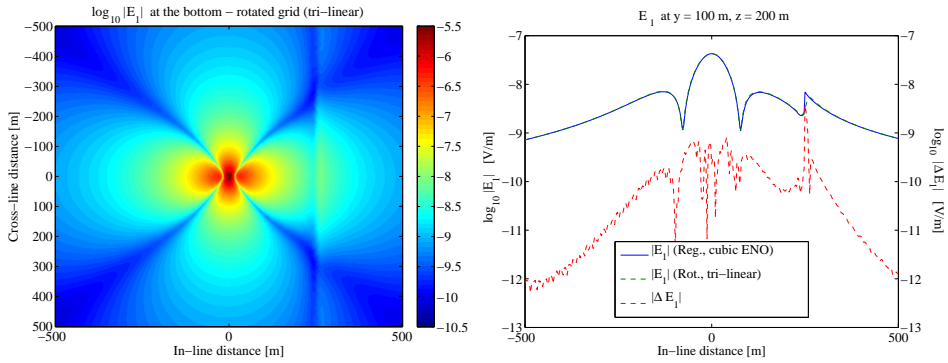
**Fig. 4.7**   The left panel shows the in-line electric field component at a depth of 200 m in the rotated configuration using standard tri-linear interpolation. The right panel compares values along $y = 100$ m. The solid blue line is the result of cubic ENO interpolation in the regular configuration, whereas the dashed green line was obtained with tri-linear interpolation in the rotated configuration. The dashed red line shows the differences between the two. The abbreviation 'Rot.' refers to the rotated configuration and 'Reg.' to the regular configuration. The differences are relatively small, except close to the discontinuity.
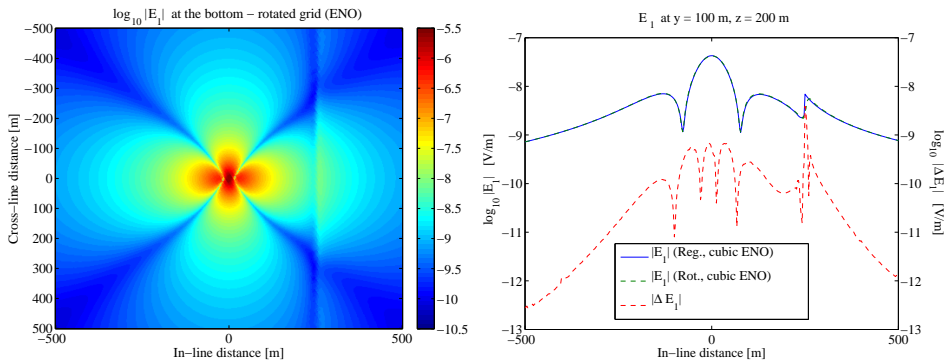


**Fig. 4.8**   As describe in Figure 4.7, but for cubic ENO interpolation.

Comparison to standard tri-linear or cubic interpolation shows that ENO interpolation provides more accurate results near discontinuities. Still, in the examples considered here, the discretisation error tends to dominate the final result and ENO interpolation only gives a moderate improvement. Given its low cost, it still appears to be worthwhile to use the scheme.

## APPENDIX 4.1:
## ONE-DIMENSIONAL ENO SCHEME

When computing a numerical solution for modelling 3D CSEM, or other problems, we have to discretise the equations on a grid. If we then want to sample computed field quantities at specific receiver locations, we need some kind of interpolation procedure. In many cases, it is sufficient to use a polynomial interpolation scheme.

The polynomial interpolation schemes that are widely used in applications are usually based on a fixed stencil. For instance, to get an interpolation result in cell $i$ with third-order accuracy, we can use information in the three cells $i - 1$, $i$, and $i + 1$ to construct a local quadratic polynomial, except of course if cell $i$ is located next to the boundary. This schemes works well for globally smooth solutions. However, when we apply this scheme for functions that have discontinuities, the fixed-stencil interpolation of second- or higher-order accuracy creates numerical oscillations near the discontinuities. This is referred to as the Gibbs phenomenon and is illustrated in Figure 4.9 on the left side.
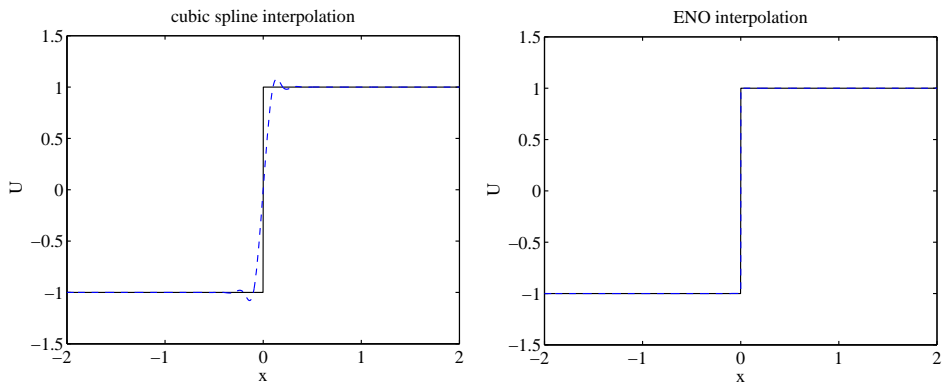


**Fig. 4.9** Cubic-spline interpolation with a fixed, centred stencil (left) and ENO cubic interpolation (right) for the sign function. Solid: exact function; dashed: interpolating polynomials.

The ENO interpolation is a higher-order interpolation scheme designed for piecewise smooth functions that contain discontinuities or have discontinuous first or higher derivatives. The scheme was originally proposed for compressible flow computations with shock waves and contact discontinuities and expanded on the earlier breakthrough work of van Leer (1979). Here we review the ENO scheme for reconstructing a function in one-dimensional space.

Suppose we are given a set of $N + 1$ points

$$(x_0, U_0), \quad (x_1, U_1), \quad \ldots, \quad (x_N, U_N),$$

where $U_i$ defines the value of a piecewise smooth function $U(x)$ at a point $x_i$, $i = 0, 1, \ldots, N$. We define cells, cell centres, and cell sizes, respectively, by

$$I_i := [x_i, x_{i+1}], \quad x_{i+\frac{1}{2}} := \frac{1}{2}(x_i + x_{i+1}),$$

and

$$\Delta x_i = x_{i+1} - x_i, \quad \text{for } i = 0, 1, \ldots, N - 1.$$

Here we assume no two $x_i$ are the same and that $\{x_i\}$ is properly ordered.

For a fixed value $m$, we want to reconstruct the function $U$ by finding $H_m(x)$, a piecewise polynomial function of $x$ with uniform polynomial degree $m$ that satisfies the following requirements:

1. For $h$ sufficiently small value, $H_m(x)$ approximates the function $U$ to $O(h^{m+1})$:
$$H_m(x) = U(x) + O(h^{m+1}),$$

    at all points $x$ for which there is a neighbourhood where $U$ is smooth.

2. It is essentially non-oscillatory:
$$TV(H_m) \leq TV(U) + O(h^{m+1}), \tag{4.4}$$

    where $TV$ denotes the total variation in $x$.

The inequality (4.4) above ensures that the function $H_m$ does not have spurious oscillations at a point of discontinuity. In the next paragraph we explain how to reconstruct the function $H_m$. The details and analysis of the reconstruction procedure can be found in Harten *et al.* (1986, 1997).

The function $H_m$ is reconstructed as follows:

$$H_m(x_i) := U_i, \quad \text{for } i = 0, 1, \ldots N,$$

and

$$H_m(x) := p_{m,i+\frac{1}{2}}(x), \quad \text{for } x \in I_i,$$

where $p_{m,i+\frac{1}{2}}$ is a polynomial function in $x$ of degree $m$. The half index $i + \frac{1}{2}$ is used to indicate that the local polynomial $p_{m,i+\frac{1}{2}}$ lives in interval $I_i$.
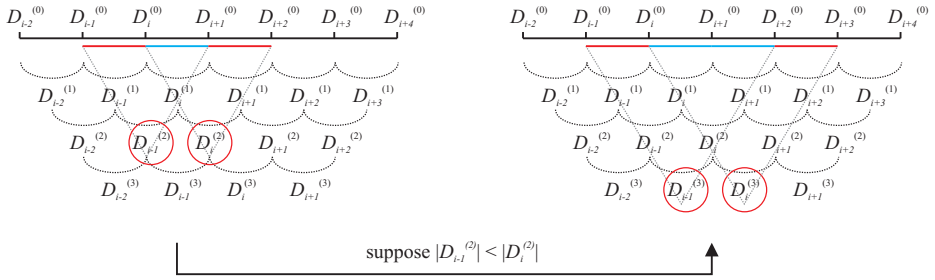
**Fig. 4.10** The ENO scheme adaptively determines a stencil for interpolation by selecting the smallest divided differences. Here, we use $D_i^{(k)} \equiv D[x_i, \ldots, x_{i+k}]$ for brevity.

The local polynomial $p_{m,i+\frac{1}{2}}$ is obtained using Newton interpolation at $(m+1)$ points that include $x_i$ and $x_{i+1}$. Clearly, there are many possibilities for $p_{m,i+\frac{1}{2}}$ since there are many combinations of $(m+1)$ points that include $x_i$ and $x_{i+1}$. In order to reduce the number of choices, and to make the numerical implementation easier, we set $p_{m,i+\frac{1}{2}}$ to be a polynomial that only passes through a stencil of $(m+1)$ successive points. This choice implies that we get exactly $m$ candidates $p_{m,i+\frac{1}{2}}$ corresponding to $m$ different stencils of $(m+1)$ successive points. For example, to construct an interpolating polynomial with second-order accuracy, we can use information of three points, either $\{x_{i-1}, x_i, x_{i+1}\}$ or $\{x_i, x_{i+1}, x_{i+2}\}$. Then, it only remains to choose which stencil would give the best approximation function $p_{m,i+\frac{1}{2}}$ on the interval $I_i$ in terms of getting the smoothest or least oscillatory polynomial.

The information about smoothness of the polynomial is extracted from the table of divided differences, which is defined recursively by:

$$D[x_i] := U_i,$$

and

$$D[x_i, \ldots, x_{i+k}] := \frac{D[x_{i+1}, \ldots, x_{i+k}] - D[x_i, \ldots, x_{i+k-1}]}{x_{i+k} - x_i}.$$

The divided differences themselves can be viewed as approximations to first and higher derivatives of function $U$. How we choose a stencil of $(m+1)$ points for which $p_{m,i+\frac{1}{2}}$ is smoothest, is basically the same problem as finding the interval where $U$ has the smallest divided differences.

Harten *et al.* (1997) proposed a non-linear adaptive algorithm to choose a

stencil of $(m + 1)$ points. Figure 4.10 illustrates how the algorithm works for 1D interpolation. We start by setting an initial stencil in the interval $[x_i, x_{i+1}]$, which correspond to a $p_{1,i+\frac{1}{2}}$ that is a first-degree (linear) polynomial. We proceed to obtain a second-degree interpolant by adding to the current interval either one cell to the left

$$[x_{i-1}, x_i] \cup [x_i, x_{i+1}],$$

or one cell to the right

$$[x_i, x_{i+1}] \cup [x_{i+1}, x_{i+2}].$$

The choice is based on the absolute values of the divided differences. If,

$$|D[x_{i-1}, x_i, x_{i+1}]| < |D[x_i, x_{i+1}, x_{i+2}]|,$$

we select the interval $[x_{i-1}, x_{i+1}]$ as the next stencil, otherwise we choose the interval $[x_i, x_{i+2}]$. This procedure is repeated for larger stencils and higher-degree polynomials. Let us assume that we have already a stencil of $k + 1$ points that corresponds to the $k$-th degree smoothest polynomial at cell $I_i$,

$$[x_{j_i}, x_{j_i+k}], \quad \text{for some } j_i.$$

Then, to obtain the $(k + 1)$-th degree smoothest polynomial at cell $I_i$, we proceed by adding to the interval $[x_{j_i}, x_{j_i+k}]$ either one cell to the left,

$$[x_{j_i-1}, x_{j_i}] \cup [x_{j_i}, x_{j_i+k}],$$

or one cell to the right

$$[x_{j_i}, x_{j_i+k}] \cup [x_{j_i+k}, x_{j_i+k+1}].$$

The choice is based on the absolute values of $D[x_{j_i-1}, \ldots, x_{j_i+k}]$ and $D[x_{j_i}, \ldots, x_{j_i+k+1}]$. If,

$$|D[x_{j_i-1}, \ldots, x_{j_i+k}]| < |D[x_{j_i}, \ldots, x_{j_i+k+1}]|,$$

we select the interval $[x_{j_i-1}, x_{j_i+k}]$ as the next stencil, otherwise we choose the interval $[x_{j_i}, x_{j_i+k+1}]$.

We can generalize the ENO interpolation to multi-dimensional spaces by repeating the one-dimensional procedure above. However, we cannot directly use the approach in our 3D CSEM modelling code, because the electric field values are computed as edge averages, whereas the ENO scheme outlined in the previous section acts on point values. For edge averages, we have to consider the primitive function.

Given cell averages $\overline{u}_{i+\frac{1}{2}}$ of a piecewise smooth function $u(x)$ at the centre of each cell,

$$\overline{u}_{i+\frac{1}{2}} = \overline{u}(x_{i+\frac{1}{2}}) := \frac{1}{\Delta x_i} \int_{x_i}^{x_{i+1}} u(x)\, dx, \quad \text{for } i = 0, 1, \ldots, N-1.$$

we can evaluate the point values of the primitive function, $U(x) = \int_{x_0}^{x} u(s)\, ds$, by

$$U(x_i) = \sum_{k=0}^{i} \overline{u}_{k+\frac{1}{2}} \Delta_{k+\frac{1}{2}}.$$

The lower bound $x_0$ can be chosen arbitrary. Since $u = dU/dx$, we can apply ENO interpolation to the point values of the primitive function $U$ and then obtain an approximation to $u$, $r(x)$, by defining

$$r(x) := \frac{d}{dx} H_m(x).$$

In the 3D CSEM modelling, we applied the ENO interpolation as follows. First, we interpolate the data in the in-line direction with the help of the primitive function. The results are then interpolated by the point-wise ENO scheme in the two perpendicular directions.

We end this section by noting that the selection of the smoothest stencil by means of an if-statement may pose problems if the modelling code is used for least-squares inversion of electromagnetic measurements. Then, a differentiable version can be employed as proposed by van Albada *et al.* (1982); see also Mulder and van Leer (1985).

## APPENDIX 4.2:
## THE VERTICAL COMPONENT IN THE THREE-LAYER PROBLEM

The vertical electric field component in the three-layer problem can be derived explicitly by solving Equation 4.3 in the wave number domain and then taking the inverse Fourier transform to go back to the spatial domain (Ward and Hohmann, 1987).

We consider a three-layer problem in an unbounded domain and number the top layer and the two layers below as 0, 1, and 2, respectively. Layer 1 has a thickness $d$. Each layer has different parameters, $\mu$, $\varepsilon$, and $\sigma$. A coordinate system is defined such that the origin is located at the interface of layer 0 and layer 1. A point source in the $x$-direction is placed at coordinate $(0, 0, z^s)$, $0 < z^s < d$.

Maxwell's equations for 1D layered media can be decomposed in either the horizontal electric and magnetic field components or the vertical electric and magnetic field components and their vertical derivatives. Both decomposition methods fully describe the total electromagnetic field. The latter method is of interest because the vertical electric field component is completely decoupled from the vertical magnetic field component. Here we are only interested in the vertical electric field and we choose to eliminate all horizontal components of the electromagnetic field. With this configuration, the vertical electric field component at a specific point $\mathbf{x} = (x, y, z)$ anywhere in the three-layered model is given by

$$E_z(\mathbf{x}, \omega) = \begin{cases} E_{z,0}(\mathbf{x}, \omega), & \text{for } z < 0; \\ E_{z,1}(\mathbf{x}, \omega), & \text{for } 0 < z < d; \\ E_{z,2}(\mathbf{x}, \omega), & \text{for } z > d. \end{cases}$$

This expression is obtained by solving the following boundary value problem for the vertical electric field that is generated by a unit-strength $x$-directed electric current dipole source with an impulsive time-signature:

$$\tilde{E}_{z,0} = \tilde{A}_0^- \exp(\Gamma_0 z), \text{ for } z < 0,$$

$$\tilde{E}_{z,1} = \frac{\mathrm{i}k_x}{2\eta_1} \mathrm{sign}(z - z^s) \exp(-\Gamma_1 |z - z^s|)$$

$$+ \tilde{A}_1^+ \exp(-\Gamma_1 z) + \tilde{A}_1^- \exp[-\Gamma(d - z)], \text{ for } 0 < z < d,$$

$$\tilde{E}_{z,2} = \tilde{A}_2^+ \exp[-\Gamma_2(z - d)], \text{ for } z > d,$$

where $\tilde{A}_i^+$ denotes the amplitude of the down-going field and $\tilde{A}_i^-$ of the up-going field in layer $i$. The vertical wave number of layer $i$ is denoted by $\Gamma_i$ and given by

$$\Gamma_i = \sqrt{\kappa^2 - \mathrm{i}\omega\mu_0\eta_i}, \qquad \mathrm{Re}\,(\Gamma) \geq 0,$$

where $\kappa^2 = k_x^2 + k_y^2$ and $\eta_i = \sigma_i - \mathrm{i}\omega\varepsilon_i$. The boundary conditions require the vertical electric current to be continuous and the vertical derivative of the vertical electric field to be continuous across any source-free interface with a discontinuity in the electric medium parameters. This leads to four conditions for the four unknown field amplitudes in the three layers, which problem can be solved for the up- and down- going field amplitudes. We use the solution only for the field

components in the lower two layers, which leads to

$$E_{z,1}(\mathbf{x}, \omega) = 3\frac{x(z - z^s)}{R^2}\left(\frac{1}{R^2} + \frac{\gamma_1}{R}\right)\frac{\exp(-\gamma_1 R)}{4\pi\tilde{\sigma}_1 R}$$

$$+ i\omega\mu_0\frac{x(z - z^s)}{R^2}\frac{\exp(-\gamma_1)}{4\pi R}$$

$$+ \frac{x}{2\pi r}\int_{\kappa=0}^{\infty}(\tilde{E}_1^+(\kappa, z, \omega) + \tilde{E}_1^-(\kappa, z, \omega))J_1(\kappa r)\kappa^2\,\mathrm{d}\kappa,$$

$$E_{z,2}(\mathbf{x}, \omega) = \frac{x}{2\pi r}\int_{\kappa=0}^{\infty}\tilde{E}_2^+(\kappa, z, \omega)J_1(\kappa r)\kappa^2\,\mathrm{d}\kappa,$$

and

$$\tilde{E}_1^+(\kappa, z, \omega) = \frac{\exp[-\Gamma_1(z + z^s)] - r_1^{TM}\exp[-\Gamma_1(2d + z - z^s)]}{1 + r_0^{TM}r_1^{TM}\exp(-2\Gamma_1 d)}$$

$$\times\frac{r_0^{TM}}{2\tilde{\sigma}_1},$$

$$\tilde{E}_1^-(\kappa, z, \omega) = \frac{\exp[-\Gamma_1(2d - z - z^s)] + r_0^{TM}\exp[-\Gamma_1(2d - z + z^s)]}{1 + r_0^{TM}r_1^{TM}\exp(-2\Gamma_1 d)}$$

$$\times\frac{r_1^{TM}}{2\tilde{\sigma}_1},$$

$$\tilde{E}_2^+(\kappa, z, \omega) = \frac{\exp[-\Gamma_1(d - z^s)] + r_0^{TM}\exp[-\Gamma_1(d + z^s)]}{1 + r_0^{TM}r_1^{TM}\exp(-2\Gamma_1 d)}$$

$$\times\frac{(1 + r_1^{TM})}{2\tilde{\sigma}_2}\exp[-\Gamma_2(z - d)].$$

The radial distance in the horizontal plane is given by $r = \sqrt{x^2 + y^2}$ and the total distance is given by $R = \sqrt{x^2 + y^2 + (z - z^s)^2}$. The quantities $\gamma_i = \sqrt{-\imath\omega\mu_i\tilde{\sigma}_i}$, $\Gamma_i = \sqrt{\kappa^2 - \imath\omega\mu_i\tilde{\sigma}_i}$, where $\tilde{\sigma}_i = \sigma_i - \imath\omega\varepsilon_i$.

The reflection coefficients are given by

$$r_0^{TM} = \frac{\tilde{\sigma}_1\Gamma_0 - \tilde{\sigma}_0\Gamma_1}{\tilde{\sigma}_1\Gamma_0 + \tilde{\sigma}_0\Gamma_1}\quad\text{and}\quad r_1^{TM} = \frac{\tilde{\sigma}_2\Gamma_1 - \tilde{\sigma}_1\Gamma_2}{\tilde{\sigma}_2\Gamma_1 + \tilde{\sigma}_1\Gamma_2}.$$

The two remaining Fourier-Bessel integrals are evaluated numerically using an adaptive 8-point Gauss quadrature for every receiver location separately.

# Part II

# EM Monitoring

# 5 A feasibility study of land CSEM reservoir monitoring in a complex 3D model

**SUMMARY**

We carried out a series of numerical simulations in a complex 3D resistivity model to investigate the feasibility of using controlled-source electromagnetics on land for monitoring changes in a hydrocarbon reservoir during production. Displacement of oil by saline water injection changes the resistivity. The modelling allows a comparison of the measured time-lapse EM signal to various sources of noise that can be expected in a field experiment, for instance, magnetotelluric signals, repeatability errors, and near-surface resistivity changes caused by seasonal variations. Our estimates show that land CSEM monitoring should be feasible, though not easily, for the example considered here, a thick reservoir at a depth of about one kilometer. The trade-off between signal strength and repeatability errors requires the source to be located at some distance from the reservoir. Measurements in a monitoring well suffer less from surface noise. Measuring the vertical electric component in a well, placed at some distance from the reservoir, provides the best result.

## 5.1   INTRODUCTION

The controlled-source electromagnetic (CSEM) method for hydrocarbon explo-
ration was introduced in the 1980s by the Scripps Institution of Oceanography
(Cox, 1981; Cox *et al.*, 1986; Evans *et al.*, 1991), the University of Toronto
(Cheesman *et al.*, 1987), and Cambridge University (Evans *et al.*, 1991). Com-
mercial acceptance was reached much later (Eidesmo *et al.*, 2002; Ellingsrud *et al.*,
2002). Since then, the marine CSEM method received more and more attention
from the oil and gas industry. CSEM surveys on land have a longer history and
have been carried out in, for instance, Russia, China, and India (Spies, 1983; He
*et al.*, 2007; Strack and Pandey, 2007). In some cases, CSEM measurements were
used as the only exploration tool. In other, it complemented seismic surveys by
providing an indication of the resistivity of targets identified by seismic imaging
(Eidesmo *et al.*, 2002; Darnet *et al.*, 2007; MacGregor *et al.*, 2007). This informa-
tion can improve the probability of success in hydrocarbon exploration. Marine
CSEM measurements are mostly processed in the frequency domain, whereas for
land applications, both the time domain and the frequency domain are used.

  A potential application of controlled-source EM is monitoring a hydrocarbon
reservoir during the recovery process.  Oil production with water flooding or
steam injection, for instance, creates resistivity changes in the subsurface. These
changes occur primarily in the reservoir. Smaller effects may be caused by changes
in the near surface.  A central question in EM monitoring is whether or not
resistivity changes in the reservoir are detectable, and if so, if the value of that
information is worth the effort compared to more established methods as time-
lapse seismic measurements (Landrø *et al.*, 2003; Vasco *et al.*, 2008) that provide
far better resolution, but not necessarily of the same quantity.  In the EM case,
spatial resolution will always be poor due to the diffusive character of EM signals
in the earth at the low frequencies required to reach sufficient depth (Ward
and Hohmann, 1987). However, EM measurements are more sensitive to fluid
properties than seismic measurements, especially when comparing highly resistive
oil to low-resistivity brine.  Although it would be interesting to compare or
combine the CSEM data with other geophysical data sets, we do not consider that
here. Instead, we focus on the feasibility of CSEM reservoir monitoring.

  Several authors have undertaken an assessment of the feasibility of CSEM
monitoring, for example Lien and Mannseth (2008), Orange *et al.* (2009), and
Black and Zhdanov (2009). They all presented a modelling study of the CSEM
monitoring problem for marine applications. Lien and Mannseth (2008) and
Black and Zhdanov (2009) employed a 3D integral-equation method to model the
time-lapse effect of the flooding front during water injection into an oil reservoir.

Orange *et al.* (2009) used an accurate 2D finite-element modelling code to study several scenarios for depleting a reservoir, including lateral and bottom flooding, stacked reservoirs, and partial depletion. Here, we use a 3D finite-volume code to study oil displacement by a water drive in a complex 3D resistivity model and to assess if time-lapse changes are detectable with the land CSEM method.

From a practical point of view, monitoring the reservoir onshore is much easier than offshore, although the noise influence on EM data could be much stronger compared to the marine case. Also, the accessibility of certain land areas may be restricted. In a marine environment with EM detectors on the sea bottom, the presence of several hundreds of meters of salt water will shield magnetotelluric and man-made EM signals, at least at higher frequencies. Also, source and receiver coupling are less of an issue. On the other hand, sea water currents create electric disturbances that increase the amount of background noise. On land, source and receiver coupling is a problem, as are natural and cultural sources of EM "noise". Land measurements are also susceptible to near-surface effects due to seasonal and diurnal changes, weather conditions such as rainfall and frost, and variations in ground water level. Both on land and in the sea, instrument noise and dynamic range play a role. Differences in positioning and variations in instrument properties cause repeatability errors. Still, a relative accuracy of the order of one percent should be feasible with careful and extensive calibration and pre-processing.

In this chapter, we present a modelling study with the aim to investigate the potential use of land electromagnetic measurements for reservoir monitoring. We selected a reasonably complex geological model. In that model, we conducted numerical experiments to study the sensitivity of EM data to changes in an oil-bearing reservoir due to water injection. We assume that the CSEM measurements are available in the frequency domain. We considered measurements with sources and receivers at the surface as well as an acquisition geometry with sources at the surface and receivers in a monitoring well. We included noise and repeatability errors to assess the feasibility of land CSEM reservoir monitoring.

The outline of the chapter is as follows. We first review the governing equations in the frequency domain, their discretisation, and the solution method. Next, we describe the 3D model with the oil reservoir. We then investigate various aspects of CSEM monitoring, such as the choice of frequency and the effect of the position of the source on the time-lapse data. After examining the surface-to-surface case, we consider sources at the surface and receivers in a monitoring well. The effect of various kinds of noise, both additive and multiplicative, is studied in section 5.6 and affects the choice of acquisition geometry.

## 5.2   METHOD

In this section, we review the governing equations, their finite-volume discretisation, and the numerical solution method. The electromagnetic wavefields are the electric field, $\hat{\mathbf{E}}(\mathbf{x}, t)$, and the magnetic field, $\hat{\mathbf{H}}(\mathbf{x}, t)$. Here $\mathbf{x} = (x_1, x_2, x_3)$ denotes the Cartesian coordinate vector and $t$ is time. As usual, the $x_3$-axis is pointing downward. We define the temporal Fourier transform of a space- and time-dependent vector field $\hat{\mathbf{E}}(\mathbf{x}, t)$ as

$$\mathbf{E}(\mathbf{x}, \omega) = \int_{-\infty}^{\infty} \hat{\mathbf{E}}(\mathbf{x}, t) e^{i\omega t} \, dt,$$

where $i$ is the imaginary unit and $\omega$ the angular frequency. The behaviour of electric field in conducting media can be described by Maxwell's equations and Ohm's law (c.f. Ward and Hohmann (1987); Jackson (1999); Griffiths (1999)). In the frequency domain at an angular frequency $\omega$, these can be combined into

$$i\omega\mu_0\tilde{\sigma}\mathbf{E} - \nabla \times \mu_r^{-1}\nabla \times \mathbf{E} = -i\omega\mu_0\mathbf{J}_s, \qquad (5.1)$$

where $\mathbf{J}_s(\mathbf{x}, \omega)$ denotes the current source. The parameters $\tilde{\sigma}(\mathbf{x}) = \sigma - i\omega\varepsilon_0\varepsilon_r$, with $\sigma(\mathbf{x})$ the conductivity, $\varepsilon_r(\mathbf{x})$ the relative permittivity, $\mu_r(\mathbf{x})$ the relative permeability, and $\varepsilon_0$ and $\mu_0$ their absolute values in vacuum. The magnetic field, $\mathbf{H}$, follows from the relation

$$\nabla \times \mathbf{E}(\mathbf{x}, \omega) = -i\omega\mu_r\mu_0\mathbf{H}(\mathbf{x}, \omega).$$

To compute a numerical solution of Equation 5.1 for a given conductivity and source term, we discretised the equations on a tensor-product cartesian grid allowing for grid stretching. Here, we employed the Finite Integration Technique (Weiland, 1977), which can be considered as a finite-volume generalisation of the scheme by Yee (1966). The discretisation starts with a grid of block-shaped cells. The three electric field components are represented as average value on edges, the $x$-component on edges parallel to the $x$-direction and likewise the $y$- and $z$-component parallel to their corresponding directions.

Perfectly electric conducting (PEC) boundary conditions, namely $\mathbf{E} \times \mathbf{n} = 0$ with $\mathbf{n}$ the normal to the boundary, are used where the model is truncated. To avoid undesirable boundary effects, we added a boundary strip of about five skin depths around the model. For the air layer, an even thicker layer is added. Grid stretching is necessary to balance the need for an accurate solution around the area of interest and the limitations of available computer memory. Several conflicting

requirements guide the choice of the grid. We refer to the paper by Plessix *et al.* (2007) for more details.

Discretisation of the system of equations (5.1) together with the PEC boundary conditions leads to a linear system of the form

$$\mathbf{L}^h \mathbf{E}^h = \mathbf{f}^h,$$

where $\mathbf{L}^h$ is the discrete Maxwell operator, $\mathbf{E}^h$ the vector of the discrete values of the electric field, and $\mathbf{f}^h$ the source vector. The matrix $\mathbf{L}^h$ is large, symmetric but not hermitian, and sparse. We solved the discrete equations with an iterative method, BiCGStab2 (van der Vorst, 1992; Gutknecht, 1993), preconditioned by a multigrid solver (Mulder, 2006). The method is matrix-free: we never explicitly form the large sparse linear matrix that describes the discretised problem but only evaluate its action on the latest estimate of the solution, thereby reducing storage requirements. For applications of this solver, we refer to Mulder (2006), Plessix *et al.* (2007), and Mulder *et al.* (2008).

Equation 5.1 in operator notation reads

$$\mathbf{L}_\sigma \mathbf{E} = \mathbf{f}, \tag{5.2}$$

where $\mathbf{L}_\sigma = i\omega\mu_0\tilde{\sigma} - \nabla \times \mu_r^{-1}\nabla\times$, and $\mathbf{f} = -i\omega\mu_0\mathbf{J}_s$. Suppose we have a background model $\sigma_b$ and electric field $\mathbf{E}_b$ that satisfies

$$\mathbf{L}_{\sigma_b} \mathbf{E}_b = \mathbf{f}. \tag{5.3}$$

By letting $\mathbf{E} = \mathbf{E}_b + \mathbf{E}_s$ where $\mathbf{E}_s$ is the secondary solution that we want to compute, Equation 5.2 can be rewritten as

$$\mathbf{L}_\sigma \mathbf{E}_b + \mathbf{L}_\sigma \mathbf{E}_s = \mathbf{f}. \tag{5.4}$$

This separation can be performed because the operator $\mathbf{L}_\sigma$ is linear with respect to the field $\mathbf{E}$. Since the operator $\mathbf{L}$ is also linear with respect to the model parameter $\sigma$, the first term on the left-hand side can be expressed as $\mathbf{L}_\sigma \mathbf{E}_b = \mathbf{L}_{\sigma_b}\mathbf{E}_b + \mathbf{L}_{\sigma_s}\mathbf{E}_b$, where $\sigma_s = \sigma - \sigma_b$. Then, by substituting Equation 5.3 into Equation 5.4, we obtain the system of equations for the secondary solution,

$$\mathbf{L}_\sigma \mathbf{E}_s = -\mathbf{L}_{\sigma_s}\mathbf{E}_b.$$

The secondary system of equations is the same as the original one except for the source term.

The primary-secondary field formulation does not change the convergence speed of the iterative method, but may provide more accurate results, for instance, when the source resembles a delta function. In that case, the solution will be singular close to the source and a rather fine grid will be required to resolve the singular behaviour of the electric field. The primary-secondary formulation allows for an analytical treatment of the source singularity and, therefore, does not require very small cells close to the source point. We used the exact solution for a homogeneous half space (Raiche and Coggon, 1975) with a resistivity equal to that at the source location as the primary field.

## 5.3   BASE MODEL

As a starting point for studying the monitoring problem, we modified the Overthrust model (Aminzadeh *et al.*, 1997) to obtain a realistic and complex subsurface resistivity, replacing velocities by resistivities according to $\rho = (v/1700)^{3.88}$, as suggested by Meju *et al.* (2003). Here, $v$ is the velocity in m/s and $\rho$ the resistivity in $\Omega$m. The model has a size of 20 km by 20 km by 4.7 km.

In the 3D model, we selected one part as an artificial reservoir sand that contains oil and water. We then defined two different states, the initial condition of the reservoir and a later state where part of the oil has been replaced by water. For simplicity, we assumed that the recovery process only affects the configuration of oil and water in the reservoir, so that the differences in the time-lapse data are entirely due to changes in this part. We start with this idealized situation and will make modifications later on.

Figure 5.1 shows a vertical slice through the model at $y = 3000$ m for two different states, the initial condition of the reservoir and a later state where the oil-water contact has risen 100 m after water injection. We will start with the assumption of 100% sweep efficiency, meaning perfect replacement of oil by water. Archie's law (Archie, 1942) relates the in-situ resistivity of sedimentary rock to its porosity and water saturation by

$$\rho_t = \rho_w \phi^{-m} S_w^{-n},$$

where $\phi$ denotes the porosity, $\rho_t$ the resistivity of the fluid saturated rock, $\rho_w$ represents the resistivity of the water, and $S_w$ the water saturation. The constants $m$ and $n$ are the cementation and saturation exponents, respectively. Archie (1942) found that $m$ is approximately 1.8 to 2.0 for consolidated sandstones and 1.3 for clean, unconsolidated sands. He also determined that the saturation exponent is approximately 2.0. If we use 2.0 for both constants $m$ and $n$ and assume that the
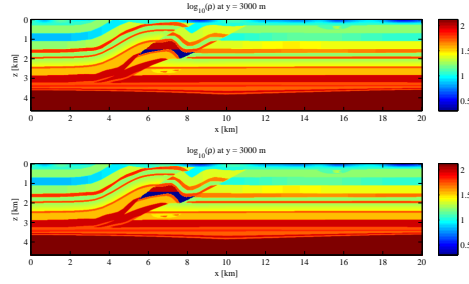
**Fig. 5.1** Resistivity based on the SEG/EAGE Overthrust model. The reservoir formation lies around $x = 6$ km and between 1.4 and 2.0 km depth in this section of the model. The dark blue part shows the injected water. The oil-bearing sand above it is coloured dark red. In the middle panel, the oil-water contact has moved up 100 m relative to top panel.
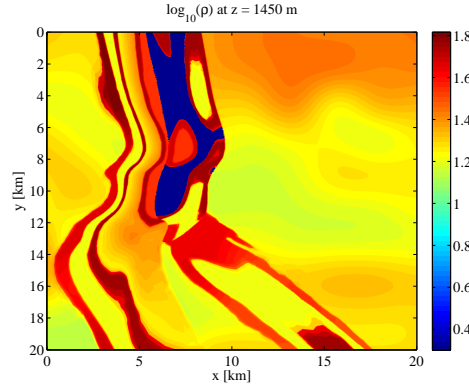


**Fig. 5.2** A horizontal cross-section of the bottom panel of Figure 5.1 at 1450 m depth.

saturated rock has a porosity of 40% and a water saturation of 100%, we obtain a resistivity of about 2 $\Omega$m, given a resistivity of 0.33 $\Omega$m for the salt water injected during the recovery process. The resistivity in the oil-bearing part of the reservoir sand is set to 100 $\Omega$m.

We added extra boundary strips of about five skin depths in the $x$- and $y$-directions and at the bottom of the model to avoid undesirable boundary effects. The skin depth at a frequency $f$ is $1/\sqrt{\pi f \sigma \mu}$, where $\sigma$ is the conductivity and $\mu$ the permeability. In our case, $\sigma$ is set to 0.5 S/m and $\mu$ is set to its vacuum value, $\mu_0 = 4\pi\ 10^{-7}$ H/m. On the top of the model, we added an air layer with resistivity value of $10^{11}$ $\Omega$m and a thickness of about 40 km. We defined a computational grid with 128 by 128 by 128 cells, leading to over 2 million
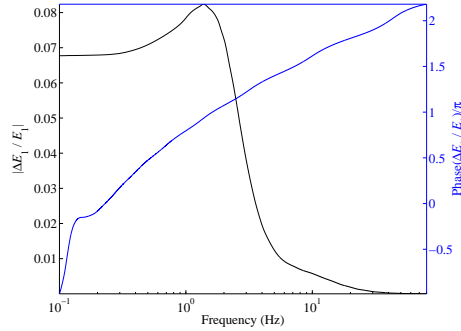
**Fig. 5.3**   Relative difference of the electric field components in $x$-direction, $E_1$, for a receiver at (7000, 11375, 0) m or 5 km distance from the source. Both the amplitude and the normalized unwrapped phase angle (the unit is $\pi$ or 180°) are shown.

grid points with about 6 million unknowns. The cell widths of the stretched grid varied from 25 m to about 5 km. A finer grid would increase the computational time. Later on, we will assess the numerical accuracy by comparing results for $128^3$ and $256^3$ grid cells.

## 5.4   SURFACE-TO-SURFACE EM

We consider time-lapse EM effects due to resistivity changes during reservoir depletion with a water drive. We assume simple bottom depletion in which the oil-water contact has moved up 100 m as would happen as a result of water injection in the deeper parts of the reservoir by means of a horizontal well. We start with the assumption of 100% sweep efficiency. Although this assumption is over-optimistic, the difference between 100% and more reasonable sweep efficiency will not be too dramatic. This is because the resistivity contrast between mixture-saturated part and oil-bearing is still high. If, for example, the sweep efficiency is 40%, Archie's law predicts a resistivity around 10 $\Omega$m for the rock that contains the oil-water mixture. This is still a small number compared to the resistivity of the oil-bearing part. Later on, we will show a comparison between 100% and 40% sweep efficiency.

We first determine the frequency that is most sensitive to the change in the reservoir. We measured the time-lapse change in a surface-to-surface configuration, placing both the source and the receivers on the surface. A unit dipole source in the $x$-direction is positioned at (2000, 11375, 0) m. We placed a receiver at (7000, 11375, 0) m and then computed the in-line electric field $E_1$. Figure 5.3 shows the in-line electric field components as a function of frequency. We observe the largest

relative difference between 1 and 2 Hz, whereas the difference rapidly decreases above 2 Hz. The relative differences for frequencies above 5 Hz are smaller than 1% because of the strong attenuation of high-frequency electromagnetic waves in the earth.

Figure 5.4 displays the amplitude behaviour of time-lapse difference for the in-line electric field measured on the surface. We still assume idealized conditions, i.e., the difference is entirely due the resistivity change in the reservoir. The time-lapse resistivity changes are examined by considering the amplitudes of the absolute as well as the normalized differences of the electric field. Measuring the absolute differences is useful to identify domains with signal changes above the noise floor, which is independent of the signal strength, while measuring the normalized differences is useful to identify domains with signal changes that lie above a noise level and are proportional to the signal strength, such as the repeatability errors. The results in top panels of Figure 5.4 show the effect of frequency on the absolute amplitude of the difference. The high frequency on the left provides a far better resolution than the lower frequencies to the right. The plots in bottom panels of Figure 5.4 display the relative change $|\Delta E_1|/\sqrt{|E_1|^2 + |E_2|^2}$ on a logarithmic scale. We impose a lower bound of 1% for the multiplicative noise, because we assume that repeatability errors only allow for reliable measurements of relative differences above 1%. We observe that the resistivity change at 10 Hz can hardly be detected, but that we have a clear effect above the reservoir at 1 and 0.1 Hz. Figure 5.4 shows that at 10 Hz, the time-lapse change is more spatially confined to the reservoir region but that their amplitude is too small to be detectable because the attenuation is too strong at this high frequency.

As already stated, we used a computational grid with 128 by 128 by 128 cells, with cell widths varying from 25 m to about 5 km. Convergence, with a relative drop in the residual of $10^{-7}$, took about 30 minutes using a 2.2-GHz AMD Opteron with 16 GB of memory. We oversampled the result on a very fine grid using standard trilinear interpolation. To check if the result is accurate enough, we ran the same simulation but now with a finer grid of 256 by 256 by 256 cells. The number of iterations to reach convergence remained the same. Figure 5.5 displays the amplitude behaviour of the in-line electric field with the initial model at 1 Hz using two computational grids. We observe that the responses display the same qualitative behaviour either with $128^3$ or with $256^3$ cells. There are certainly differences between those two results as indicated by the dashed line in Figure 5.5, but the values are relatively small and seem to be below 1%. This is smaller than the assumed size of the repeatability errors. Figure 5.6 displays the amplitude behaviour of time-lapse difference at 1 Hz using the two computational grids. Again, we observe that the results display the same qualitative behaviour for the
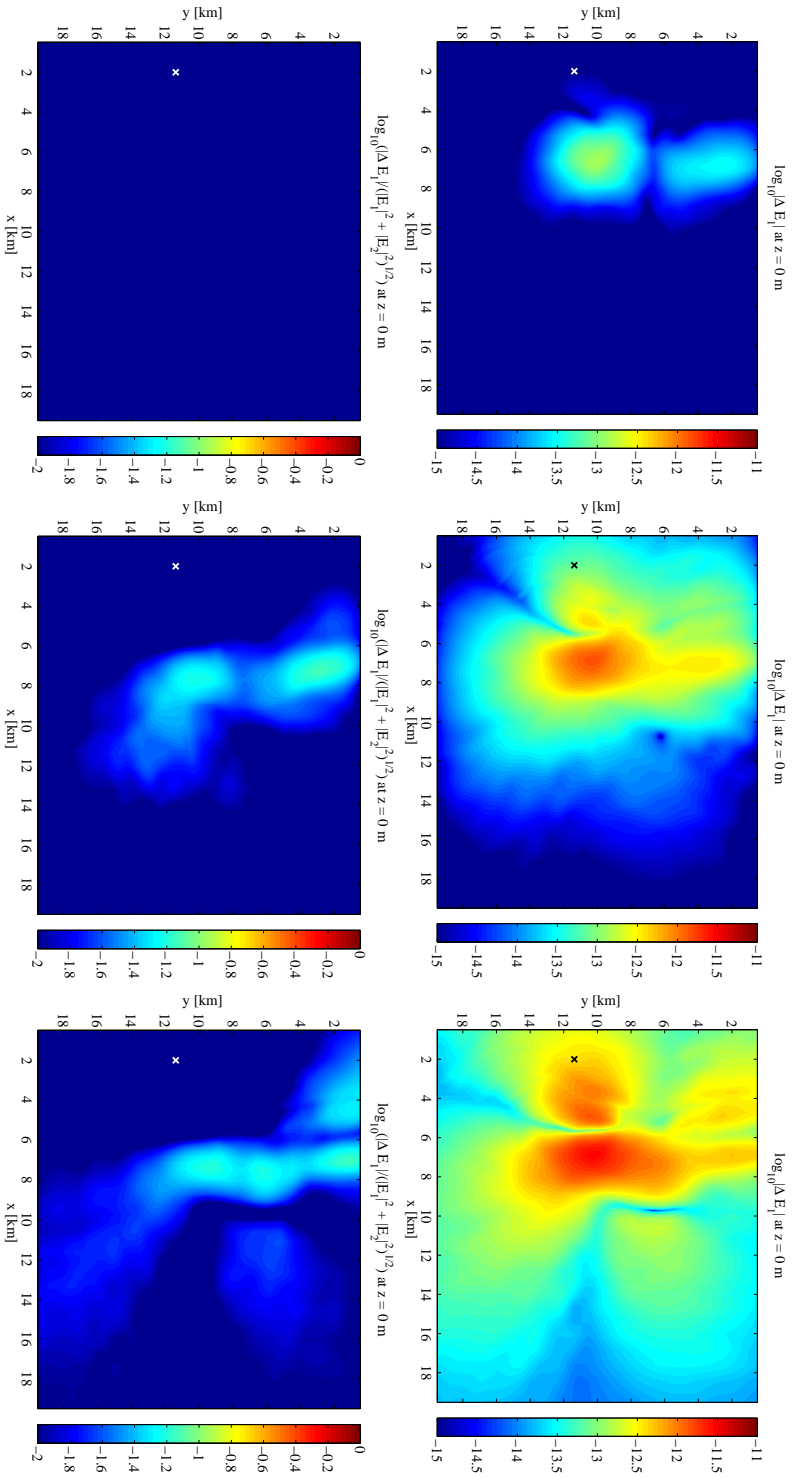
**Fig. 5.4**  The top panels display the time-lapse differences of the in-line electric field observed on the surface (top view) at frequencies of 10, 1, and 0.1 Hz, from left to right. The bottom panels display the normalized fields with amplitudes below 1% suppressed, as these are assumed to be dominated by noise. The small white cross marks the lateral location of the HED source.
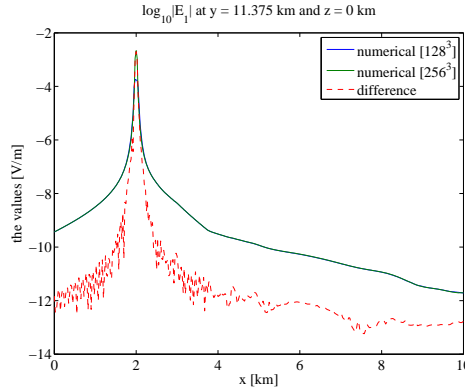
**Fig. 5.5**    The amplitude behaviour of the electric field components in $x$-direction, $E_1$, for a receiver array at $(y, z) = (11375, 0)$ m. The legend with 'numerical [$128^3$]' means the result computed with $128^3$ cells, while 'numerical [$256^3$]' is with $256^3$ cells.

result obtained with $128^3$ or with $256^3$ cells. Small differences can be observed in the absolute time-lapse variations, displayed in the two top panels of Figure 5.6, but the numerical errors are less obvious in the normalized time-lapse differences shown at the bottom. We conclude that it is sufficient for our purpose to use the computational grid with $128^3$ cells. We refer to Mulder (2006, 2008) and Mulder *et al.* (2008) for more details about the performance of the method.

So far, we considered only a source positioned at $(2000, 11375, 0)$ m. This source location may not be optimal. We ran the same experiment but now with different source positions along a line in the $x$-direction. We still considered the surface-to-surface configuration. The frequency was fixed at 1 Hz and the computational grid had $128^3$ cells.

Figure 5.7 displays the effect on the absolute and relative change. Here we only show the results for three source positions, namely $(4000, 11375, 0)$ m, $(8000, 11375, 0)$ m, and $(14000, 11375, 0)$ m. The top-centre panel of Figure 5.7 suggest that the source at $x = 8000$ m provides higher sensitivity. We observe that the absolute amplitude of the difference is higher than the result with the source at $x = 4000$ m or $x = 14000$ m. However, we loose the time-lapse effect when we consider the relative change. The relative amplitudes in an area of about 2 km around the source location have become too small, as shown in the bottom-centre panel of Figure 5.7. This is caused by the fact that the near-field signals are dominated by the direct field. Repeatability errors in the strong field around the source will exceed the signal difference due to the resistivity changes in the reservoir. We obtain a better result for the source at $x = 14000$ m, where the
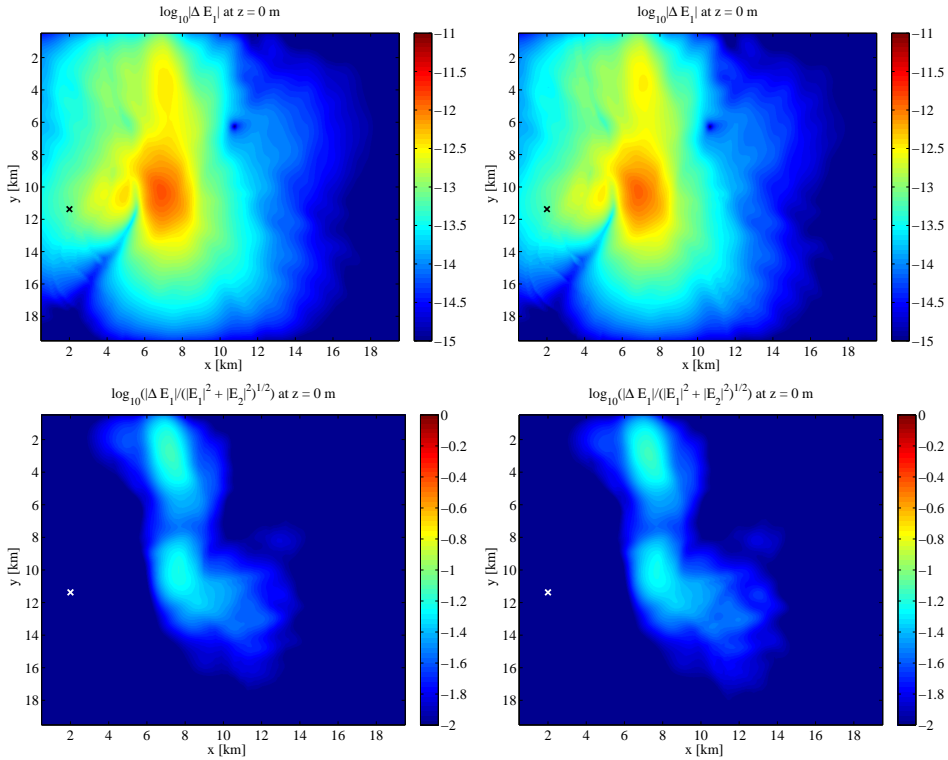
**Fig. 5.6**  The top panels display the time-lapse differences of the in-line electric field observed on the surface (top view) at 1 Hz with the computational grid of $128^3$ and $256^3$ cells, from left to right. The bottom panels display the normalized fields with amplitudes below 1% suppressed. The small cross marks the lateral location of the HED source.

time-lapse variation, both in terms of the amplitude difference as well as in relative change, is spatially better confined to the reservoir region. These results suggest that we should place the source not too close to the target area. We repeated the experiment for sources along a line in the $y$-direction. The $y$ position is now fixed at 14000 m. The top panels of Figure 5.8 display the effect on the absolute amplitude change at $x = 4000$, 8000, and 14000 m, respectively, whereas the bottom panels show the relative change.

These results confirm that there are optimal distances between source, receivers, and target area. If the source is close to the receiver and the target, the signal will be dominated by the direct field. Note that we will use the term "direct field" to denote the electric field generated in the absence of a time-lapse change. The change in reservoir properties can be considered, to first order, as a scatterer that

produces an additional signal. At large distances from the source, the signal of the time-lapse change is becoming too weak. Acquisition optimization, which we have not undertaken, should take these observations into account.

In the previous experiments, we have assumed a 100% sweep efficiency. This choice may be over-optimistic. We repeated the experiments for a sweep efficiency around 40%, assuming that not all the oil is replaced by water. The resistivity of the swept oil is now set to 10 $\Omega$m instead of 2 $\Omega$m as in the case of 100% sweep efficiency. Figure 5.9 shows a vertical slice through the model at $y = 3000$ m before and after water injection. Figure 5.10 displays the effect on the absolute and the relative change in the surface electric field for the same case as in Figure 5.8, but now with the 40% sweep efficiency applied. The difference between 100% and 40% sweep efficiency is not too dramatic in terms of the overall shape of the time-lapse difference, but the absolute and relative amplitudes become smaller, as expected.

## 5.5   MONITORING WELL

So far, we considered only the surface-to-surface configuration, placing both the sources and the receivers on the surface. This configuration is the most obvious one to use on land, but may suffer from resistivity changes in the near-surface environment, as will be considered in section 5.6. We therefore investigated another type of configuration, similar to vertical seismic profiling (VSP), namely surface-to-borehole measurements with sources on the surface and receivers in a monitoring well. We ran a number of experiments to study the feasibility of reservoir monitoring with this acquisition geometry.

In a typical vertical borehole EM survey, logging tools are usually fitted with sensors that consist of a magnetic channel and a vertical electric channel measuring $E_3$. The antenna for the horizontal electric channel will not fit. Nevertheless, we assume in our modelling study that all components can be recorded.

First, we looked for the component that is most sensitive to the reservoir change. We ran a simulation with the same configuration as in Figure 5.7. A unit dipole source in the $x$-direction was positioned on the surface at (4000, 11375, 0) m. We select this position, because the source should not be too close to and also not too far away from the target. Of course, the position may not be optimal, but it is sufficient to start the investigation. The frequency was set to 1 Hz. The bottom-left panel of Figure 5.7 shows that the strongest relative time-lapse change in $E_1$ occurs around $x = 7000$ m and $y = 3000$ m, so we placed the well at this position. The well location is marked by a circle in Figure 5.11, displaying a horizontal cross-section of the resistivity at the reservoir level with the reservoir
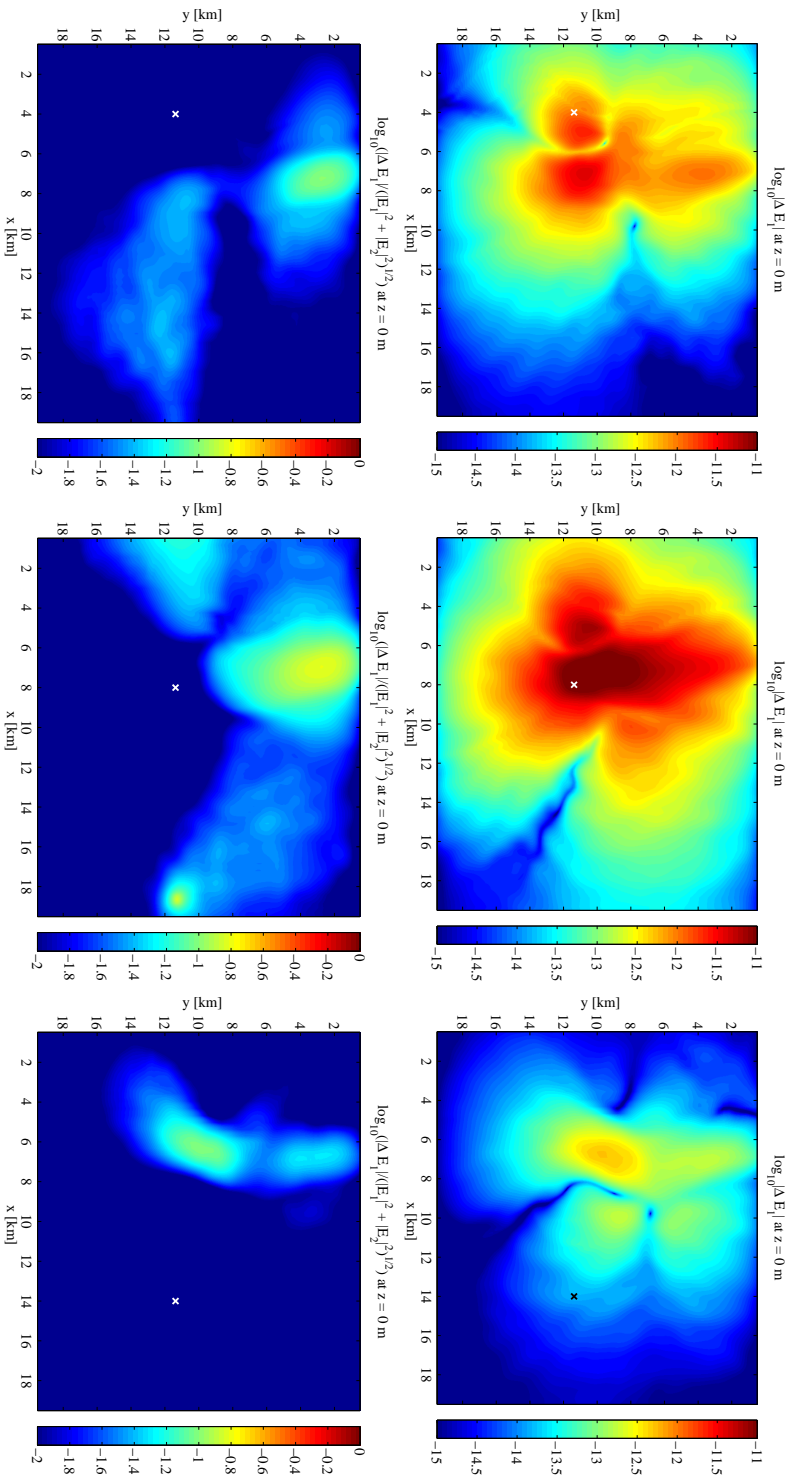
**Fig. 5.7**  The top panels show the time-lapse differences of the in-line electric field at 1 Hz, observed on the surface (top view) with source positions at $x = 4$, 8, and 14 km, from left to right. The $y$ and $z$ source coordinate is the same as in the first experiment. The bottom panels display the normalized fields with amplitudes below 1% removed. The small cross marks the lateral location of the HED source.
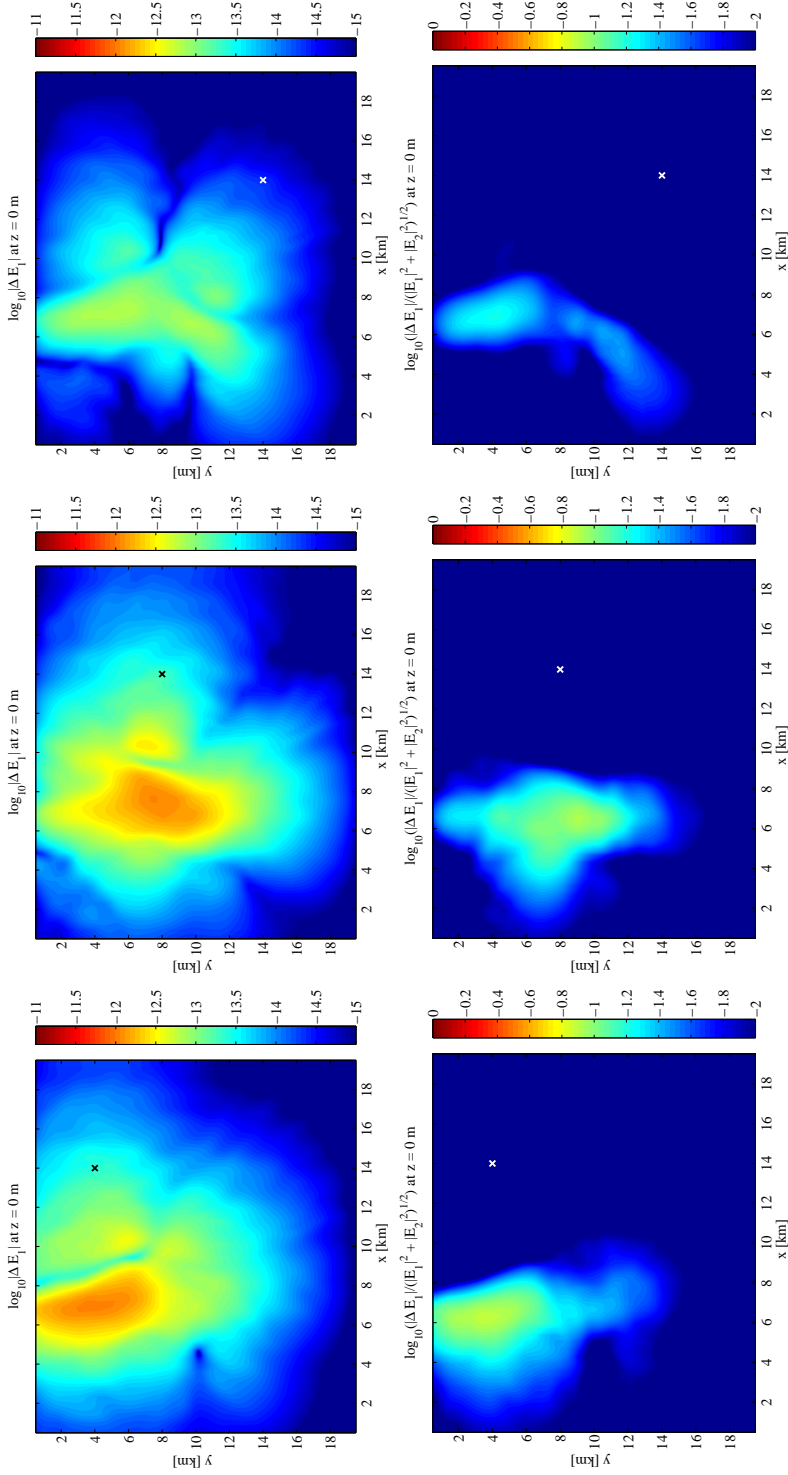
**Fig. 5.8** The top panels show the time-lapse differences of the in-line electric field observed on the surface (top view) with source positions at $y = 4$, 8, and 14 km, from left to right. The $x$-position is set to 14 km and $z$-position is at the surface. The bottom panels display the normalized fields with amplitudes below 1% suppressed. The small cross marks the lateral location of the HED source.
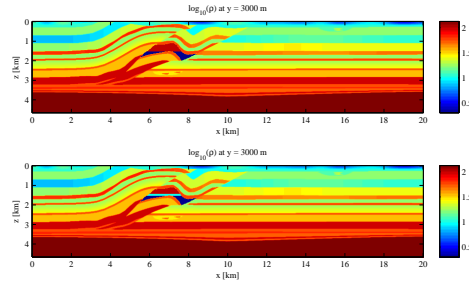
**Fig. 5.9**   The light blue part in the bottom panel shows the replaced part, having a 40%
water saturation. The top panel shows the initial condition.

clearly visible in dark blue. The black cross indicates the surface source location.

Figure 5.12 shows the response before and after water injection. The left panel
displays the resistivity log of the well. The reservoir is visible between depths from
about 1 km to 1.5 km. The dashed lines represent the initial resistivities, the
drawn lines the resistivities after production. The sweep efficiency is assumed to be
100%. The centre and the right panels of Figure 5.12 display the electric and the
magnetic field components in the well. The dashed lines represent the initial fields,
the solid lines show the fields after production. The effect of oil displacement is
visible in all electric and magnetic components and the largest changes occur close
to where the resistivity has changed. However, if we would consider a shallow
well, Figure 5.12 suggests that the vertical electric field component, $E_3$, captures
the change best. This component is relatively easily measured in a vertical well.
As in the surface-to-surface configuration, a lower sweep efficiency will generate a
smaller time-lapse change in the measured signal as can be seen in Figure 5.13,
where we assumed a sweep efficiency of 40%. Still, the effect of oil displacement
is captured best by $E_3$. A small effect also appears in $H_2$, the magnetic field
component in $y$-direction. Note that the signature of $E_3$ on the bottom-left panel
follows the resistivity log shown in the top-right panel.

Having established that measuring time-lapse changes of the vertical electric
component, $E_3$, appears to be the best option for a monitoring well, the question
remains what a good location for the well would be. To answer this question,
we examined vertical cross-sections of the time-lapse differences in the electric
field field components for different source positions. Figure 5.14 displays vertical
cross-sections of the time-lapse differences in the three electric field components
for a source in the $x$-direction at (4000, 11375, 0) m, as in Figure 5.12. We only
show a single cross-section at $y = 3$ km. The left panels display the absolute
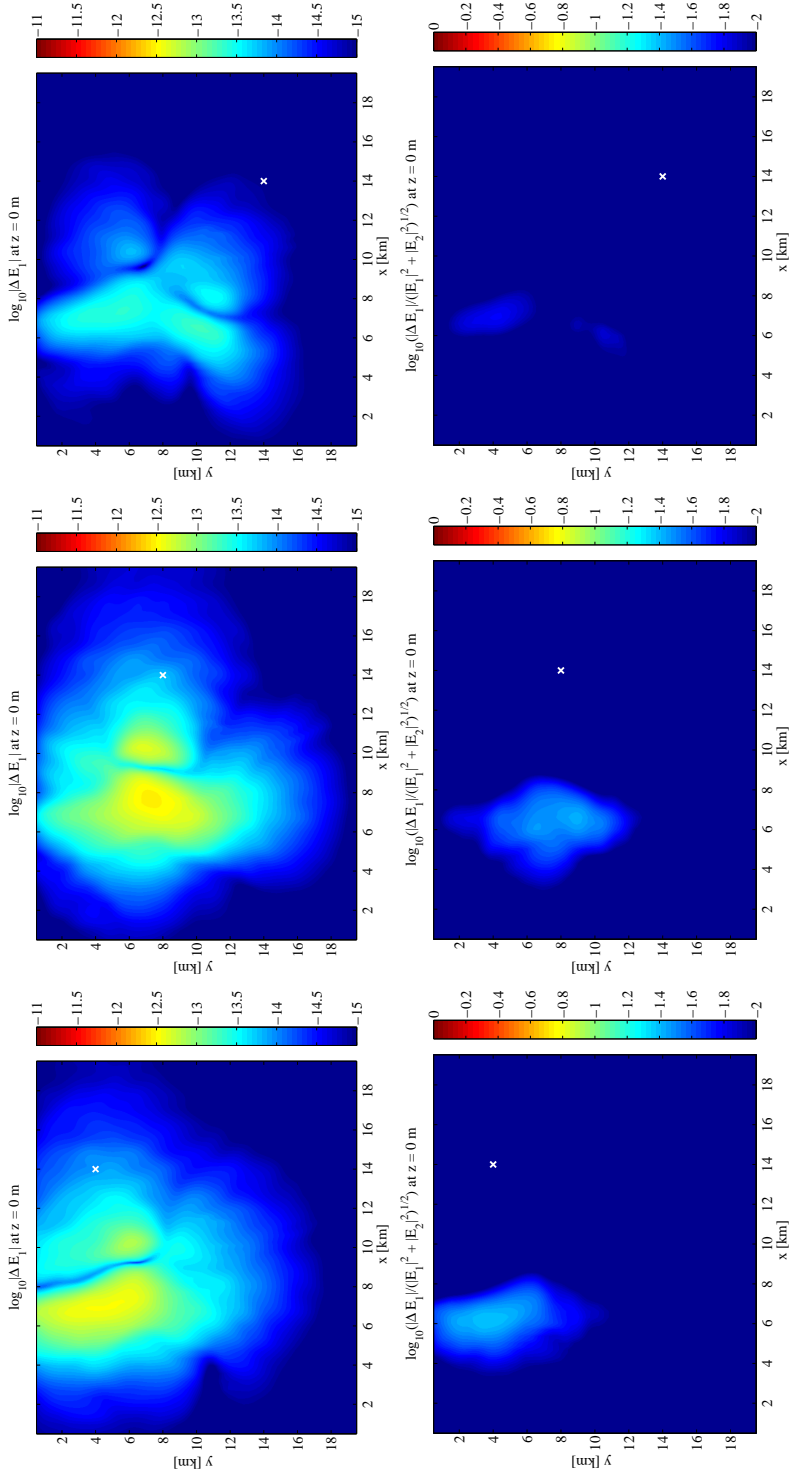difference of $E_1$, $E_2$, and $E_3$, respectively, from top to bottom. The right panels

**Fig. 5.10** Absolute (left column) and relative (right column) time-lapse changes in $E_1$ for three different source positions marked by a cross, similar to Figure 5.8, but for a sweep efficiency of 40%. The small cross marks the lateral location of the HED source.
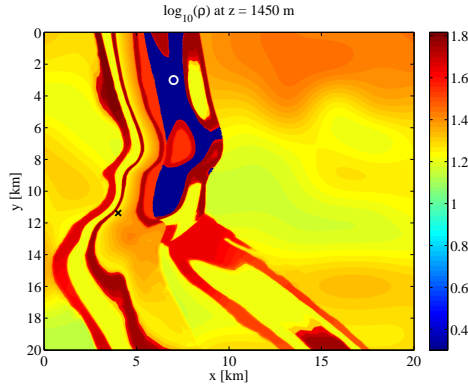
**Fig. 5.11**   A horizontal cross-section of the resistivity at reservoir depth. The black cross
marks the position of the source at $(x, y) = (4000, 11375)$ m. The white
circle indicates the location of the vertical well at $(x, y) = (7000, 3000)$ m.

show the relative differences. We observe that the largest differences in $E_1$ and
$E_3$ occur just below and above the reservoir. The differences for component
$E_1$ extend all the way to the surface. This is a useful result, as the horizontal
electric field components are easy to measure at the surface. For measurements in
a well, the vertical component, $E_3$, captures the change best, as can be seen in the
bottom-right panel of both Figures 5.12 and 5.14. We repeated the experiment
for a different source position on the surface, at (14000, 4000, 0) m, the same
position as in the left panels of Figure 5.8 at some distance from the reservoir. The
results are shown in Figure 5.15. We can see a behaviour similar to what we can
observe in Figure 5.14.

At this point, it would seem that placing a vertical well through the reservoir
appears to be a good way of capturing the change in the resistivity. With ver-
tical, piston-like displacement, this is trivially true, but then a well-log would
already be sufficient. If we want to monitor the reservoir as a whole, including
lateral heterogeneities and variability in sweep efficiency due to variations in rock
properties and faults, a single monitoring well in the reservoir may be less useful.
In the experiments shown in Figures 5.14 and 5.15, the source was placed at
some distance from the target. If, instead, we consider a source straight above
the reservoir, a monitoring well in the reservoir is less useful as illustrated by
Figure 5.16. Here, we placed the source on the surface at (7500, 8000, 0) m,
precisely above the reservoir. Figure 5.16 displays a vertical cross-section at $y =$
8 km. We can see in the panels on the right-hand side that the relative time-lapse
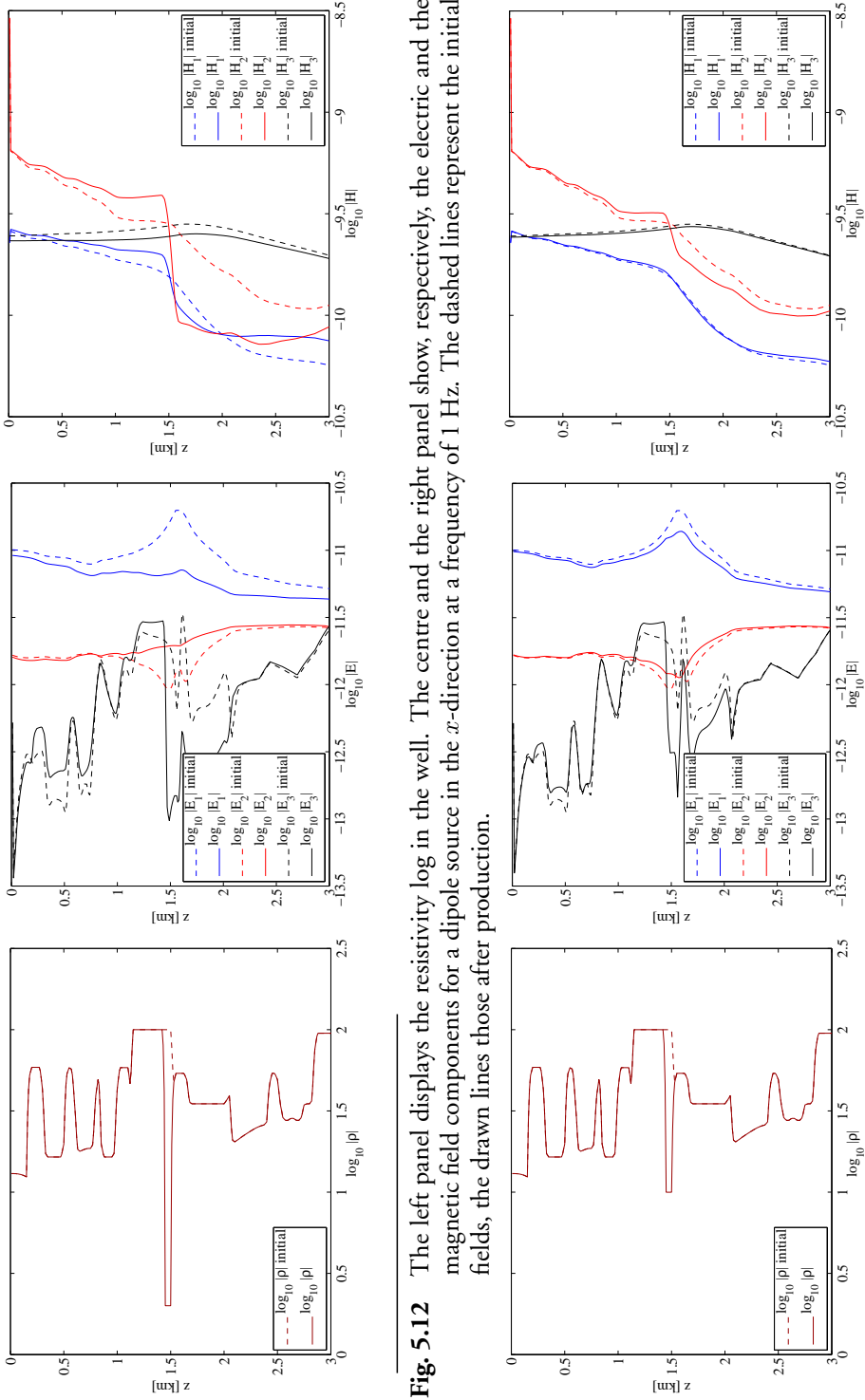differences have become much smaller. This is due to the near-field signal being

**Fig. 5.12** The left panel displays the resistivity log in the well. The centre and the right panel show, respectively, the electric and the magnetic field components for a dipole source in the $x$-direction at a frequency of 1 Hz. The dashed lines represent the initial fields, the drawn lines those after production.



**Fig. 5.13** As described in Figure 5.12, but assuming a sweep efficiency of 40%.
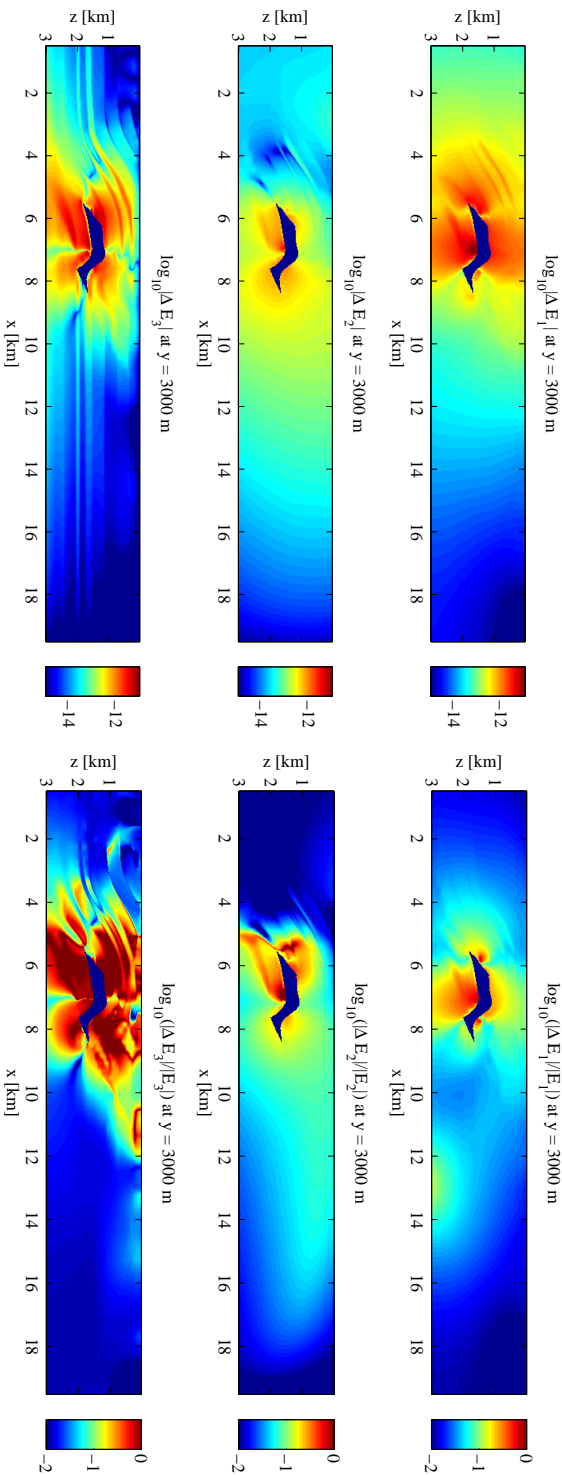
**Fig. 5.14**  All panels display a vertical cross-section at $y = 3$ km with the same configuration as in Figure 5.12. The left panels display the absolute difference of $E_1$, $E_2$, and $E_3$, respectively, from top to bottom. The right panels display the relative difference. The dark-blue area between $x = 6$ km and $x = 8$ km coincides with the reservoir. The source was placed at $(4, 11.375, 0)$ km, above the reservoir.
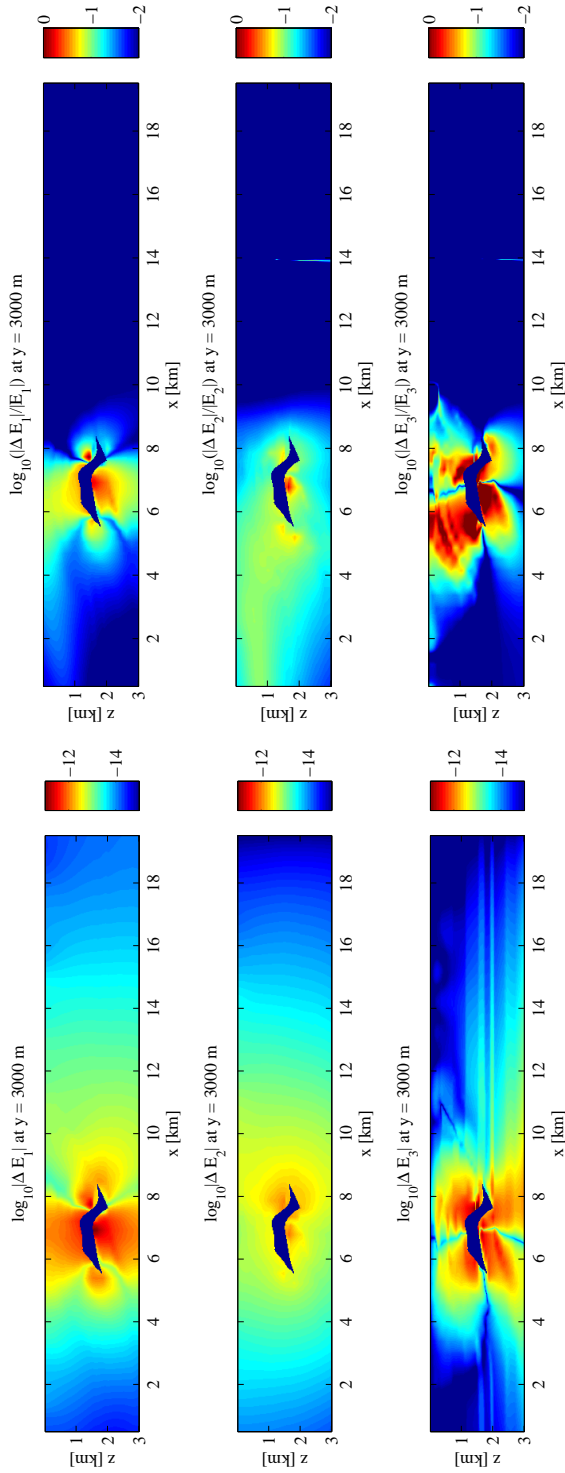
**Fig. 5.15** As described in Figure 5.14, but for a source positioned at (14, 4, 0) km, as in the left panel of Figure 5.8.

dominated by the direct field. Figure 5.16 also shows that the relative change in the vertical component becomes larger for $x$ larger than 14 km. This observation led us to consider a different type of acquisition.

Because the cost of drilling many wells is high, we want to look for an alternative, namely a walk-away survey, similar to a walk-away VSP in seismics, with a receiver in the well and sources placed at different positions on the surface. As we saw earlier that the vertical electric component was the most sensitive to changes in the reservoir, we concentrate on that component.

To avoid numerous computations for different sources at the surface, we used the source-receiver reciprocity theorem for the EM field (de Hoop, 1995), interchanging the source and receiver positions. Instead of applying source current in the $x$-direction on the surface and measuring the vertical component $E_3$ in the well, we ran the experiment with a vertical-component current source in the well and measured $E_1$ on the surface. The results should be the same. We will use both points of view in the following discussion, but assume that sources are located on the surface and the receiver in the well for the actual experiment.

To study the walk-away configuration, we first placed a receiver in the well just above the reservoir at the position (6000, 2000, 900) m and measured the vertical electric component. The white circle in the left panel of Figure 5.17 shows the well location in map view. For the source positions, we simply took the entire surface of the model. The central panel of Figure 5.17 displays the amplitude behaviour of the time-lapse difference for the vertical component, measured in the well for different source positions. We observe that the time-lapse change is spatially confined to the reservoir region, albeit with a low resolution. The strongest response appears when the source is placed close to the well. However, the picture changes completely when we consider the relative change, as shown in the right panel of Figure 5.17. The strong time-lapse signal in an area around the well location has disappeared. This effect is similar to what we found in the surface-to-surface configuration. If we take a closer look at the right panel of Figure 5.17, we observe that the larger relative differences occur at some distance from the well, as evidenced by the red to dark red colours. We conclude that the right panel of Figure 5.17 suggests a well location at some distance from the target. We repeated the experiment for a different well position at (14000, 6000, 900) m. The results are shown in Figure 5.18. We clearly obtain a better delineation of the change in the reservoir. The amplitude difference and the relative change are spatially better confined to the reservoir region.

If we use the same reasoning as for the surface-to-surface configuration, there should be an optimal distance between the well and the target area. If the source is close to the receiver and target, the signal will be dominated by the direct field.
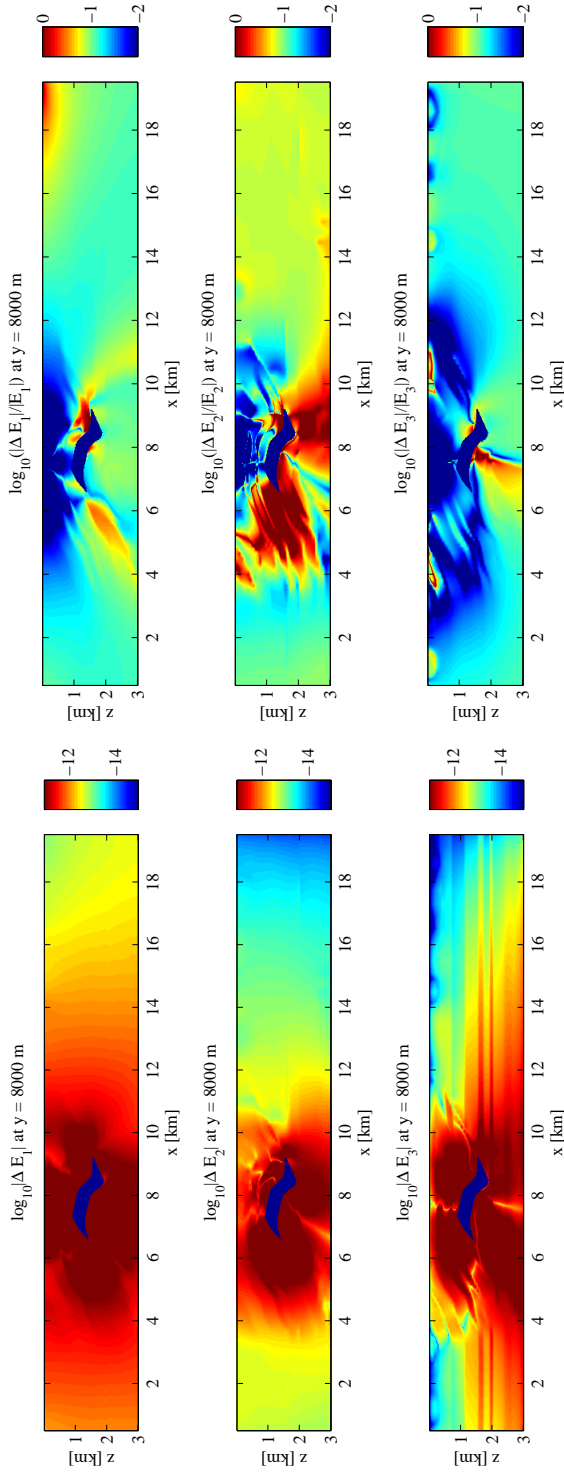
**Fig. 5.16** All panels display a vertical cross-section at $y = 8$ km of the time-lapse change in each of the three electric components for the same configuration as in Figure 5.12, but with the source above the reservoir area at $(7.5, 8, 0)$ km.
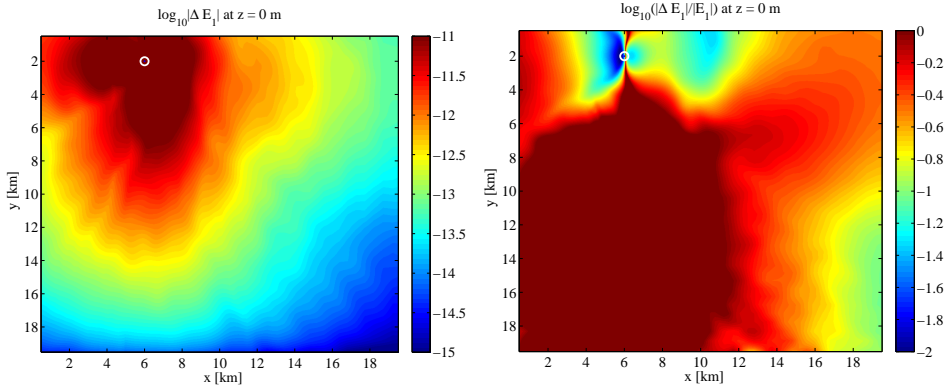
**Fig. 5.17**   The left panel shows the absolute difference of $E_1$, measured on the surface, for a dipole source in the $z$-direction at a position of $(6, 2, 0.9)$ km. The frequency was set to 1 Hz. With the reciprocity theorem, the left panel can also be interpreted as a result of placing a receiver in the well and placing a moveable source at a dense array of points on the surface. The white circle indicates the well location in map view. The right panel shows the relative absolute difference of $E_1$. Because of reciprocity, the same result will be obtained for dipole sources in the $x$-direction at the surface and a vertical antenna that measures $E_3$ in the well.
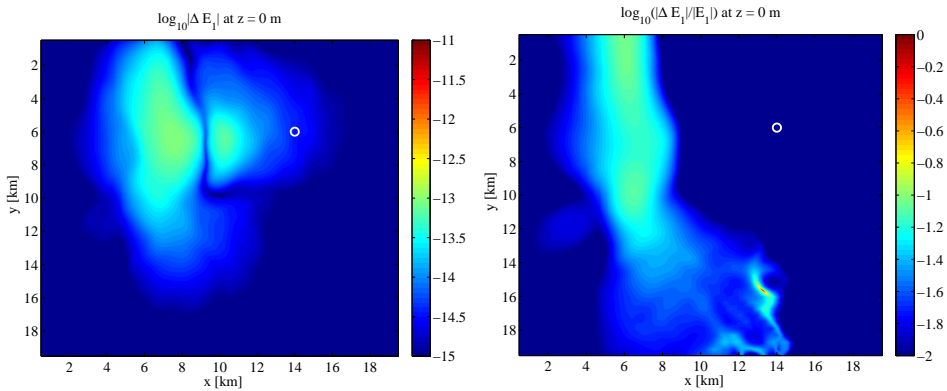


**Fig. 5.18**   As described in Figure 5.17, but with the source positioned at $(14, 6, 0.9)$ km.

If the distance is too large, the signal is becoming too weak. We conclude that the walk-away configuration has a potential value for field experiments. Once a well has been drilled, this type of measurement is relatively easy to carry out with only one or a few receivers in the well and mobile source equipment.

## 5.6  NOISE ESTIMATES

So far, we have assumed that the time-lapse difference of the electric field is mainly due to oil being displaced by water. In field surveys, the measurements will always be affected by noise and limitations of the recording equipment. Obviously, equipment and measurement errors should be made as small as possible, but are impossible to avoid. In his book, Strack (1992) lists possible sources of errors that can show up in field CSEM surveys. Some of them are caused by the choice of hardware system, other by resistivity changes in the near-surface and natural or man-made signals. In this section, we discuss the various types of "noise" that can occur in a time-lapse experiment and describe how they can be incorporated in the numerical experiments.

### 5.6.1  Near-surface effect

One type of repeatability error in a time-lapse EM data is due to changes in the near-surface environment. In time-lapse CSEM, we cannot expect the near-surface environment to be the same between surveys. Frost, for instance, will increase the resistivity of the top soil and affect the time-lapse EM measurements. Topography and near-surface inhomogeneities also play a role and can have a strong imprint on the CSEM data as shown, for example, by Li and Constable (2007) in a marine setting. Strack (1992) refers to the distortion caused by near-surface lateral discontinuities as a static shift and suggests a correction called the calibration factor. We refer to his book for more details. Here, we present an example that illustrates the effect of near-surface changes on time-lapse EM without the correction with the calibration factor. For simplicity, we only consider a resistivity change in the top soil due to, for instance, seasonal or diurnal temperature variations. Hayley *et al.* (2007) showed an empirical approximation of 1.8% to 2.2% change in bulk electrical resistivity per °C. In the context of agriculture and flood forecasting, the soil penetration of frost has been extensively studied, for example by Peck and O'Neill (1997) and DeGaetano *et al.* (2001). The frost penetration typically reaches a depth of the order of a meter. In dry areas, precipitation will have a strong effect. Without being specific about the cause of the near-surface variation, we increased the resistivity by 5% in the grid cells just below and adjacent to the surface. These cells had a cell height of 25 m.

Figure 5.19 displays the amplitude behaviour in the horizontal electric field components at 1 Hz for the same case as in Figure 5.8 but with the near-surface resistivity increase included. Here the sweep efficiency is 100%. The top panels of Figure 5.19 show the effect of near-surface changes in resistivity values on

the absolute amplitude change, whereas the bottom panels display the relative amplitude change. Although the presence of the near-surface effect produces a strong source imprint in the plots of the absolute difference, the relative changes are similar to those in Figure 5.8, where the near-surface effect was absent.

Figure 5.20 shows a vertical cross section of the absolute difference of $E_1$, $E_2$, and $E_3$ at $y = 3000$ m for the same case as in Figure 5.15 but with the near-surface resistivity increase included. Again, we can see the strong source imprint appearing in all three electric field components. These results demonstrate that the source should be put at some distance from the target. If it is too close, the repeatability error in the strong signal close to the source will mask the desired signals from the depleted area.

Near-surface changes will also cause a source imprint in walk-away surveys with a monitoring borehole, as shown in the Figure 5.21, but the effect is relatively small and localized.

### 5.6.2    Repeatability errors

The second source of distortions in time-lapse EM data is due to incorrect amplitude measurements caused by receiver mispositioning and misalignment, improper definition of gain, receiver area, current, A/D offsets, etc. We refer to these differences as repeatability errors. In land EM surveys, the impact of these adverse effects can be reduced by better instrumentation and field procedures, as suggested by Strack (1992). We assume that these differences still produce small changes in the time-lapse EM data. In the numerical experiments presented further on, we mimicked the repeatability errors by adding random numbers to the measured electric fields with a maximum amplitude of 1% relative to the signal strength at each receiver.

### 5.6.3    Measurement noise

Whereas repeatability errors tend to show up as multiplicative noise, there are various additive noise sources that also affect CSEM measurements. Examples are cultural interference, natural magnetotelluric signals, and instrument noise. Obviously, these should also be taken into account in our monitoring study.

In general, noise caused by cultural interference can be classified as periodic or sporadic noise. Periodic noise is mainly generated by man-made EM sources, such as power and telephone lines. Sporadic noise is caused by current surges in the power network, motion of magnetic material near the receivers, and so on. Although this noise in practice would pollute the wanted signals, its removal is
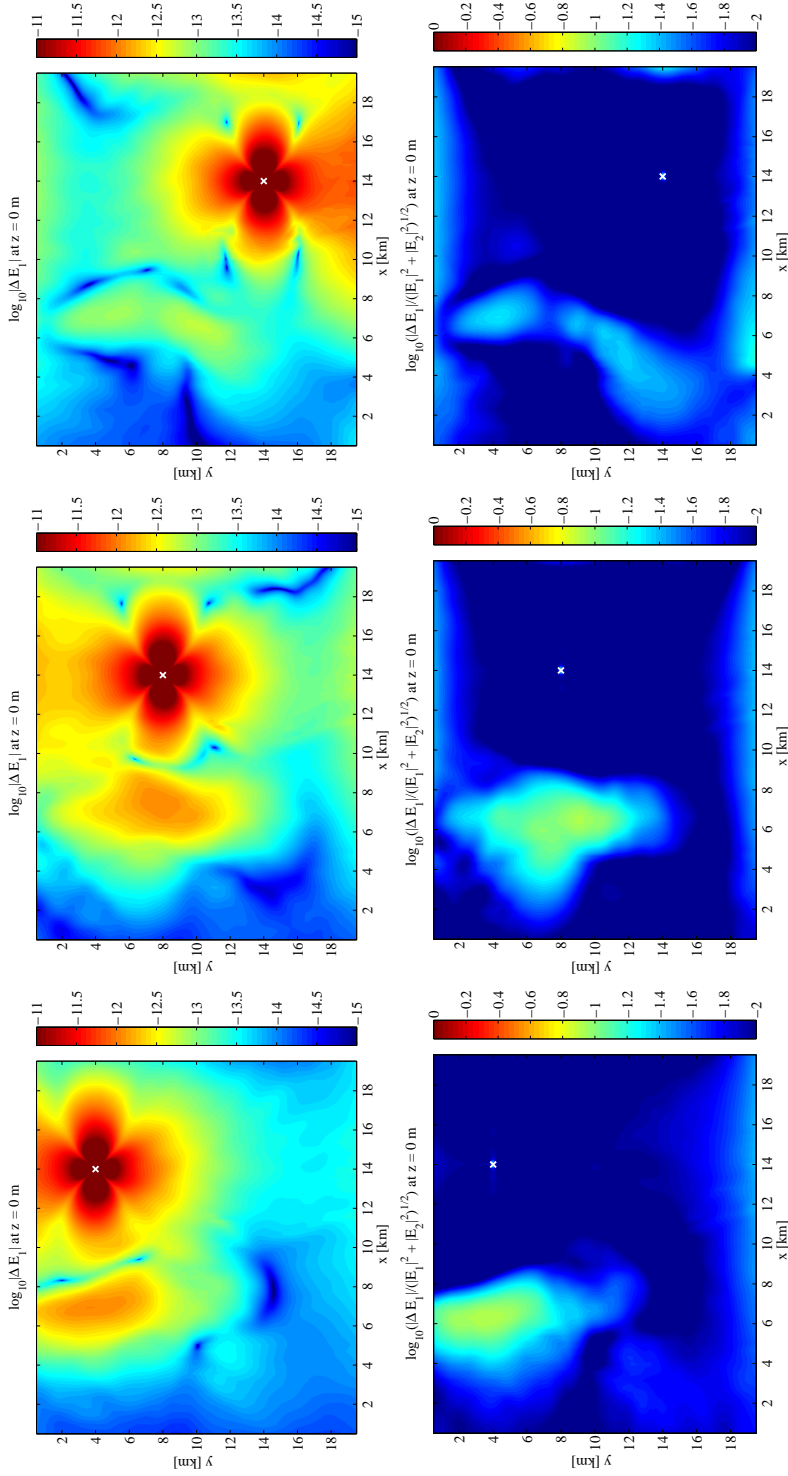
**Fig. 5.19** As described in Figure 5.8, but with the increase of the near-surface resistivity included. This increase causes large absolute differences in the time-lapse field close to the source. The small cross marks the lateral location of the HED source.
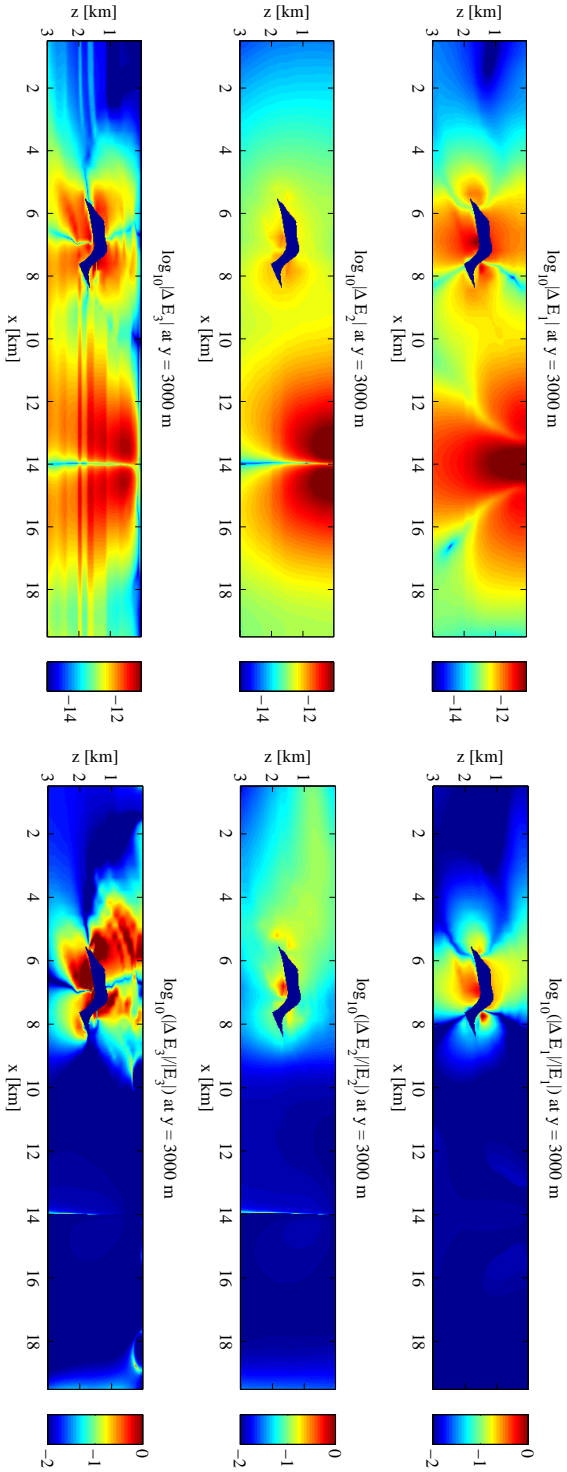
**Fig. 5.20**    As described in Figure 5.15, but with the increase of the near-surface resistivity included. Again, the effect is strongest close to the source.
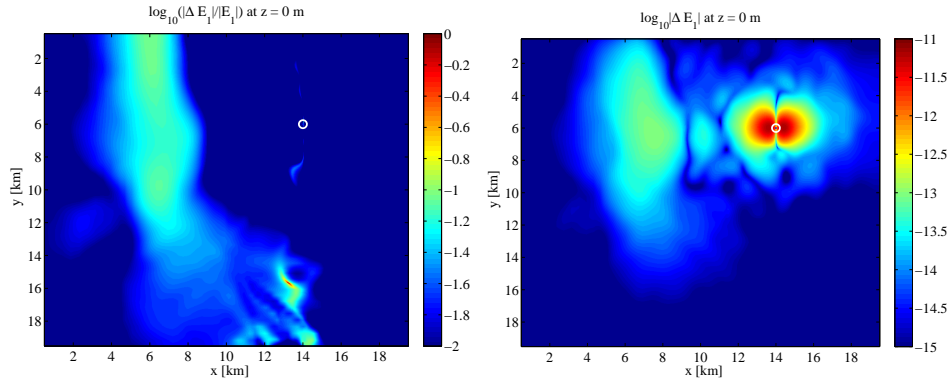
**Fig. 5.21**    As described in Figure 5.18, but for a receiver in a monitoring well and with the increase of the near-surface resistivity included.

not too difficult. Strack (1992) suggests the removal of the periodic noise with digital filters and of the sporadic noise by selective stacking techniques.

The magnetotelluric background comprises electromagnetic signals caused by natural sources as thunderstorms and interactions of the solar wind with the ionosphere and magnetosphere. Between 10 kHz and 1 Hz, the MT signals are primarily caused by thunderstorms, whereas below 1 Hz they originate from magnetosphere pulsations. There is a noise gap between 0.1 and 1 Hz. The recorded signal will definitely suffer from this type of noise, but its impact can still be reduced by careful measurements and processing. One way to overcome the natural noise is by increasing the source moment to a level where the desired time-lapse signal is large enough compared to the level of the natural background noise. Reference measurements at a distance from the reservoir can also help to reduce the impact of magnetotelluric interference.

A recording instrument has a certain noise floor and a limited dynamic range. Typical values for marine applications can be found in papers by, for instance, Webb *et al.* (1985) and Flosadóttir and Constable (1996). The noise level depends on the frequency and the antenna length. For land applications, the noise floor of the sensor can be a bit higher than the one for marine sensors. Pedersen (1988), for instance, mentions a noise floor density for the sensor of about $5 \times 10^{-9}$ V/(m$\sqrt{\text{Hz}}$) at 1 Hz. For the electric field, this amounts to $5 \times 10^{-9}$ V/m if the measurements were carried out during one second. Here we divided the spectral noise density by the square root of the measurement duration. Although instrumentation has improved over the last twenty years, we nevertheless adopt Pedersen's estimate, the noise floor is quite high compared to the size of the

time-lapse differences shown in Figure 5.4. One way to overcome the noise is by increasing the source moment, as is also done for reducing the effect of MT signals. In the numerical experiments, we chose a noise amplitude of $10^{-11}$ V/m. This is relatively low compared to the Pedersen's value. To have the same behaviour using the Pedersen's value, that would require the source moment approximately 100 times larger than the current source moment. Note that we assumed that cultural noise and natural MT background can be removed by pre-processing of the data.

### 5.6.4   Incorporating noise into the modelling

We added the effect of various sources of noise, except the near-surface effect, to the numerical modelling results in the following way.

1. We first calculate the electric field for the configuration that represents the resistivity model before production. We assumed a 20 A current source, as typical in land EM experiments. In the earlier experiments, we considered only the unit source.

2. At each receiver, we then generate a random number with a maximum amplitude of $10^{-11}$ V/m and add this to the recorded field.

3. We include the repeatability error by adding a random number with a maximum amplitude of 1% relative to signal strength at each receiver.

4. We repeat the above three steps for the configuration that represents the resistivity model after production.

5. We include a 6-decade dynamic range of the recording by suppressing data outside the range of $10^{-13}$ V/m to $10^{-7}$ V/m.

Figure 5.22 displays the difference in absolute amplitudes of the electric field component $E_1$ for various source positions. Here we applied 100% sweep efficiency as used in Figure 5.8. Although the noise dominates the signal, we can still observe the changes in resistivity above the reservoir.

If we take a closer look at Figure 5.22, we observe that different parts of the reservoir are illuminated for different source positions. This suggests stacking of the EM data for different source positions to recover the shape of the reservoir. Figure 5.23 shows the average after stacking data from the four source locations displayed in Figure 5.22. Although the source imprint remains, the shape of the reservoir is better defined.
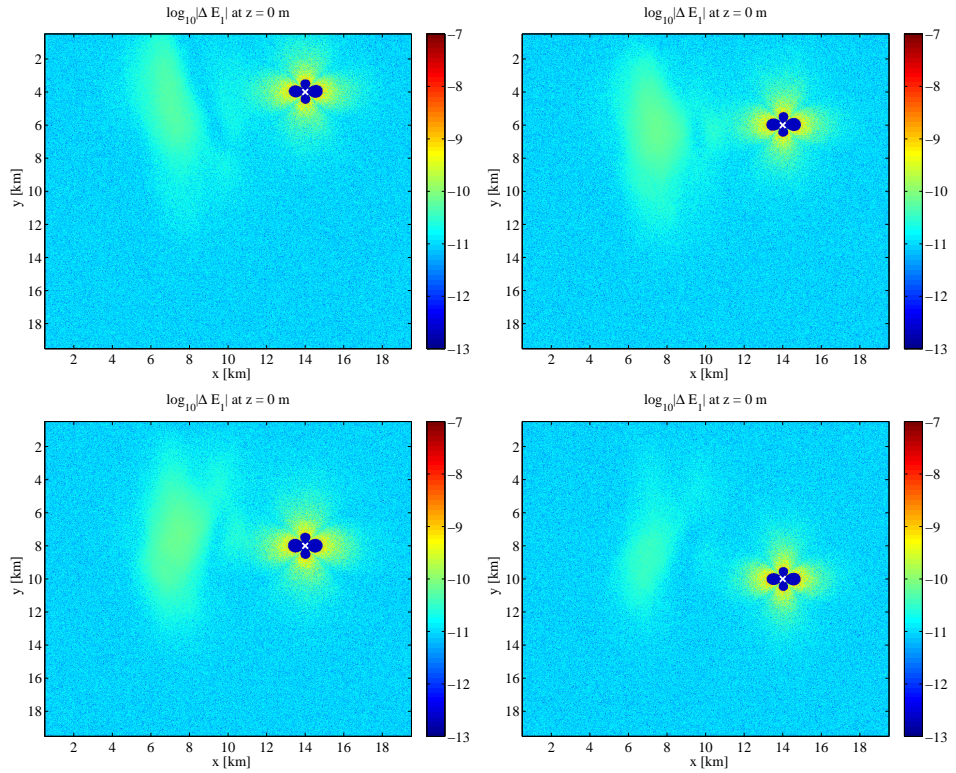
**Fig. 5.22** The time-lapse difference of the electric-field component $E_1$ with added noise at 1 Hz, recorded on the surface (top view) for a surface source with an $x$-position of 14 km and with $y = 4$, 6, 8, or 10 km, shown top-left, top-right, bottom-left, and bottom-right, respectively. The blue four-leaf clover pattern is the result of clipping the data to the dynamic range.

## 5.7  CONCLUSIONS

We have studied the effect of resistivity changes due to oil production on land CSEM measurements for a complex geological model. We considered a surface-to-surface acquisition geometry as well as a surface-to-borehole configuration with a vertical monitoring well. The results show that the resistivity change due to displacing oil by brine can produce a small but measurable change in the CSEM response. How well the time-lapse change is confined to the area above the resistivity change, depends on the placement of the sources and receivers. The results suggest that there are optimal distances between sources, receivers, and the target area. If the source is close to the receiver and the target, the signal will be dominated by direct field and the time-lapse signal will be masked. If the
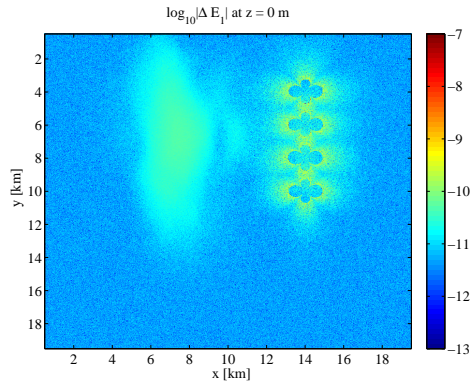
**Fig. 5.23**  Average time-lapse change in $E_1$ after stacking data for 4 different source
positions. Sources were located on the surface with an $x$-position of 14 km
and with $y = 4, 6, 8,$ and 10 km.

distance is too large, the time-lapse signal will become too weak to be detected.
This implies that the acquisition can be optimized for a given target configuration.

An alternative acquisition geometry consists of a single vertical monitoring
well and sources at various surface positions.  Our results for this walk-away
setting suggest that the technique can be an attractive choice if the vertical electric
component is measured in the well.  Our study suggest that for the land example
considered here, the detection of time-lapse changes due to production by time-
lapse EM measurements will require a repeatability error of 1% or less, as well as
proper removal of interfering coherent signals.

# 6 The effect of the airwave

**S U M M A R Y**

The displacement of oil with saline water creates a resistivity change that might be detectable by time-lapse CSEM measurements. Because the difference in measured EM signals before and after production is small, acquisition design plays an important role. We carried out numerical experiments to understand how to optimize the acquisition to best capture the time-lapse signal. Our study shows that exciting a VED source at some distance away from the target would be an attractive choice, as a HED source induces strong airwave energy masking the anomalous signal.

## 6.1   INTRODUCTION

Over the last decade, the CSEM method has established its position as a tool for detecting and evaluating hydrocarbon reservoirs (Constable and Srnka, 2007). The method is mainly applied for derisking potential prospects, complementary to seismics. Another potential application is hydrocarbon reservoir monitoring during production. Water flooding or steam injection for oil production creates a resistivity change that may be detectable by time-lapse EM measurements. The main question is whether or not such a change is detectable and if EM can do better than time-lapse seismics. The latter requires a porosity greater than 30% to have a significant velocity difference between a water- and hydrocarbon-bearing reservoir. With EM, the resistivity difference between rock containing hydrocarbons or saline water can be two or three orders of magnitude, making CSEM method potentially more suitable if this difference can be detected in the presence of repeatability errors and noise.

Several authors have investigated the feasibility of CSEM monitoring Black and Zhdanov (2009); Lien and Mannseth (2008); Orange *et al.* (2009); Wirianto *et al.* (2010a). The first and second groups employed a 3D integral-equation method to model the time-lapse effect due to the flooding front during water injection into an oil reservoir, whereas Orange *et al.* (2009) used an accurate 2D finite-element modeling code to study several scenarios for reservoir depletion, including lateral and bottom flooding, stacked reservoirs, and partial depletion. Wirianto *et al.* (2010a) used a 3D multigrid modeling code of Mulder (2006) to study the effect of vertically piston-like reservoir depletion in a land setting. To indicate the time-lapse resistivity changes, the authors frequently used both the time-lapse difference as well as the ratio of the recorded EM data before and after production, when part of the oil has been replaced by saline water. In some cases, the data comparison provided direct geometrical information about the depleted zone, whereas in others, more advanced data processing was required. However, the comparison of data recorded at the receivers offers little insight in how the EM fields interact with the depleted zone before and after production. Consequently, a direct interpretation remains difficult even if the time-lapse signals show up clearly.

Here, we present a modeling exercise investigating the interaction between excited low-frequency EM signals and the depleted zone in more detail. We use 2D vector plots of the current density generated by a harmonic electric dipole source in a simple half-space background. The patterns of current distributions are analyzed for two models that represent the resistivity before and after oil production with a water drive. We consider two sources: a surface horizontal
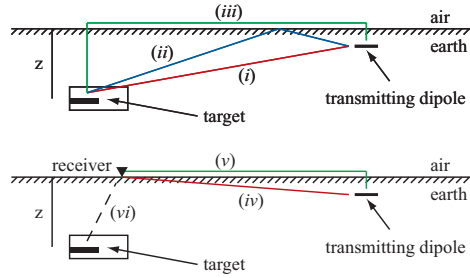
**Fig. 6.1**     On the top, paths of the EM fields at the depleted zone (target) from a HED
              source, consisting of the direct field *(i)*, the reflected field *(ii)*, and the airwave
              *(iii)*. On the bottom, paths of EM fields at receivers, consisting of the direct
              field *(iv)*, the direct airwave *(v)* and the time-lapse field *(vi)*.

electric dipole (HED) source and a vertical electric dipole (VED) source in a well.
Understanding how the EM fields interact with the depleted zone can help us to
optimize acquisition design.

We first review the basic concept of the CSEM method in the context of the
monitoring problem, then present the numerical experiments, and finally discuss
our findings.

## 6.2    PRIMARY-SECONDARY FORMULATION

To illustrate the concept of the CSEM method for reservoir monitoring, we begin
with a simple survey layout. A typical field deployment with a horizontal electric
dipole (HED) is sketched in Figure 6.1. During a survey, a source is employed to
excite electro-magnetic fields that penetrate through the background medium and
illuminate the target, in our case the depleted zone (the top panel of Figure 6.1).
EM receivers are placed on the surface, typically measuring the horizontal electric
currents and the three components of the magnetic field. The interaction between
the excited low-frequency EM signals and the conductive target zone then results
in a secondary field that can be detected with receivers on the surface in addition
to the response of the background field (the bottom panel of Figure 6.1). The
response of the background field is the EM response that would be excited by the
same source in the absence of the target body. The presence of a target body is
usually analyzed by comparing the EM response of the target to the response for
the background without the target.

The concept of the CSEM method for the monitoring problem is the same
as for the exploration problem, but with a different target body and background

fields. For exploration, the target body is the resistive hydrocarbon-bearing reservoir and the background field is the response for a background medium without the reservoir. For monitoring, the target body is the depleted zone and the background field is the response for the initial configuration, before oil production started. Although the concepts are similar, the analysis for the monitoring problem differs from that for the exploration case. For exploration, the analysis is frequently done by comparing the EM response of a hydrocarbon-bearing reservoir to the response for a layered, 1D background without the reservoir. The layered background model is used for computational speed and lateral variations are usually accommodated for by locally gluing 1D models together. Because the hydrocarbon reservoir is more resistive than the surrounding background, its presence causes the electromagnetic field to be reflected. It then diffuses back to the receivers at the sea bottom or, in our case, on the land surface, where it can be detected as an anomalous signal. In contrast to data analysis for the exploration problem, the analysis for the monitoring problem usually involves the EM responses for two different states with oil present in both. After production, there still may be oil on top of the water-flooded area. The existence of this highly resistive body may prevent the depleted zone from being "illuminated" by the source and therefore the time-lapse difference in the EM signal may be too weak to be reliably measured. In that case, acquisition design will play an important role in capturing the time-lapse variations. In the next section, we consider some numerical experiments to investigate the acquisition design that captures the time-lapse signal best, considering two types of setups, namely a surface-to-surface and a borehole-to-surface configuration.

## 6.3   NUMERICAL EXPERIMENTS

Before considering a monitoring example, we start with a simple half-space configuration. Figure 6.2 shows vector plots of the current density for an $x$-directed point source (HED) in a vertical section of a homogeneous Earth model with a resistivity of 2 $\Omega$m. The source is located at (10,0,0) km, just below the air-earth interface, and operates at 1 Hz. The images illustrate the background current-density distribution. The color shows the magnitude of current density, overlaid by the black arrows that point in the direction of current-density vectors. The left panel shows the real part of current density, the right its imaginary part. In both panels, we see that the current-density distribution excited by a 1 Hz HED source rapidly decays away from the source. This clearly shows the diffusive character of EM fields generated by a low-frequency source. At shallow depth, both the real and imaginary part of the current density are decaying less
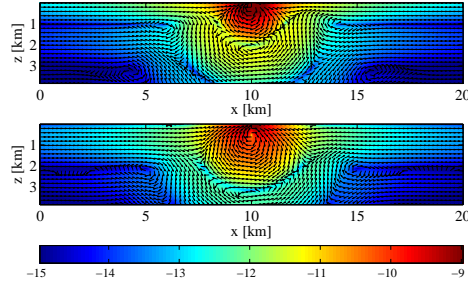
**Fig. 6.2** Current-density vector plots for a 2 $\Omega$m half-space model. All panels show the $x, z$-plane at $y = 0$ km. A harmonic $x$-directed point dipole source (HED) is located at $(10,0,0)$ km. The source frequency is set to 1 Hz. The background color represents the amplitude of the current density on a logarithmic scale and the black arrows mark the directions of the current-density vectors. The top panel displays the real part of current density, whereas the bottom panel shows its imaginary part.

in the lateral direction. This fact is due to the so-called airwave, which is the electromagnetic field that propagates in the air with the speed of light. The part that propagates along the surface is called a lateral wave and it sends an electromagnetic field into the ground with an almost vertical diffusion direction (Baños, 1966; King *et al.*, 1992). A similar effect can be observed for a source at the interface between two conducting layers, where the fast diffusive medium (low conductivity) generates a field in the slow diffusive medium (high conductivity) that diffuses in the direction normal to the interface. The last case bears some resemblance to the refraction of seismic waves, where waves in the fast medium send energy back into the slow medium at the critical angle. A different pattern for the current-density distribution is obtained with a VED source, as shown in Figure 6.3. Here, we repeated the experiment but now with a $z$-directed point dipole source located at $(10,0,0.5)$ km. Unlike in the case of the HED source, the lateral wave is absent and the EM signals comprise only the direct field and the reflected fields due to the air-earth interface, which acts as a perfect reflector (Baños, 1966; King *et al.*, 1992). If $\mathbf{E}^d$ denotes the direct EM field and $\mathbf{E}^{aw}$ the field related to the airwave, the HED source generates a field $\mathbf{E}^d + \mathbf{E}^{aw}$, whereas with a VED source only produces $\mathbf{E}^d$.

Next, we include a reservoir under production. We take the same half-space model as before and insert a 300 m thick resistive hydrocarbon-bearing layer at 1 km depth with a resistivity of 100 $\Omega$m and a 200 m thick conductive water-bearing layer with a resistivity of 3 $\Omega$m. The sketch of the reservoir is shown in Figure 6.4. For the monitoring study, we assume the reservoir is flooded by saline
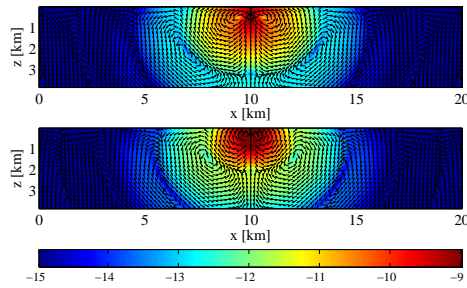
**Fig. 6.3**   As described in Figure 6.2, but now for a $z$-directed point dipole source (VED), located at (10,0,0.5) km.
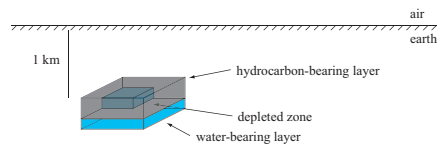


**Fig. 6.4**   The reservoir has a dimension of 2 km by 2 km by 0.5 km, divided into two parts for oil-bearing reservoir and water-bearing reservoir. Before production, oil layer are assumed perfectly on top of water layer. During production, a part of oil layer is replaced by saline water creating a depleted zone in the top-left corner.

water from the top left, creating a small, 100-m thick, box-shaped depleted zone in the corner of the hydrocarbon-bearing layer.

The first experiment is with surface-to-surface configuration, placing a HED source on the surface and measuring the response with receivers also on the surface. The bottom-left panel of Figure 6.5 displays the amplitude behavior of time-lapse difference for the in-line electric field measured on the surface, excited by a HED point source located at (11,9.5,0) km and operating at 1 Hz, as before. In this case, we assume the difference is entirely due to the resistivity change in the reservoir.

Clearly, the result of the time-lapse difference is laterally confined to the location of resistivity change. However, if we compare the amplitude of time-lapse difference to its signal strength as shown in the top panel of Figure 6.5, we observe that the time-lapse signal is much weaker, below 1% of the signal strength. Consequently, the time-lapse difference may suffer from the multiplicative noise that would easily happen as a result of repeatability errors in the measurements. Frost, for instance, will increase the resistivity of the top soil and affect the time-lapse EM measurements. To illustrate the effect of this type of noise, we added a random number with a maximum amplitude of 1% relative to signal strength at each

receiver, shown in the bottom-right panel of Figure 6.5. Here, we observed that the noise due the repeatability error dominates the time-lapse signal and imposes a strong source-imprint.

The multiplicative noise caused by repeatability errors can be described as follows. With time-lapse measurements, we collect two datasets, before and after production. The one obtained after production can be expressed as $\mathbf{E}^d + \mathbf{E}^{aw} + \mathbf{E}^{d;sc} + \mathbf{E}^{aw;sc}$. The first two terms denote the incident fields, consisting of a direct field and one due to the airwave. The last two scattering terms describe the time-lapse change. If we assume the time-lapse change is entirely due to the resistivity change in the reservoir, the component $\mathbf{E}^d + \mathbf{E}^{aw}$ will completely cancel out when considering the time-lapse difference. In the presence of multiplicative noise, however, the time-lapse difference will become $\alpha(\mathbf{E}^d + \mathbf{E}^{aw}) + \mathbf{E}^{d;sc} + \mathbf{E}^{aw;sc}$, where the factor $\alpha$ models the repeatability errors. The noise becomes a problem if $|\mathbf{E}^{d;sc} + \mathbf{E}^{aw;sc}|$ is much smaller than $|\alpha(\mathbf{E}^d + \mathbf{E}^{aw})|$, as happens in Figure 6.5. In that case, the airwave, $\mathbf{E}^{aw}$, appears as the predominant signal.

Let us assume the time-lapse difference is entirely due the resistivity changes in the reservoir, so that it can be written as $\mathbf{E}^{d;sc} + \mathbf{E}^{aw;sc}$. We want to determine which of the two incident fields, $\mathbf{E}^d$ or $\mathbf{E}^{aw}$, most affects the time-lapse signal. To reduce the contribution of the direct field, we placed the source further away from the target, whereas to reduce the contribution of the airwave, we repeated the experiment in a fully homogeneous background, without an air-earth interface. Figure 6.6 shows the results. The top panel displays the time-lapse difference when we have the contributions of both the direct field and the airwave. The bottom-left panel shows the time-lapse difference when we have only the airwave contribution and the bottom-right with only the direct field. Clearly, the time-lapse signal due to the incident field generated by the airwave provides the best result. We also observe that the time-lapse difference measured on the surface is laterally confined to the location of resistivity changes in that case. Therefore, the presence of the airwave is beneficial, because it illuminates the depleted zone even if the source is not close to the target. In the presence of repeatability errors, however, the strong currents induced by the incident airwave cannot be fully subtracted and the multiplicative noise will start to dominate the time-lapse signals, making them difficult to detect.

As an alternative, we considered a vertical dipole source located in a well. The left panel of Figure 6.7 displays the amplitude behavior of time-lapse differences for the in-line electric field measured on the surface, excited by a VED point source located at (11,9.5,0.5) km and operating at 1 Hz, as before. The right panel of Figure 6.7 displays the same response, but after adding random noise with a maximum amplitude of 1% relative to the signal strength at each receiver.
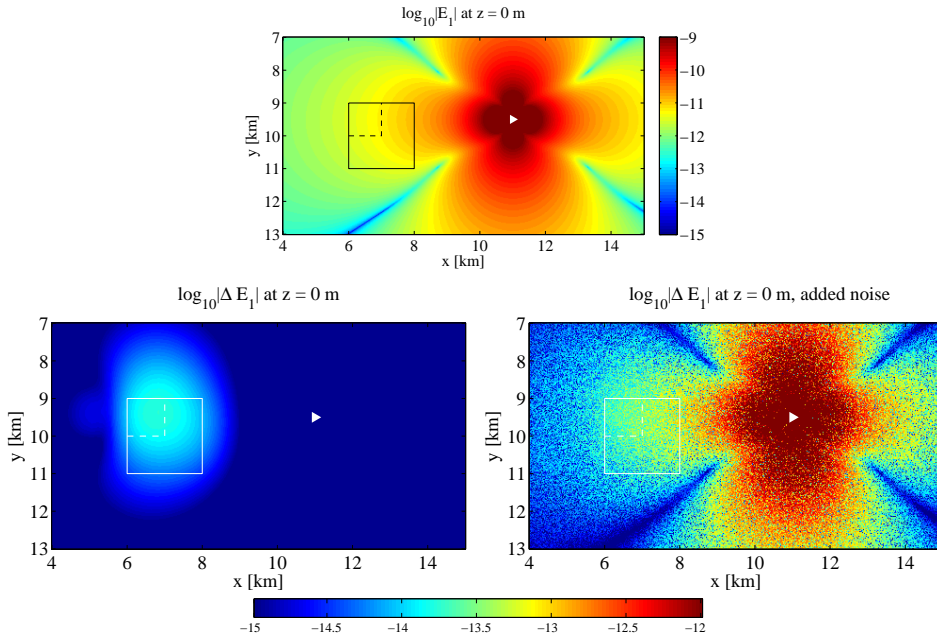
**Fig. 6.5**  The top panel displays the $x$-directed electric field observed on the surface (top view), computed for the configuration that represents the resistivity before production. The bottom-left panel displays the time-lapse difference of the $x$-directed electric field observed on the surface (top view). The bottom-right panel displays the time-lapse difference with added noise. The solid white box indicates the lateral position of the reservoir and the dashed white line indicates the lateral position of the oil-water interface after flooding. The small white triangle marks the lateral location of the HED source.

The time-lapse differences can still be recognized, although not easily.

## 6.4   CONCLUSIONS

With the HED source, the airwave appears as the predominant signal. It propagates in the air and the part that propagates parallel to the surface has a geometrical spreading function inversely proportional to distance cubed. This part generates a diffusive electromagnetic field that diffuses almost vertically down into the Earth. The presence of the airwave can be beneficial for the monitoring problem, because it provides illumination of the depleted zone even if the source is not close to the target. However, at the same time, the strong currents induced by the airwave on the ground also dominate the time-lapse signals. In the presence of repeatability errors, this will make it difficult to recognize the signals due to time lapse changes
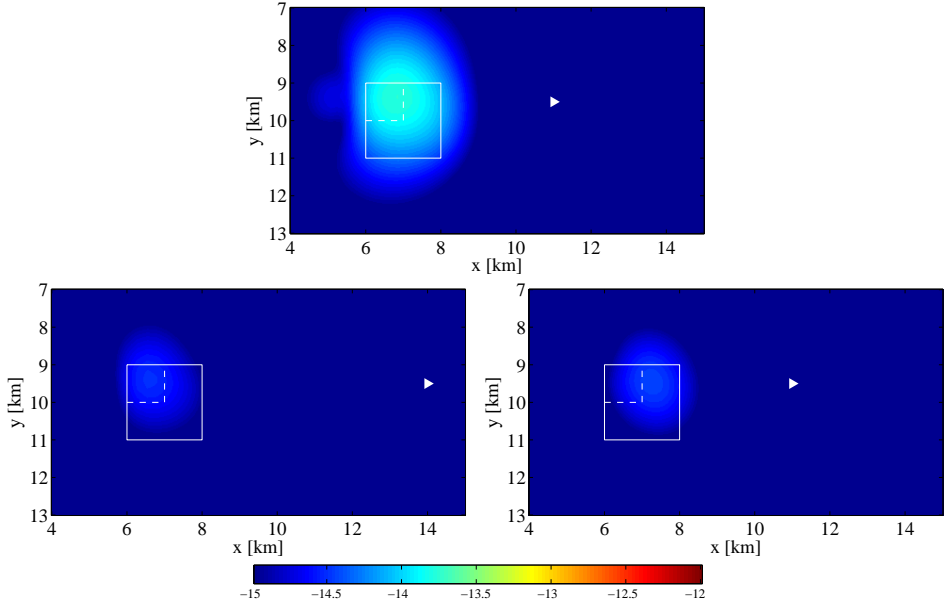
**Fig. 6.6**    All panels show $\log_{10}|\Delta E_1|$ at $z = 0$ km (top view). The top panel displays the amplitude behavior of time-lapse difference when the resistivity change is illuminated by the direct field and the airwave. The bottom-left panel corresponds to illumination by only the airwave, and the bottom-right panel by only the direct field.
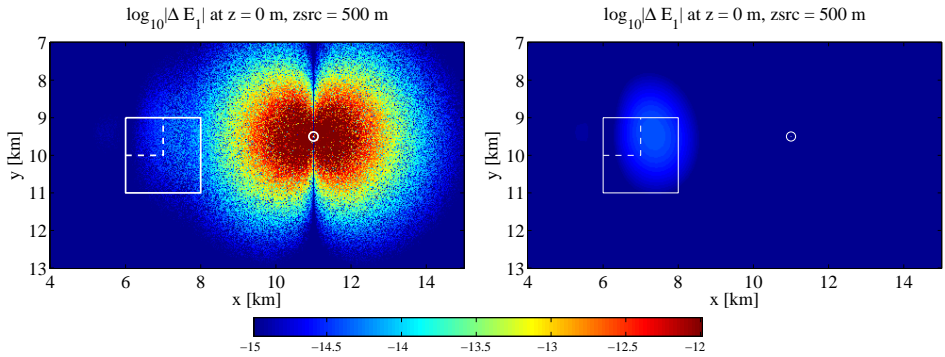


**Fig. 6.7**    The left panel displays the time-lapse differences of the electric component $E_1$ observed on the surface (top view). The right panel displays the time-lapse difference of the electric component $E_1$ with added noise.

in the presence of repeatability errors. However, a HED source could still be useful if the airwave can be eliminated or at least be reduced. Otherwise, placing

the source in a vertical well is the preferred option, in spite of the higher cost.

# 7 Exploiting the airwave for time-lapse reservoir monitoring with CSEM on land

**SUMMARY**

In the application of controlled source electromagnetics for reservoir monitoring on land, repeatability errors in the source will mask the time-lapse signal due to hydrocarbon production when recording surface data. We demonstrate that at larger distances, the airwave will still provide sufficient illumination of the target. The primary airwave diffuses downward into the Earth and then is scattered back to the surface. The time-lapse difference of its recorded signal reveals the outline on the surface of the resistivity changes in a hydrocarbon reservoir under production. However, repeatability errors in the primary airwave can destroy the signal-to-noise ratio of the time-lapse data. We present a simple and effective method to remove the primary airwave from the data, which we call 'partial airwave removal'. For a homogeneous half space and a delta-function type of source, the surface expression of the airwave does not depend on frequency. For this reason, the primary airwave can be subtracted from the data using recordings at two frequencies, one low enough with a skin depth of the order of the reservoir depth that is sensitive to the reservoir at depth, the other high enough to only sense the near surface. The method does not affect secondary airwave components created by signals that have propagated through the Earth and returned to the surface. We show that the method provides a direct indicator of production-related time-lapse changes in the reservoir. We illustrate this for several models, including a general 3D heterogeneous model and one with strong surface topography, for situations where survey repeatability errors are large.

## 7.1   INTRODUCTION

During the last decade, controlled source electromagnetics (CSEM) has been a subject of continued interest in the oil and gas industry. Early enthusiasm was triggered by the success of a pilot CSEM experiment for detecting thin resistive hydrocarbon reservoirs located off-shore Angola (Ellingsrud *et al.*, 2002). Since then, several authors reported and established its position as a tool for de-risking potential hydrocarbon prospects next to seismics; see, for example, the March–April 2007 issue of Geophysics, the March 2007 issue of The Leading Edge, and the May 2009 and May 2010 issues of First Break. Another potential application of CSEM is hydrocarbon reservoir monitoring during production. Water flooding or steam injection for oil production creates resistivity changes in the reservoir, and those changes potentially can be detected with time-lapse CSEM measurements. Several feasibility studies on time-lapse CSEM (Lien and Mannseth, 2008; Orange *et al.*, 2009; Wirianto *et al.*, 2009, 2010a; MacGregor and Cooper, 2010) led to optimistic conclusions. Earlier, Wright *et al.* (2002) obtained positive results with field data when monitoring gas storage in a shallow, 25-m thick reservoir containing gas and water.

In our own synthetic feasibility study (Wirianto *et al.*, 2010a), we considered land CSEM for a deeper target with oil and brine in a complex 3D resistivity model. We studied the effect of additive and multiplicative noise and repeatability errors on the time-lapse EM signal. Close to the source, multiplicative repeatability errors of the direct field completely drown the time-lapse measurements. Further away, surface time-lapse data revealed the outlines of the subsurface resistivity changes, assuming oil depletion of a rather large reservoir volume. With a smaller depleted volume, the production-related time-lapse signal becomes harder to distinguish, especially in the presence of repeatability errors (Wirianto *et al.*, 2010b).

This led to two questions: why can we still observe time-lapse signals at a larger distance from the source, and how can we improve their signal-to-noise ratio (SNR)? In the following section, we explain that the primary airwave provides the answer to the first question. It is the dominant signal at the surface, and, when diffused into the Earth, the main source of illumination for the reservoir. However, repeatability errors will affect the primary airwave, just as happens with the direct field, and these can mask the time-lapse signal from the swept reservoir region. To improve its SNR, we have to remove the primary airwave from the recorded data, while keeping that part of the airwave that has diffused into the Earth and then back to the surface and into the air. For sources and receivers on the surface, we found an effective way to accomplish what we call 'partial airwave removal',

which only removes the primary component that travels directly from source to receiver and therefore also gets rid of its related repeatability errors. We present numerical examples that test if this idea still works in the presence of near-surface heterogeneities or significant surface topography.

## 7.2   THE AIRWAVE EFFECT

We will explain the impact of the airwave on the monitoring problem with a simple example, assuming a flat horizontal surface and a homogeneous half space. Figure 7.1 sketches the configuration of a land CSEM monitoring problem. We consider a reservoir under production in a 2 $\Omega$m homogeneous half space. The reservoir has dimensions of 2 km by 2 km by 0.5 km and consists of a hydrocarbon-bearing and a water-bearing part. The hydrocarbon-bearing part has a resistivity of 100 $\Omega$m, and is a 300-m thick layer at a depth of 1 km below the air-earth interface. Below it, a 200-m thick water-bearing layer has a resistivity of 0.3 $\Omega$m. For the monitoring study, we assume the reservoir is flooded by saline water from the top left, creating a small, 100-m thick, box-shaped depleted zone in the corner of the hydrocarbon-bearing layer. Moreover, we also assume that the CSEM measurements are available in the frequency domain. We computed the electric field response for this time-lapse configuration with a multigrid solver (Mulder, 2006).
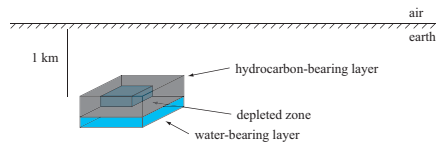


**Fig. 7.1**   Geometry of a simple monitoring problem.

Figure 7.2 displays the amplitude behavior of the time-lapse difference for the $x$-directed electric field measured on the surface, excited by a unit $x$-directed horizontal electric dipole (HED) point source located at (11,9.5,0) km and operating at 1 Hz. The time-lapse difference shown in the bottom-left panel of Figure 7.2 is laterally confined to the location of resistivity change. In practice, we will not obtain such a nice result because repeatability errors will affect the time-lapse measurements. These will have instrumental as well as natural causes, for instance, frost, and will appear as multiplicative noise in the recorded data before and after production. As an illustration, we use the same approach as used in the Chapter 5, mimicking repeatability errors by adding random numbers to

the measured electric fields with a maximum amplitude of 1% relative to the signal strength at each receiver. The bottom-right panel of Figure 7.2 shows that this noise imposes a strong source imprint and completely masks the time-lapse signal. We therefore have to better understand what is going on when we try to detect the time-lapse resistivity changes in the reservoir.
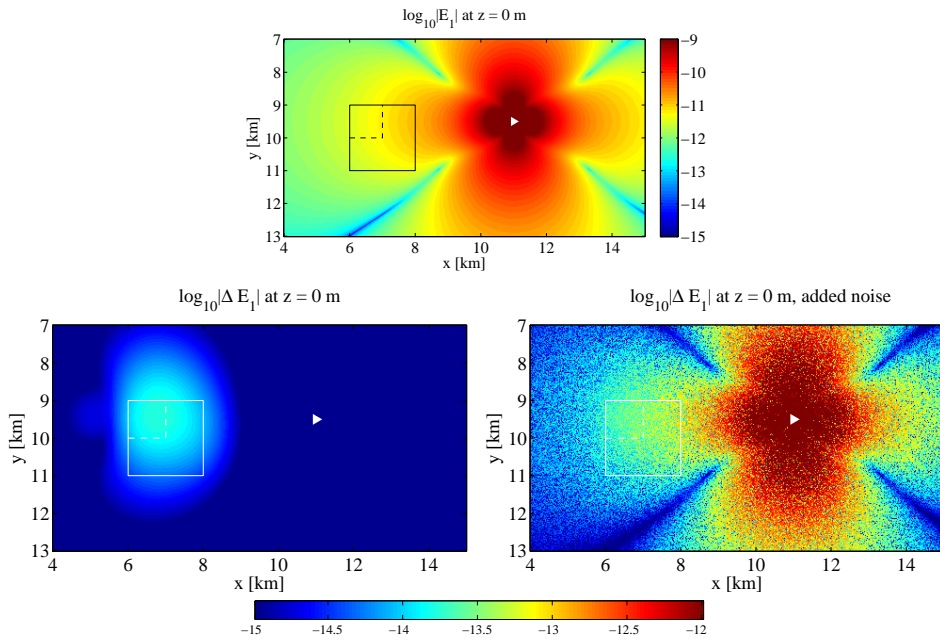


**Fig. 7.2**    The electric field in the $x$-direction recorded at the surface in top view at 1 Hz. The total field before production (top). The time-lapse difference without noise (bottom-left). The time-lapse difference with noise (bottom-right). The solid black box indicates the lateral position of the reservoir and the dashed black line indicates the lateral position of the oil-water interface after flooding. The small white triangle marks the lateral location of the HED source.

The depleted volume can be considered as a scattering object. To first order, the time-lapse difference is the scattered field, contaminated by repeatability errors in the total field. The behavior of the secondary fields is determined by the extent, depth, and the resistivity contrast of the depleted zone, as well as the background signals that are excited by the source (e.g. Tehrani and Slob, 2010). Since extent and resistivity contrast of the depleted zone present an existing situation, the detectability of the time-lapse change depends primarily on the incoming fields at the depleted zone. For the model shown in Figure 7.1, we can simply use the solution for a homogeneous half-space (Raiche and Coggon, 1975), ignoring

higher-order scattering inside the reservoir. Figure 7.3 shows a vertical cross-section through the source of the incoming electric field excited by an $x$-directed HED point source. The color shows the amplitude of the electric field on a logarithmic scale. The black arrows follow the current. Apart from the direct field of the source, there is a significant contribution at shallow depths from the airwave, which is the electromagnetic field that propagates in the air with the speed of light. The part that propagates along the surface is called a lateral wave. It sends a field into the ground with an almost vertical diffusion direction (Baños, 1966).
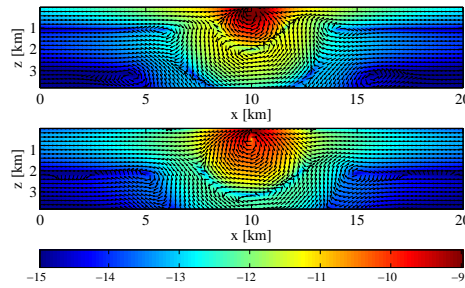


**Fig. 7.3** Electric-field vector plots in a vertical section of a 2 $\Omega$m half-space model excited by an $x$-directed HED point source. The source is located at (10,0,0) km, just below the air-earth interface, and operates at 1 Hz. The top panel displays the real part of the electric field (the in-phase mode), whereas the bottom panel shows its imaginary part (the out-of-phase mode).

Generally, with an HED source on the surface the EM fields are composed of two types: the direct field and the airwave, which can be separated following Slob *et al.* (2010). The airwave amplitude is proportional to inverse horizontal distance to the power three, while it shows an exponential decay as a function of depth. The direct field diffuses through the ground and shows an exponential decay as a function of distance. Separate analysis of each contribution shows that the airwave dominates for offsets exceeding 2 km, both on the surface and at the depth of the depleted volume. From this analysis it follows that the airwave provides the largest contribution to the time-lapse signal if the source is not too nearby. The fact that the airwave is also the predominant signal on the surface will create large multiplicative repeatability errors in the time-lapse measurements. Let us look at this in more detail. With time-lapse measurements, we collect two data sets, before and after production. The latter can be expressed as $\mathbf{E}^d + \mathbf{E}^{aw} + \mathbf{E}^{d;sc} + \mathbf{E}^{aw;sc}$. The first two terms denote the incident fields, with the direct field and the primary airwave contribution, whereas the last two terms denote the scattered fields
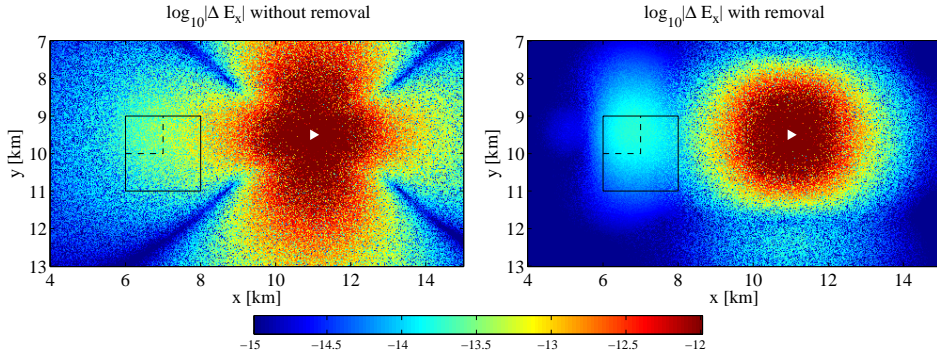
**Fig. 7.4**    On the left, the time-lapse difference of the electric field in the $x$-direction
recorded at the surface in top view at 1 Hz, as in the right panel of Figure 7.2.
On the right, the result after partial airwave removal.

representing the time-lapse change. If we assume this change is entirely due to the
resistivity change in the reservoir, the component $\mathbf{E}^d + \mathbf{E}^{aw}$ will cancel out when
considering the measurements at different times. In the presence of multiplicative
noise, however, the difference becomes $\alpha(\mathbf{E}^d + \mathbf{E}^{aw}) + \mathbf{E}^{d;sc} + \mathbf{E}^{aw;sc}$, where the
factor $\alpha$ models the multiplicative repeatability errors. For $|\mathbf{E}^{d;sc} + \mathbf{E}^{aw;sc}| \ll$
$|\alpha(\mathbf{E}^d + \mathbf{E}^{aw})|$, this noise becomes a problem as illustrated in the bottom-right
panel of Figure 7.2.

From these results, we conclude that the airwave can be beneficial if we can
reduce or remove the contribution $\mathbf{E}^{aw}$ due to the primary airwave generated by
the source, while maintaining the part of the airwave $\mathbf{E}^{aw;sc}$ that is transmitted
into the ground, has a large enough amplitude at reservoir depth, and can produce
a significant time-lapse response. This leads us to the concept of 'partial airwave
removal'.

## 7.3   PARTIAL AIRWAVE REMOVAL

In the time domain, the airwave related to a delta-function source at the surface
shows up as an instantaneous delta spike, which can be surgically removed from
the data. Because the Fourier transform of delta function has a flat spectrum,
we propose to perform partial airwave removal in the frequency domain by
comparing CSEM measurements at two distinct frequencies. This approach
remotely resembles the method proposed by Maaø and Nguyen (2010), but is
essentially different. Their frequency-differencing amounts to data weighting with
a factor proportional to time, with the purpose of boosting later arrivals that have

seen deeper structures. Noise is boosted as well, so the method requires data with a good SNR. For time-lapse measurements, we only want to remove the primary airwave from the measurements to improve the SNR of the time-lapse signal. We therefore select two frequencies that are sufficiently far apart. One should be low enough to have a skin depth of the order of the target depth, so that it sees the reservoir. The other should be high enough to only sense the near surface. Subtracting the two will emphasize the signal from the deeper target and remove the repeatability errors from the primary airwave.

We will illustrate the method by numerical examples. As a first test, we applied partial airwave removal to the earlier monitoring example. Figure 7.4 displays the results. The left panel of Figure 7.4 shows the time-lapse difference at 1 Hz in the presence of multiplicative noise before applying the removal. For the right panel of Figure 7.4, we first subtracted the measured responses at 10 Hz and then computed the time-lapse difference. Now, the lateral extent of the depleted zone is better defined, even in the presence of repeatability error.

In the second test, we considered the effect of topography on the airwave. Figure 7.5 shows the elevation model, with a largest difference in height of 1 km. The reservoir is located 1 km below the hilly area, whereas the source is placed in the valley, 600 m below the highest point, as indicated by a white star. Figure 7.6 shows the $x$-component of the electric field measured on the surface. The left panel shows the time-lapse difference at 1 Hz without and the right panel with partial airwave removal using the response at 10 Hz. Clearly, after removal the lateral extent the depleted zone is better defined.

The third test involves a heterogeneous background but a flat surface. We used the same model as in Wirianto *et al.* (2010a) with a slight modification. Instead of vertical, piston-like displacement, we assumed that the oil production only affects the small area shown in Figure 7.7. A unit dipole source in the $x$-direction was positioned on the surface at $(x,y)$ = (12000, 9500) m. The frequency was set to 5 Hz. The left panel of Figure 7.8 shows the time-lapse difference of $x$-directed electric field measured on the surface without and the right panel of Figure 7.8 with partial airwave removal using the EM field at 10 Hz. The results show that the method also performs well with a heterogeneous resistivity model. Again, the lateral extent of the depleted zone is better defined, even in the presence of repeatability errors.

## 7.4   CONCLUSIONS

The airwave can produce a better time-lapse signal in the presence of repeatability noise than the direct field from the source, because we are able to remove the
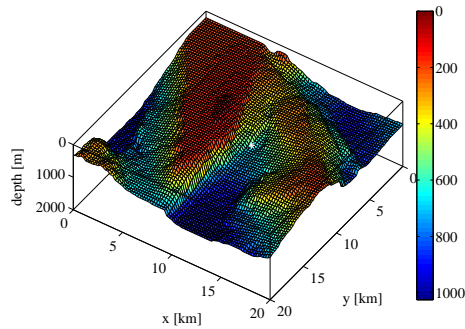
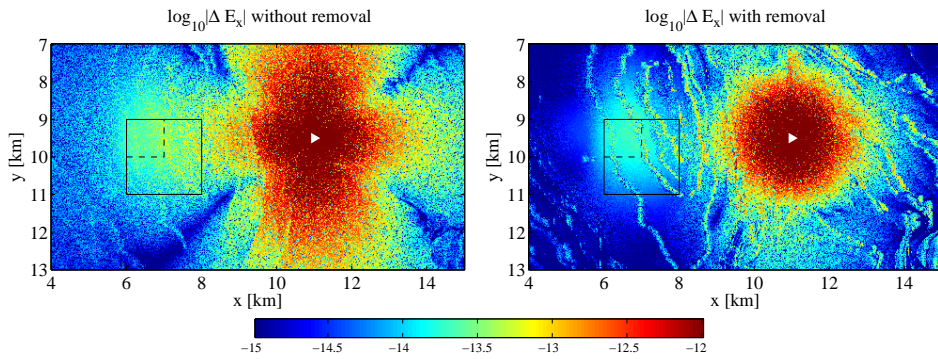**Fig. 7.5**   Topography model.



**Fig. 7.6**   As described in Figure 7.4, but with topography.

primary airwave component. This is common practice in time-domain measurements. We proposed a similar approach for frequency-domain measurements. Subtracting a simultaneous measurement of data at a higher frequency from a measurement at a lower frequency that has a large enough skin depth to reach the reservoir removes the airwave and its related multiplicative noise from the time-lapse data.

Numerical experiments demonstrated a substantial improvement of the signal-to-noise ratio of the time-lapse signal after partial airwave removal, not only in a homogeneous background model, but also with topography or strong heterogeneities. Our results indicate that the concept of partial airwave removal potentially opens up a new avenue for land CSEM reservoir monitoring using frequency-domain systems. One of the remaining issues is the optimal choice of the pair of frequencies for partial airwave removal. Another is its practical use in a field test.
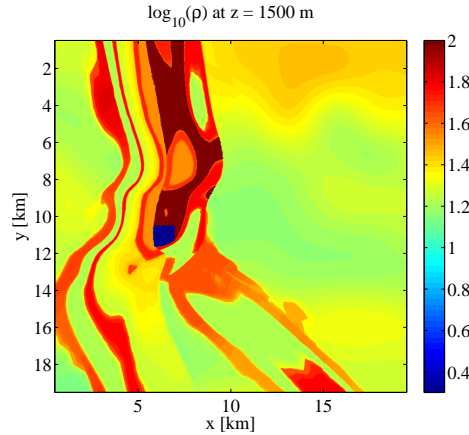
**Fig. 7.7** The horizontal slice of the model at the depth of the depleted volume. The dark blue color indicates the depleted volume.
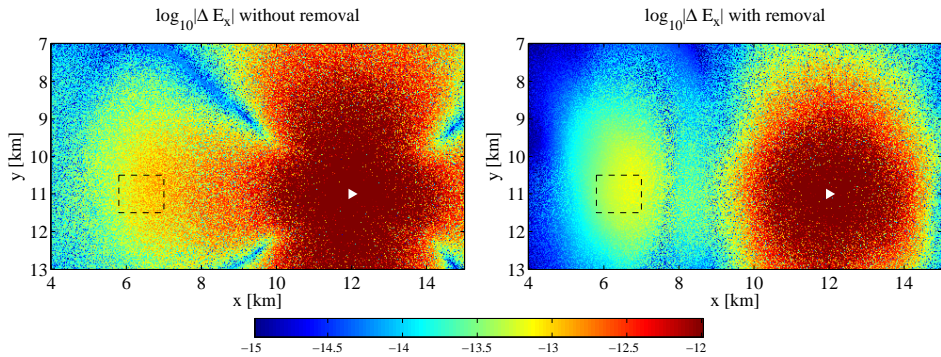


**Fig. 7.8** The left and right panels are similar to Figure 7.4, but for a heterogeneous background. We applied a frequency of 5 Hz to observe the target and 10 Hz to model the airwave effect on the near surface. In each panel, the dashed black line indicates the lateral position of the oil-water interface after flooding. The small white triangle marks the lateral location of the HED source.

# 8 Incorporating EM inversion into reservoir monitoring

**SUMMARY**

In the application of controlled source electromagnetics for reservoir monitoring on land, the time-lapse signal measured with a surface-to-surface acquisition can reveal the lateral extent on the surface of resistivity changes at depth in a hydrocarbon reservoir under production. However, a direct interpretation of the time-lapse signal may generally be difficult and biased. We investigated if non-linear inversion can use time-lapse responses to characterize the subsurface resistivity changes. We examined two different strategies, using a full non-linear inversion algorithm as the interpretation tool: inverting the reference and monitor data independently or in sequence. In the second case, the inversion result of the reference data set serves as an initial guess for the inversion of the monitor data set. Numerical examples show that independent inversion of the data sets can provide an estimate of the depth and lateral extent of the resistivity changes. The second strategy of sequential inversion produces less satisfactory results. We illustrate the independent inversion approach for an example with large survey repeatability errors and another one with a complex overburden.

## 8.1   INTRODUCTION

While exploration is the main application of the controlled-source electromagnetic (CSEM) method these days, current developments are also moving toward monitoring a hydrocarbon reservoir during production. Water flooding or steam injection for enhanced oil production creates resistivity changes in the reservoir, and if those changes are large enough, we can expect them to show up in the CSEM response of a time-lapse survey.

Several recent papers lead to the optimistic conclusion that resistivity changes due to displacing oil by brine can produce a small but measurable change in the CSEM responses (see Lien and Mannseth, 2008; Orange *et al.*, 2009; Wirianto *et al.*, 2009, 2010a). Interestingly, the time-lapse changes in the CSEM response of subsurface resistivity variations, measured with a surface-to-surface acquisition geometry, can directly reveal the lateral extent of the subsurface changes. Since the resistivity structure of the earth is usually complex, a direct interpretation of time-lapse responses in terms of resistivity changes in the earth can, of course, be difficult and biased. In this case, incorporating EM inversion may provide better results.

In this chapter, we present a synthetic study with the aim to investigate the potential use of non-linear EM inversion to process time-lapse data in order to retrieve resistivity changes. We examine two different strategies of EM inversion: inverting the two data sets independently and in sequence. In the first, we invert for resistivity model independently for each data set and then compare the result. In the second, the inversion result of the reference data set serves as an initial guess for the inversion of the monitor data. This chapter is arranged as follows. We first review the governing equations in the frequency domain, their discretization, and the solution method. Then, we outline the EM inversion scheme used for this study. Finally, we present numerical examples investigating the potential use of EM inversion for monitoring.

## 8.2   PROBLEM FORMULATION

As a synthetic test study, we consider the isotropic case. Generalization to the VTI case is straightforward, but a general conductivity tensor can be challenging. To distinguish data between two time instances of observation, we use the superscript $(1)$ to indicate data at the reference state $t = t^{(1)}$ and the superscript $(2)$ for data at the monitor state $t = t^{(2)}$.

The behaviour of electromagnetic field in conducting media can be described by Maxwell's equations and Ohm's law (c.f. Ward and Hohmann, 1987; Jackson,

1999; Griffiths, 1999). In the frequency domain at an angular frequency $\omega$, these can be combined into

$$i\omega\mu_0\tilde{\sigma}^{(1,2)}\mathbf{E}^{(1,2)} - \nabla \times \mu_r^{-1}\nabla \times \mathbf{E}^{(1,2)} = -i\omega\mu_0\mathbf{J}_s, \tag{8.1}$$

where $\mathbf{J}_s(\mathbf{x}, \omega)$ denotes the current source. The parameters $\tilde{\sigma}^{(1,2)}(\mathbf{x}) = \sigma^{(1,2)} - i\omega\epsilon_0\epsilon_r$, with $\sigma(\mathbf{x})$ the conductivity, $\epsilon_r(\mathbf{x})$ the relative permittivity, $\mu_r(\mathbf{x})$ the relative permeability, and $\epsilon_0$ and $\mu_0$ their absolute values in vacuum. Here, we assume that time-lapse changes occur only in the conductivity (or resistivity). The electric permittivity and magnetic permeability remain unchanged.

To compute a numerical solution of Equation 8.1, we use the solver developed by Mulder (2006). The equations are discretized by the Finite Integration Technique (Weiland, 1977) and the resulting equations are solved with an iterative method, BiCGStab2 (van der Vorst, 1992; Gutknecht, 1993), preconditioned by a multigrid solver. The method is matrix-free: we never explicitly form the large sparse linear matrix that describes the discretized problem but only evaluate its action on the latest estimate of the solution, thereby reducing storage requirements. Perfectly electric conducting (PEC) boundary conditions are used where the model is truncated. To reduce the influence of these unrealistic boundary conditions on the resulting solution, we applied grid stretching to move them sufficiently far away from the region of interest. The magnetic field, $\mathbf{H}$, is obtained from the discretized relation

$$\nabla \times \mathbf{E} = -i\omega\mu_r\mu_0\mathbf{H}.$$

## 8.3   NON-LINEAR EM INVERSION

In this study, we assume that we only have electric data. The extension to magnetic data is fairly straightforward. With observed electric data, $e_{s,r,f}^{\text{obs}}$, excited by a source at $\mathbf{x}_s$ for frequency $f$ and observed at receiver positions $\mathbf{x}_r$, the EM imaging problem consists of finding a model that minimizes the weighted least-squares functional

$$J(\boldsymbol{p}) = \left[ \frac{1}{2} \sum_{s,r,f} \|w_{s,r,f}^e \Delta e_{s,r,f}(\sigma[\boldsymbol{p}])\|^2 \right] + R(\boldsymbol{p}),$$

where

$$\Delta \boldsymbol{e}_{s,r,f}(\sigma[\boldsymbol{p}]) = \boldsymbol{e}_{s,r,f}(\sigma[\boldsymbol{p}]) - \boldsymbol{e}_{s,r,f}^{\text{obs}}.$$

Here, $\boldsymbol{e}_{s,r,f}$ represents the computed electric response, obtained by solving Equation 8.1, and $w_{s,r,f}^e$ are data weights that depend on source, receiver, and frequency.

$R(\boldsymbol{p})$ represents an additive regularization term, used to stabilize the inversion process (Vogel, 2002; Zhdanov, 2002). As model parameters, we consider a field $\boldsymbol{p}(\mathbf{x})$. Representing these on a finite-volume mesh with a total of $M$ cells, we may express the parameters as a vector $\boldsymbol{p} \in \mathbb{R}^M$. In the implementation, $\boldsymbol{p}$ can correspond to, for instance, the conductivity, resistivity, logarithm of the resistivity or exponentiation to some power. Here, we chose $\boldsymbol{p}$ as the logarithm of the resistivity.

Following the approach of Plessix and Mulder (2008), we minimize the functional $J$ with a quasi-Newton optimization approach, a limited-memory version of the Broyden-Fletcher-Goldfarb-Shanno (BFGS) method (Byrd $et$ $al.$, 1995). In this method, the update $\boldsymbol{p}^k$ at iteration $k$ is given by

$$\boldsymbol{p}^k = \boldsymbol{p}^{k-1} - \alpha^{k-1}\tilde{\mathbf{K}}^{k-1}\nabla_{\boldsymbol{p}}J(\boldsymbol{p}^{k-1}),$$

where $\alpha^{k-1}$ is a real scalar value obtained by a line-search algorithm, $\tilde{\mathbf{K}}^{k-1}$ is the approximate inverse of the Hessian, computed by the BFGS algorithm, and $\nabla_{\boldsymbol{p}}J(\boldsymbol{p}^{k-1})$ is the gradient of the least-square functional. In its practical implementation, the gradient of the least squares functional is computed by the adjoint method (e.g. Lions and Magenes, 1972; Giles $et$ $al.$, 2003; Plessix, 2006).

To improve the convergence rate, a preconditioner is used. Following Plessix and Mulder (2008), we implemented the preconditioner as a scaling of the unknowns, $\boldsymbol{p}$. With $\mathbf{D}$ a regular real-valued matrix of size $M \times M$, we defined the scaled unknown, $\tilde{\boldsymbol{p}}$ by

$$\tilde{\boldsymbol{p}} = \mathbf{D}^{-1}\boldsymbol{p}.$$

We chose $\mathbf{D}$ as a depth weighting of the form

$$\mathbf{D}(x, y, z) = \frac{\beta}{1 + \exp(-\frac{z-z_b}{\delta})} \quad \text{for } z > 0,$$

where $\beta$ and $\delta$ are positive and $z_b$ is a reference depth. This depth weighting crudely balances the shallow and deeper resistivity updates during the inversion.

## 8.4   RESULTS

We present a number of examples that highlight the challenges that appear when attempting to incorporate EM inversion in a monitoring problem. We first illustrate the performance of our EM inversion approach for an exploration problem with a simple subsurface model. We then present and discuss results obtained by EM inversion applied to a monitoring problem in the same simple
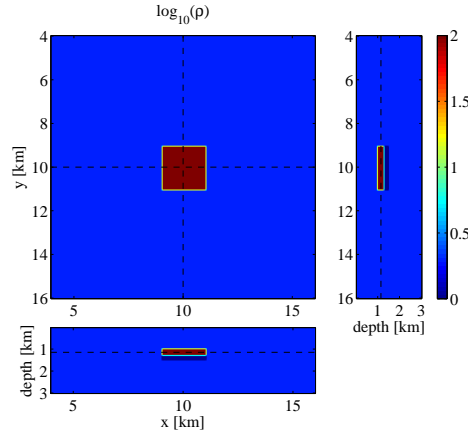
**Fig. 8.1**   True resistivity model plotted on a logarithm scale. On the top-left, an $xy$-plane cross-section of the model at depth of 1.2 km. On the top-right, a $yz$-plane cross-section at $x = 10$ km. On the bottom, an $xz$-plane cross-section at $y = 10$ km. The black dashed lines indicate the position of the cross-sections. The hydrocarbons result in a high resistivity, colored red, and the brine-filled rock leads to a low resistivity, colored dark blue.

subsurface model. We consider two different inversion strategies for processing the time-lapse data set, one in which the reference and monitor data are inverted independently, and one where we use the inversion of the reference data as an initial guess for inverting the monitor data. Finally, we investigate how a complex model affects the inversion of an EM monitoring problem.

### 8.4.1   EM inversion test

In order to investigate and illustrate the performance of our non-linear inversion approaches, we created a synthetic EM survey for a simple model of a reservoir. Figure 8.1 shows the model. A reservoir is embedded in a $2\,\Omega$m homogeneous half-space. The reservoir has dimensions of 2 km by 2 km by 0.5 km and consists of a hydrocarbon-bearing and a water-bearing part. The hydrocarbon-bearing part is a 300-m thick layer at a depth of 1 km below the air-earth interface and has a resistivity of 100 $\Omega$m. Below it, a 200-m thick water-bearing layer has a resistivity of 0.3 $\Omega$m.

In this model, we generated 'observed' data. Figure 8.2 displays the acquisition geometry. Given a source at $x = x_s$ laid down on the surface, we measure the responses with six receiver lines on the surface with a 500 m spacing between the lines. Each line contains 82 receivers with a 100 m spacing between the stations.
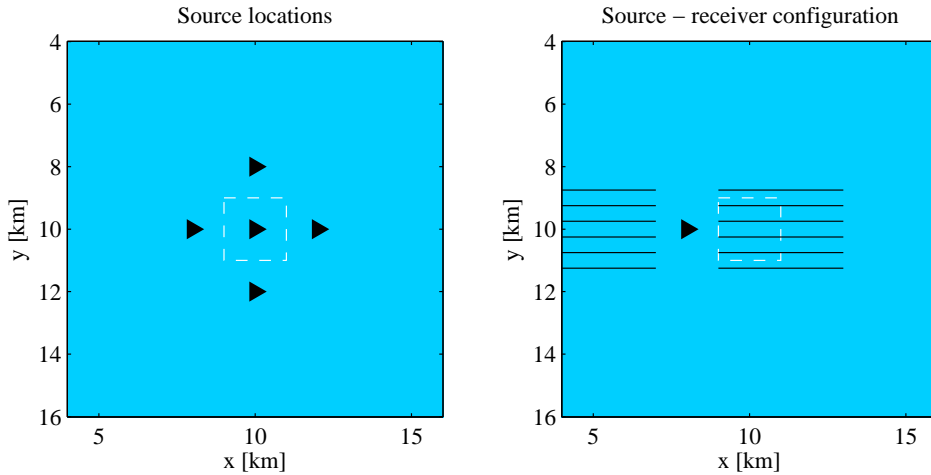
**Fig. 8.2**  On the left, a map view of source locations. On the right, the configuration of source-receiver for a source at $(x,y)$ = (8,10) km.  The white dashed line indicates the outline of reservoir.

They are located between $x = x_s - 5$ and $x = x_s + 5$ km, excluding the short offsets between $x = x_s - 1$ and $x = x_s + 1$ km.  Here, only the in-line electric components were recorded.  To have both depth and lateral coverage, we used three frequencies, 10, 1, and 0.1 Hz, and five sources.  We could, of course, have considered more frequencies and more sources to improve the coverage and illumination, but that would increase the required computational time.  Therefore, we compromised by using only three frequencies and five sources, leading to 15 source-frequency pairs.  Sources were located just below the surface in the configuration displayed in Figure 8.2. We did not add noise to data.

For the imaging, the inversion model has a size of 20 km by 20 km by 4.7 km on a grid with a 100 m spacing in the $x$- and $y$- directions, and a 50 m spacing in the $z$- direction, leading to over 3 millions unknowns to be resolved. During the runs, each frequency response was computed on a computational grid different from the model parameters' grid. Consequently, a projection or interpolation operator was required to map the model from the inversion grid to the computational grid. Here, we applied piecewise linear interpolation in the conductivity-space domain. We ran the inversion in parallel on 15 CPUs, each handling one source for one frequency at the time.

The initial model for the inversion was a $2\,\Omega$m homogeneous half-space. The left panel of Figure 8.4 shows the normalized errors between the synthetic computed with the initial model and the 'observed' data, computed for the true model.
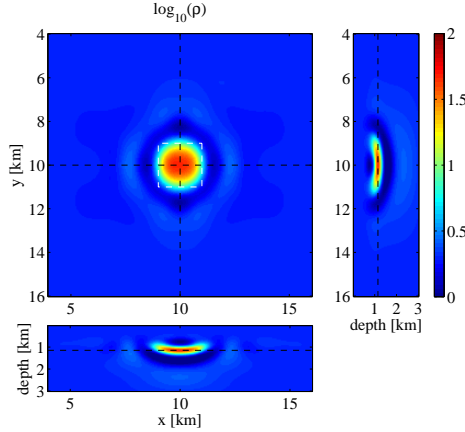
**Fig. 8.3**  As Figure 8.1, but for the recovered resistivity model at iteration 30. The white
dashed line indicates the outline of the reservoir.

The reservoir is clearly visible at 1 and 0.1 Hz. The small normalized errors at
10 Hz were expected because the resistivity body is absent in the shallow part and
the high frequencies are almost insensitive to the deeper part of the model.

To stabilize the inversion, we implemented the minimal change regulariza-
tion (Vogel, 2002; Zhdanov, 2002):

$$R(\boldsymbol{p}) = \lambda \, \|\boldsymbol{p} - \boldsymbol{p}^{\text{ref}}\|^2$$

where $\boldsymbol{p}^{\text{ref}}$ represents the reference model and $\lambda$ is a positive number. The
reference model equals the initial guess. The constant $\lambda$ is used to balance between
the error and the regularization terms.

The reconstructed resistivity model after 30 iterations is shown in Figure 8.3.
We observed that after 30 iterations, the reservoir is well retrieved with the correct
depth and lateral extent. The total cost functional $J$ was reduced to about 2%
of its initial value (see Figure 8.5). The poor resolution was expected because of
the diffusive nature of the EM fields and the ill-posedness of the inverse problem.
We also notice so-called 'inversion smiles'. These are due to having only in-
line measurements (Plessix and Mulder, 2008). The normalized errors after 30
iterations are shown in the right panel of Figure 8.4. Obviously, the inversion
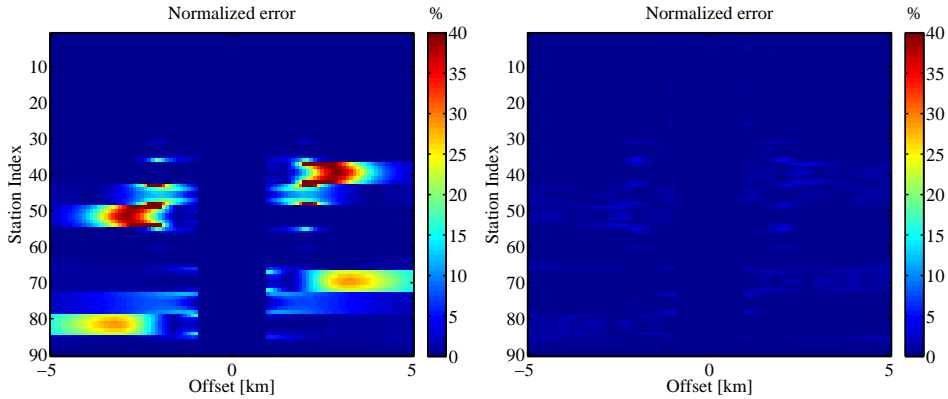result explains the data well.

**Fig. 8.4**   The normalized errors between the synthetic data and the 'observed' data computed with the true model. On the left, the normalized errors at the initial iteration, while on the right panel at iteration 30. The station indices from 1 to 30 correspond to a frequency of 10 Hz, between 31 and 60 to 1 Hz, and between 61 and 90 to 0.1 Hz. Notice that data were absent in the offset range between −1 km and 1 km.
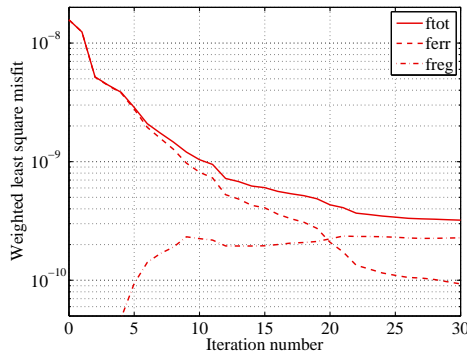


**Fig. 8.5**   The decrease of the weighted total cost function with iteration number. The dashed line indicates the contribution from the error function and the dashed-dotted line from the regularization term.

### 8.4.2   Inversion strategies for EM monitoring

The previous example suggests that our inversion approach performs well when inverting an exploration data set. Next, we use this tool to investigate the feasibility of incorporating non-linear inversion into the monitoring problem.

As a starting point, we created a synthetic time-lapse data set. We repeated the previous test for the reference and the monitor model. The reference model is
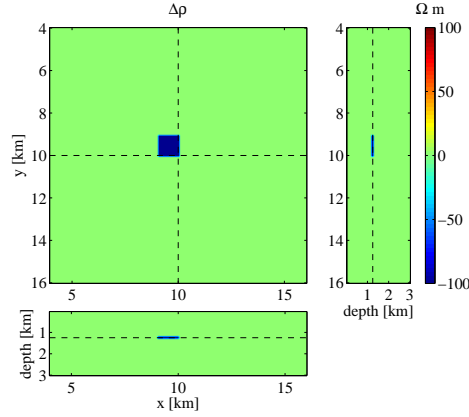
**Fig. 8.6** The true resistivity difference. On the top-left, a $xy$-plane cross-section of the resistivity difference at depth of 1.2 km. On the top-right, a $yz$-plane cross-section at $x = 10$ km. At the bottom, an $xz$-plane cross-section at $y = 10$ km.

the same as in the previous test. For the monitoring model, we assumed that the reservoir was flooded by saline water from the top left, creating a small, 100-m thick, box-shaped depleted zone in the corner of the hydrocarbon-bearing layer. Figure 8.6 displays the resistivity difference between the reference and the monitor models.

For these two models, we created a synthetic time-lapse data set $e^{(1)}$ for the reference state and a data set $e^{(2)}$ for the monitor state, computed with the same acquisition geometry as the previous example. We assumed idealized conditions, i.e., the difference in EM response is entirely due to resistivity changes in the reservoir. Repeatability errors such as positioning errors and changes in the near surface were not yet considered.

Let the result of inversion of the reference data be $\rho^{(1)}$ and that for the monitor data $\rho^{(2)}$. We examine the time-lapse resistivity changes by plotting the difference $\Delta\rho$ as well as the normalized differences $\Delta^r\rho$ of the inversion results, defined by

$$\Delta\rho = \rho^{(2)} - \rho^{(1)} \quad \text{and} \quad \Delta^r\rho = \frac{\Delta\rho}{\rho^{(1)}}.$$

Measuring just the differences is useful to identify domains where the the resistivity has changed, independent of the original resistivity values, while measuring the normalized differences is useful to identify domains with resistivity changes that are proportional to the resistivity values. For example, a 1 Ω-m difference can be
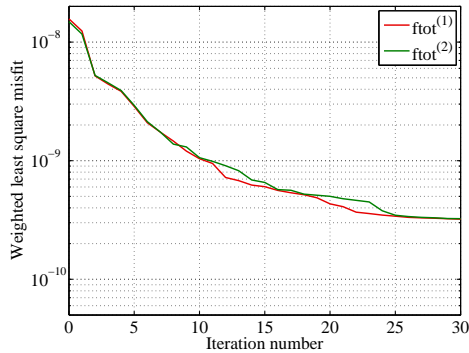
**Fig. 8.7**   As Figure 8.5, but for the reference (red) and the monitor (green) data sets, computed independently.

considered small if it occurs within hydrocarbon-bearing rocks with a resistivity of $100\,\Omega$m, but it is definitely large within water-bearing rocks with a resistivity of $0.3\,\Omega$m. Next, we compare two different strategies for processing a time-lapse data set.

### Strategy 1: independent inversion

The first strategy is to invert the reference and the monitor data sets independently. We ran the inversion twice, once with the reference data set and once with the monitor data set. As before, we used a $2\,\Omega$-m homogeneous half-space as the initial model. Systematic errors may occur during the inversion. To keep them similar for both inversions, we used the same data weighting and inversion parameters for each. Figure 8.7 displays the convergence history for the two inversions. We observe that the two converge with almost the same number of iterations.

The central question with this strategy is how to compare the results. One option is comparison at the same iteration count. Another is comparison at the same threshold value of the misfit functional. The last option appears to be more natural, but it may have difficulty when noise is present in both data sets. In that case, noise may dominate the misfit after several iterations, slowing down its decrease, and the optimization scheme may be unable to even reach the threshold. We have not carried out a detailed investigation of this issue, but choose to work with the first option under the assumption that the systematic errors will largely cancel out when taking the difference of the independent inversion results.

The resistivity differences obtained with this strategy are shown in Figure 8.8 and the normalized differences in Figure 8.9, both computed after performing 30 iterations both on the reference and the monitor data set. As can be seen in
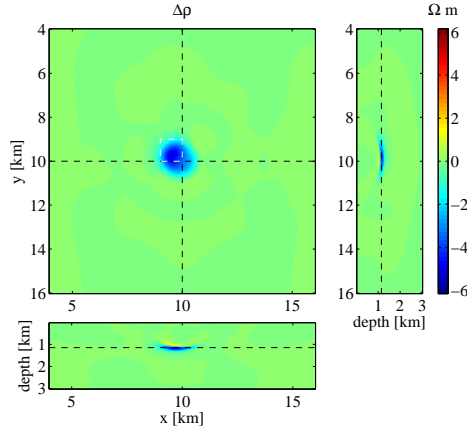
**Fig. 8.8**    As Figure 8.6, but for the difference between the inversion result of the reference and the monitor data sets. The white dashed line indicates the outline of the actual difference.
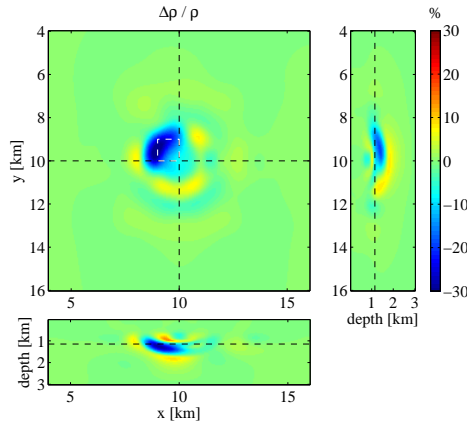


**Fig. 8.9**    As Figure 8.8, but for the normalized difference. The scale is in percent.

Figures 8.8 and 8.9, the inversion result can provide an indication of the depth and the lateral extent of the true resistivity change. However, we notice that the position of the resistivity changes shown in the Figure 8.10 is slightly shifted to the center of the reservoir. Using more sources, receivers, and frequencies may improve the result, but at the expense of more computation time. As observed after inversion of the exploration data set, the poor resolution also remains an issue for EM in the monitoring case.

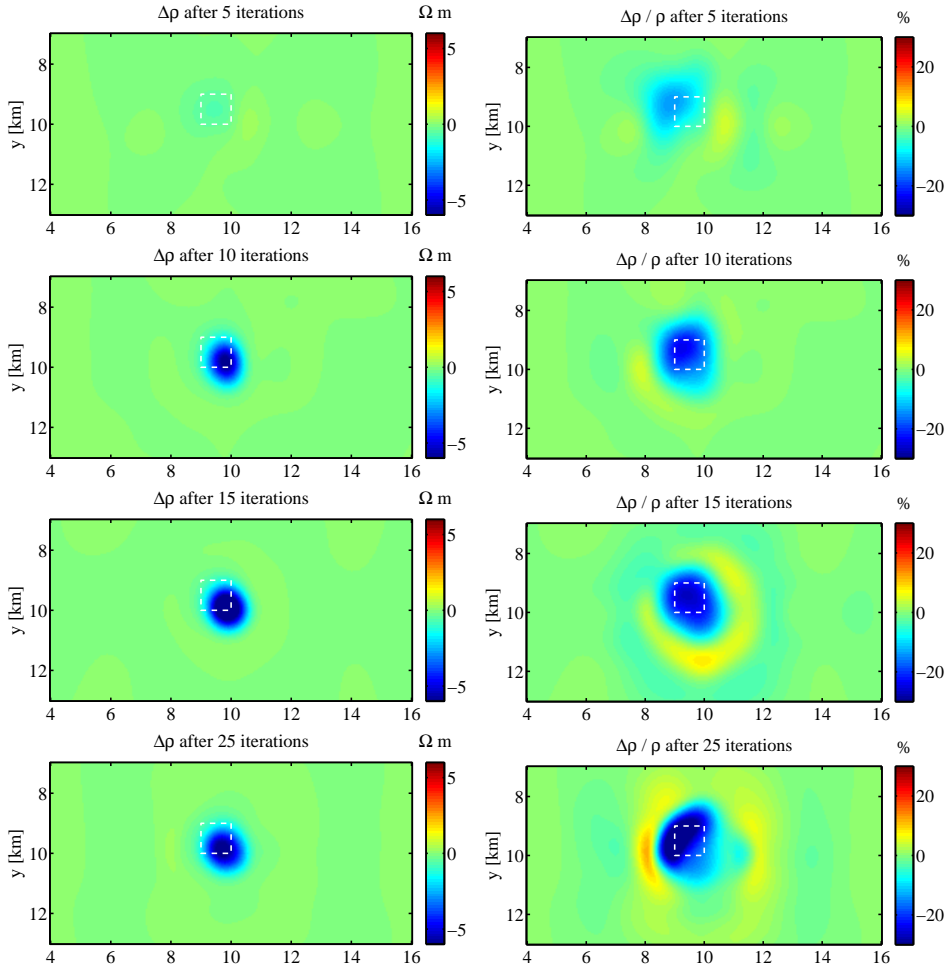To further understand the inversion procedure, we plotted the differences

**Fig. 8.10**  The left panels display the resistivity differences at a depth of 1.2 km observed after 5, 10, 15, and 25 iterations, from top to bottom. The rights panels display the normalized differences.

and the normalized differences of the inversion results at other iteration counts. Figure 8.10 shows the result after 5, 10, 15, and 25 iterations, respectively. Interestingly, the estimated resistivity changes already appear at an early stage of the inversion and then improve when the iteration count increases.

### Strategy 2: sequential inversion

The second strategy is to invert time-lapse data set subsequently: we first invert the reference data set and then use the result as an initial guess for inverting
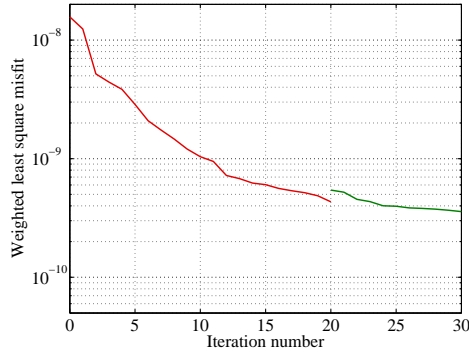
**Fig. 8.11**   The decrease of the normalized misfit function versus iteration number for
the reference (red) and the monitor (green) data sets, computed subsequently.

the monitor data set. As before, we consider both differences and normalized
differences.

Figures 8.11–8.13 show the results. We ran the first inversion for 20 iterations,
just when the misfit reaches about 1% of its initial value. We then started the
second inversion, using the first inversion result as the initial model. Figure 8.11
displays the convergence history for the two inversions. The jump between the
first and the second inversion is caused by switching to the time-lapse response
that happened after displacing oil by brine. Figure 8.12 displays the resistivity
differences and Figure 8.13 the normalized differences. Here, we are comparing
the retrieved model of the second inversion to the one of the first inversion. It
can be seen that the resistivity differences and the normalized differences obtained
with this strategy hardly indicate the true resistivity changes. Figure 8.13 shows
that the result mainly covers the full domain of the second inversion.

As a further test, we restarted the inversion of the reference data set with the
same initial model as the inversion of the monitor data set. This approach is
similar to the first strategy but now with a rather accurate initial model.

Figures 8.14–8.16 show the result. Figure 8.14 displays the convergence history
for the two inversions. Figure 8.15 displays the resistivity differences and the
normalized difference are shown in Figure 8.16. Here, we compare the inversion
result of the reference and the monitor data set after 9 iterations. It can be seen
that the inversion result provides an indication of the depth and the lateral extent
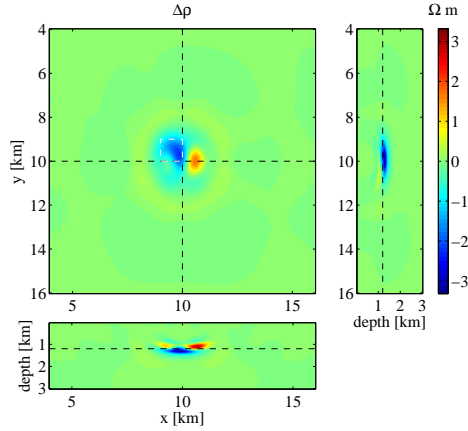of the true resistivity change.

**Fig. 8.12**   As described in Figure 8.8, but for the difference between the inversion result of the reference and the monitor data sets, computed subsequently.
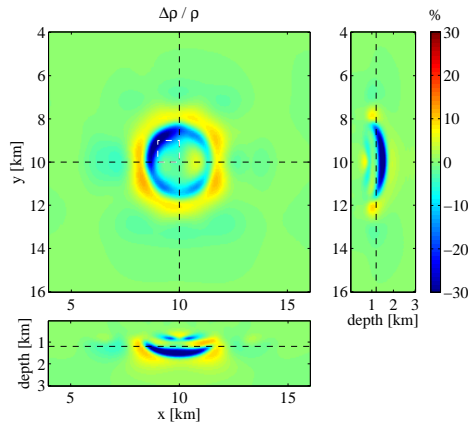


**Fig. 8.13**   As described in Figure 8.12, but for the normalized difference. The scale is in percent.

## 8.5   NOISE

So far, we assumed idealized conditions, i.e., the time-lapse data differences are entirely due the resistivity changes in the reservoir. In practice, repeatability errors will pollute the time-lapse measurements. Next, we investigate the effect of repeatability noise on the inversion result of the time-lapse data.

We use the same approach as Wirianto *et al.* (2010a), mimicking repeatability errors by adding random complex numbers to the measured electric fields. We
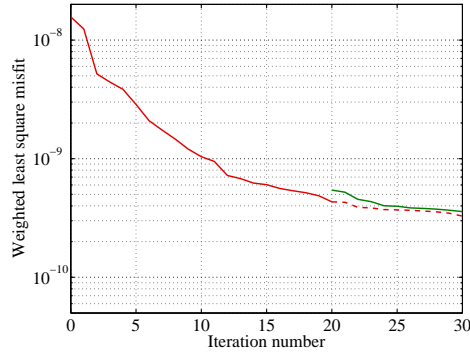
**Fig. 8.14** The decrease of the normalized misfit function versus iteration number for the reference (red) and the monitor (green) data sets, computed subsequently. The red dashed line displays the decrease after restarting with the monitor data set.
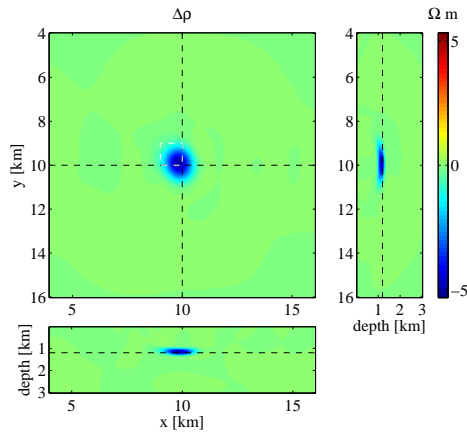


**Fig. 8.15** As described in Figure 8.8, but for the difference between the result of inversion of the reference and the monitor data sets, computed independently with a rather accurate initial model.

assume repeatability errors with a maximum amplitude of 5%, relative to the signal strength at each receiver, which is slightly higher than used in Wirianto *et al.* (2011).

In this example, we chose to work with the first strategy, inverting independently and comparing the inversion results at the same iteration count. Figure 8.17 displays the convergence history for each inversion. The presence of repeatability errors in the monitor data set slows down the decrease of the misfit. Figure 8.18 shows the normalized differences after 5, 10, 15 and 20 iterations. Again, we
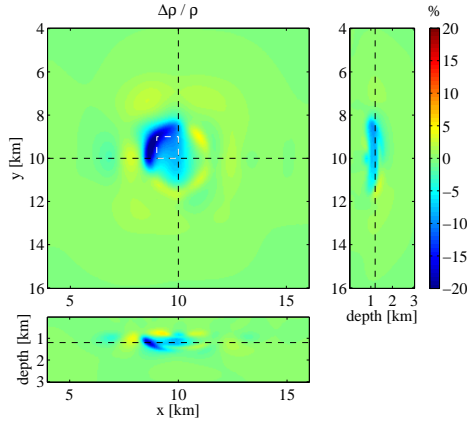
**Fig. 8.16**    As described in Figure 8.15, but for the normalized difference. The scale is in percent.
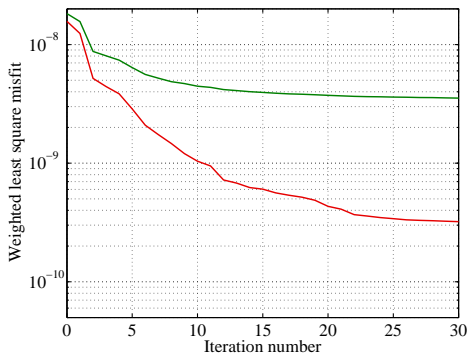


**Fig. 8.17**    The decrease of the weighted misfit function versus iteration number for the reference (red) and the monitor (green) data sets.  Here, we consider 5% multiplicative noise added to the monitor data.

observed here that the inversion result still provides an indication of the depth and the lateral extent of the true resistivity change. Furthermore, it can be seen that the estimated resistivity changes, interestingly enough, already appear at an early stage of the inversion.

## 8.6   SEG/EAGE OVERTHRUST MODEL

The SEG/EAGE Overthrust model (Aminzadeh *et al.*, 1997) provided a template for a realistic and complex subsurface. Originally, this model consists of velocity values, designed for simulating seismic wave propagation. To study whether the
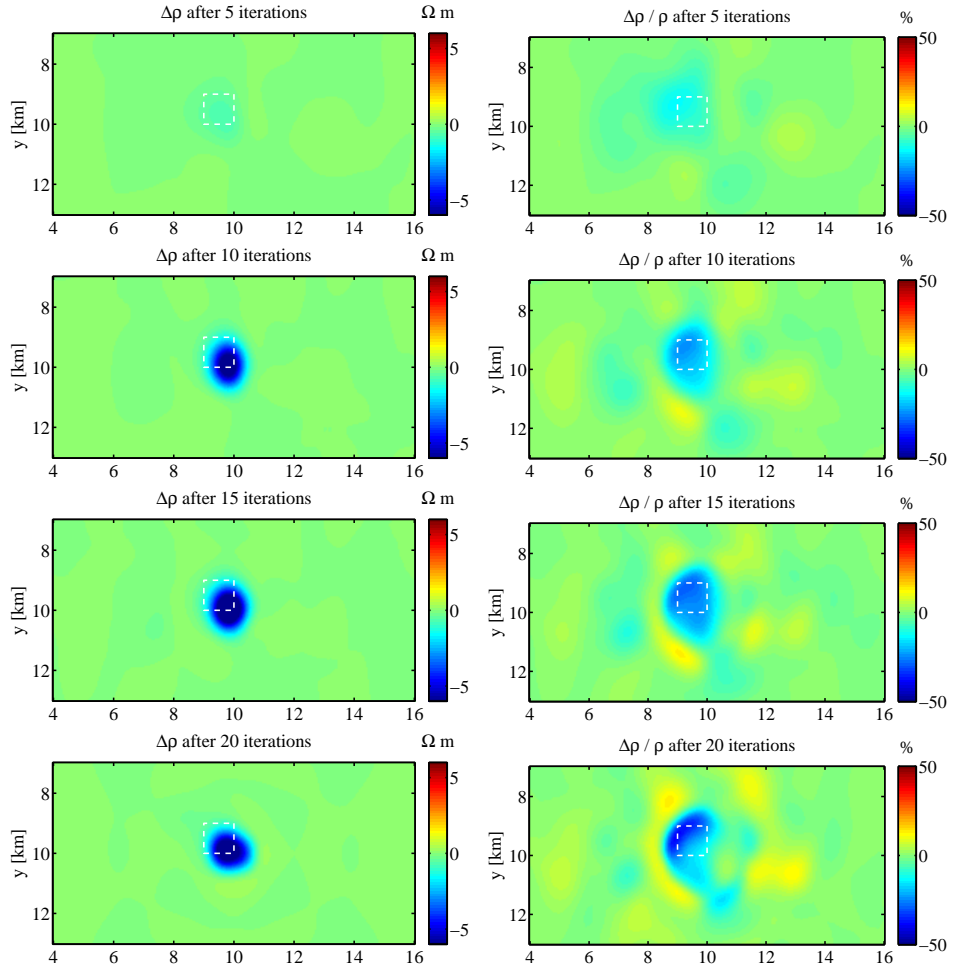
**Fig. 8.18** The cross-section of resistivity changes at depth 1.2 km. These result are after 5, 10, 15, and 20 iterations, shown top-left, top-right, bottom-left, and bottom-right, respectively. The white dashed lines indicate the actual difference. Here, we consider 5% multiplicative noise added to data at the monitoring state.

complexity of model affects the inversion of the EM monitoring problem, we chose to work with this model, replacing velocities by resistivities according to $\rho = (v/1700)^{3.88}$, as suggested by Meju *et al.* (2003). In this 3D model, we selected one part as an artificial reservoir sand that contains oil and water. We refer to Wirianto *et al.* (2010a) for more details about this model.

Figure 8.19 displays the cross-section of the true model for the reference states.
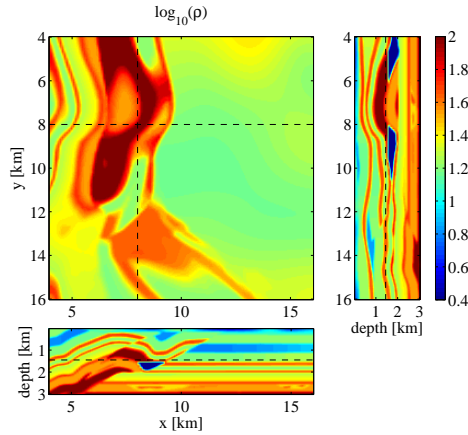
**Fig. 8.19**    Resistivity based on the SEG/EAGE Overthrust model. On the top-left, an $xy$-plane cross-section of the model difference at depth of 1.45 km. On the top-right, a $yz$-plane cross-section at $x = 8$ km. On the bottom, an $xz$-plane cross-section at $y = 8$ km. The reservoir formation lies around $x = 7$ km and between 1.4 and 2.0 km depth. The dark blue part shows the injected water. The oil-bearing sand above it is coloured dark red. The black dashed lines indicate the position of the cross-sections.

For the monitoring state, we assume that the oil-water contact has risen 100 m after water injection. We also assume 100% sweep efficiency, meaning perfect replacement of oil by water.

We generated 'observed' data with those models, resulting in the reference and the monitoring data set. The acquisition geometry is displayed in Figure 8.20. Given a source at $x = x_s$, laid down on the surface, we measure the EM response with six receiver lines on the surface with a 500 m spacing between the lines. Each line contains 82 receivers with a 100 m spacing between the stations. They located between $x = x_s - 5$ and $x = x_s + 5$ km, excluding the short offsets between $x = x_s - 1$ and $x = x_s + 1$ km. Here, only the in-line electric components are recorded. We use three frequencies, 10, 1, and 0.1 Hz, and 13 sources, resulting in 39 source-frequency pairs. We did not add noise to the data.

Figure 8.21 shows the initial model for inversion. We use a smoothed version of the exact model at the reference state. This is, of course, the ideal case, which in reality will require integration of several geophysical data sets. We ran two inversions — one with the reference data set and one with the monitoring data set — and computed the difference. Figure 8.22 displays the model differences and Figure 8.23 the normalized differences, obtained after 22 iterations. It can be seen that the resistivity changes are well retrieved at the correct depth. Some
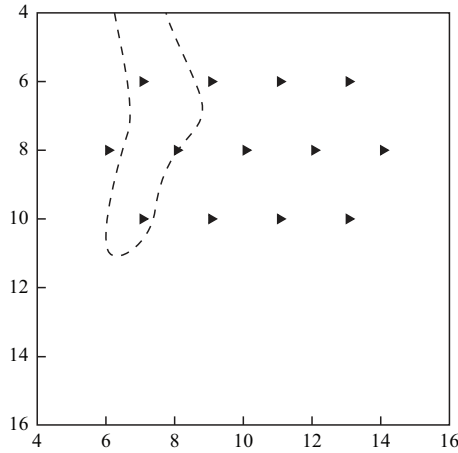
**Fig. 8.20** A map view of the source positions. The dashed line indicates the outline of reservoir.
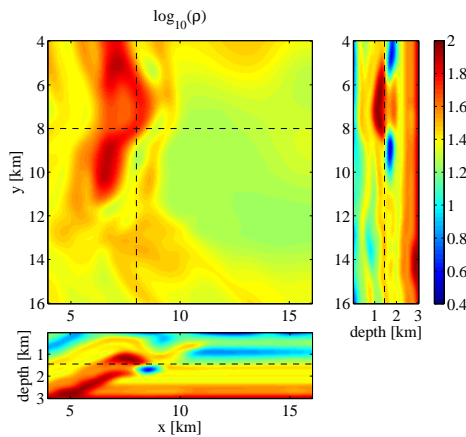


**Fig. 8.21** As Figure 8.19, but using a smoothed version of the true model as initial guess for the inversion of the reference and the monitor data sets.

artifacts, however, appear above the reservoir. This is probably due to having an incorrect overburden model.

## 8.7 CONCLUSIONS

We have studied two different strategies for using non-linear EM inversion to resolve time-lapse changes due to displacing oil by brine. With the first strategy, we inverted the two data sets independently, meaning that we ran the inversion

**Fig. 8.22**   The difference between the result of inversion of the the monitor data set and the initial model. On the top-left, an $xy$-plane cross-section of the model difference at depth of 1.45 km. On the top-right, a $yz$-plane cross-section at $x = 8$ km. On the bottom, an $xz$-plane cross-section at $y = 8$ km. The black dashed lines indicate the position of the cross-sections.
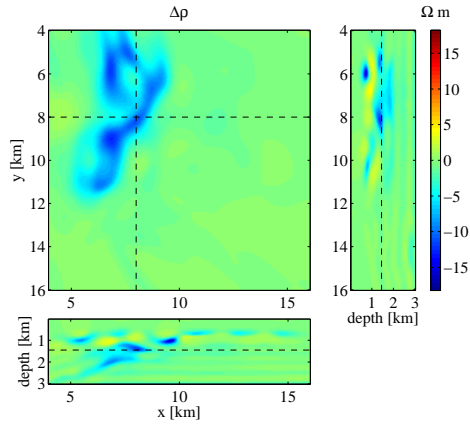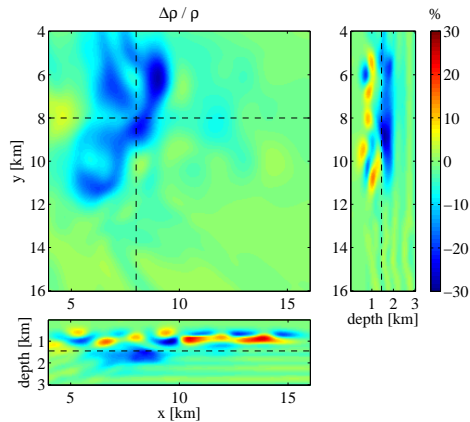


**Fig. 8.23**   As Figure 8.22, but for the normalized difference.

twice, once with the reference data set and once with the monitor data set. The results show that, by maintaining the same inversion parameters, the depth and lateral extent of resistivity changes due to displacing oil by brine can be recovered. Interestingly, the estimated resistivity changes already appear at an early stage of the inversion and then improve when the number of iterations increases. The same behavior is observed when considering noise or a complex overburden. With the second strategy, we inverted the two data sets in sequence. The inversion result

for the reference data set served as an initial guess for the inversion of the monitor data set. In this approach, the differences and normalized differences of the two inversion results hardly indicate the depth and lateral extent of the true resistivity changes. The second inversion result was substantially influenced by the initial model obtained from the first inversion.

Our study suggests that, for the land example considered here, incorporating non-linear inversion into the monitoring problem helps to recover resistivity changes. Although the actual values of the resistivity differences may be difficult to determine, the non-linear inversion does provide an indication of the depth and lateral extent of the time-lapse changes. One of the remaining issues is to incorporate more complex scenarios such as geomechanical changes, compression and compaction, or temperature changes. Another is its practical use in a field test.

# Part III

# Conclusions

# 9 Conclusions and Future Outlook

The first part of this chapter summarizes the conclusions from the earlier chapters. We divide them into two groups: those related to numerical modelling and to the EM monitoring problem. In the second part, we discuss possible extensions of the current work.

## 9.1 CONCLUSIONS

### 9.1.1 Numerical EM modelling

In chapter 2, we compared different methods for synthesizing time-domain solutions. We used complexity analysis to estimate the cost of those numerical methods in terms of the number of unknowns. While some popular methods have an $O(n^4)$ complexity, time-domain solutions obtained from a frequency-domain method have a complexity of $O(n_f n^3)$ Here $n$ is the number of points per spatial coordinate and $n_f$ is the number of frequencies. If $n_f$ is small relative to $n$, the frequency-domain method appears as an attractive choice.

In chapter 3, we studied some effects of time weighting on time-domain EM inversion. The results show that simply muting the early-time transient EM data may lead to unsatisfactory inversion results. Without the early-time response, inversion cannot retrieve the resistivity of the near surface. Due to the diffusive nature of the electromagnetic fields, this also affects the reconstruction of the resistivity at larger depths. Further investigation is required to find the best-suited time weighting for time-domain EM inversion.

In chapter 4, we studied the potential use of the essentially non-oscillatory (ENO) interpolation to accurately sample the modelled EM response near strong resistivity contrasts. We observed that ENO interpolation provides more accurate results near discontinuities than those obtained with standard tri-linear or cubic interpolation. Still, in the examples considered in chapter 4, the discretisation error tends to dominate the final result and ENO interpolation only gives a moderate improvement. However, given its low cost, ENO interpolation still appears to be worthwhile to use.

### 9.1.2  EM monitoring

In chapter 5, we studied the feasibility of using the CSEM method for monitoring changes in the subsurface. Our estimates show that the resistivity change due to displacing oil by brine can produce a small but measurable difference in the CSEM responses. Interestingly, those response differences measured on the surface are confined to the lateral extent of the resistivity changes in the subsurface, even in the presence of repeatability noises. Also, the results indicate that acquisition design plays an important role to best capture the time-lapse signal.

In chapter 6, we carried out numerical experiments to understand how to optimize the acquisition to best capture the time-lapse signal. We demonstrated that the primary airwave can be beneficial for the monitoring problem. It is the dominant signal at the surface, and, when diffused into the Earth, the main source of illumination for the reservoir. However, repeatability errors will affect the primary airwave, just as happens with the direct field, and these can mask the time-lapse signal from the swept reservoir region. To gain maximal benefit from the airwave, we have to remove the primary airwave from the recorded data while preserving that part of the airwave that has diffused into the Earth and then back to the surface and into the air.

This led us to the concept of 'partial airwave removal', introduced in chapter 7. It is a simple and effective method to remove the primary airwave from the data. The idea is to select two frequencies that are sufficiently far apart. One should be low enough to have a skin depth of the order of the target depth, so that is sees the reservoir. The other should be high enough to only sense the near surface. We have demonstrated that the signal-to-noise ratio of the time-lapse signal is substantially improved after partial airwave removal, not only in a homogeneous background model, but also with topography or strong heterogeneities. Our results suggest that the concept of partial airwave removal potentially opens up a new avenue for land CSEM reservoir monitoring using frequency-domain systems.

In chapter 8, we carried out numerical experiments to investigate if non-linear inversion can use time-lapse responses to characterize the subsurface resistivity changes. Particularly, we examined two different strategies using a full non-linear inversion algorithm as the interpretation tool: inverting the two data sets independently and subsequently. Our estimates show that inverting the reference and the monitor data set independently can provide an estimate of the depth and lateral extent of the resistivity changes, even the presence of repeatability noise and a complex overburden. Interestingly, the estimated resistivity changes already appear at an early stage of the inversion and then improve when the number of iterations increases.

## 9.2 FUTURE OUTLOOK

This thesis shows that the application of the controlled-source electromagnetic method to monitoring problem has the potential to play a significant role in the oil and gas industry. Numerical modelling results demonstrated that resistivity changes can produce a small but measurable difference in the CSEM response. With high-quality data and non-linear inversion we can use the time-lapse CSEM data to reveal the deep and lateral extent of resistivity changes. However, further research and development is still required for the CSEM method to reach its full potential for the monitoring problem. Here, we provide a number of possible extensions to the current work. We only considered land CSEM. The extension to marine CSEM is conceptually straightforward.

- The results in chapter 5 suggest that there are optimal distances between sources, receivers, and the target area. If the source is close to the receiver and the target, the signal will be dominated by the direct field and the time-lapse signal will be masked. If the distance is too large, the time-lapse signal will become too weak to be detected. A possible extension to this work is to optimize these source-receiver-target distances for a given resistivity model. Another possible extension is to consider more complex scenarios, taking other source of resistivity changes into account, such as geomechanics changes, compression, compaction, or temperature changes.

- The current approach for the partial airwave removal method in chapter 7 requires two frequencies that are sufficiently far apart. The selection of the two frequencies was done by a trial-and-error. There might be an automated approach to determine the two frequencies, given a resistivity model.

- The current studies are all based on numerical results. An ultimate extension is of course to deal with field data.

- We considered the application of CSEM for monitoring reservoirs during production. An extension is to use the CSEM method for monitoring reservoirs during $CO_2$ injection for sequestration, or for monitoring thermal effects during water injection and production on geothermal applications.

# Bibliography

Aminzadeh, F., Brac, J., and Kunz, T., 1997. *3-D Salt and Overthrust models*, Society of Exploration Geophysicists, Tulsa, Oklahoma.

Amundsen, H. E. F., Johnstad, S. E., and Røsten, T., 2004. A Sea Bed Logging (SBL) calibration survey over the Troll gas field, in *Proceeding 66th EAGE Conference & Exhibition, Expanded Abstracts*, p. E019, European Association of Geoscientists & Engineers.

Archie, G. E., 1942. The electrical resistivity log as an aid in determining some reservoir characteristics, *Petroleum Transactions of AIME*, **146**, 54–62.

Avdeev, D. B., 2005. Three-dimensional electromagnetic modelling and inversion from theory to application, *Surveys in Geophysics*, **26**, 767–799.

Baños, A., 1966. *Dipole radiation in the presence of a conducting half-space*, Pergamon Press, Inc.

Black, N. and Zhdanov, M. S., 2009. Monitoring of hydrocarbon reservoirs using marine CSEM method, *SEG Technical Program Expanded Abstracts*, **28**(1), 850–854.

Börner, R.-U., 2010. Numerical modelling in geo-electromagnetics: Advances and challenges, *Surveys in Geophysics*, **31**(2), 225–245.

Byrd, R. H., Lu, P., and Nocedal, J., 1995. A limited memory algorithm for bound constrained optimization, *SIAM Journal on Scientific and Statistical Computing*, **16**(5), 1190–1208.

Carazzone, J. J., Burtz, O. M., Green, K. E., Pavlov, D. A., and Xia, C., 2005. Three dimensional imaging of marine CSEM data, *SEG Technical Program Expanded Abstracts*, **24**(1), 575–578.

Castagna, J. P. and Backus, M. M., 1993. AVO analysis – tutorial and review, in *Offset-dependent reflectivity – Theory and practice of AVO analysis*, edited by J. P. Castagna and M. M. Backus, pp. 3–36, Society of Exploration Geophysicists, Tulsa, Oklahoma.

Cheesman, S. J., Edwards, R. N., and Chave, A. D., 1987. On the theory of seafloor conductivity mapping using transient electromagnetic systems, *Geophysics*, **52**, 204–217.

Choo, C. K., Rosenquist, M., Rollett, E., Ghaffar, Kamal. A. Abd., Voon, J., and Wong, H. F., 2006. Detecting hydrocarbon reservoir with SeaBed Logging in deepwater Sabah, Malaysia, *SEG Technical Program Expanded Abstracts*, **25**(1), 714–718.

Commer, M. A. and Newman, G. A., 2004. A parallel finite-difference approach for 3D transient electromagnetic modeling with galvanic sources, *Geophysics*, **69**(5), 1192–1202.

Constable, S., 2010. Ten years of marine CSEM for hydrocarbon exploration, *Geophysics*, **75**(5), 75A67–75A81.

Constable, S. and Srnka, L. J., 2007. An introduction to marine controlled-source electromagnetic methods for hydrocarbon exploration, *Geophysics*, **72**(2), WA3–WA12.

Constable, S. C., Parker, R. L., and Parker, C. G., 1987. Occam's inversion: a practical algorithm for generating smoothmodels from EM sounding data, *Geophysics*, **52**, 289–300.

Cox, C. S., 1981. On the electrical conductivity of the oceanic lithosphere, *Physics of the Earth and Planetary Interiors*, **25**, 196–201.

Cox, C. S., Constable, S. C., Chave, A. D., and Webb, S. C., 1986. Controlled source electromagnetic sounding of the oceanic lithosphere, *Nature*, **320**, 52–54.

Dantzig, G. B., 1963. *Linear Programming and Extensions*, Princeton University Press.

Darnet, M., Choo, M. C. K., Plessix, R.-E., Rosenquist, M. L., Yip-Cheong, K., Sims, E., and Voon, J. W. K., 2007. Detecting hydrocarbon reservoirs from CSEM data in complex settings: Application to deepwater Sabah, Malaysia, *Geophysics*, **72**(2), WA97–WA103.

Davydycheva, S. and Rykhlinski, N., 2009. Focused-source EM survey versus time-domain and frequency-domain CSEM, *The Leading Edge*, **28**(8), 944–949.

Davydycheva, S., Rykhlinski, N., and Legeido, P., 2006. Electrical-prospecting method for hydrocarbon search using the induced-polarization effect, *Geophysics*, **71**(4), G179–G189.

de Hoop, A. T., 1995. *Handbook of radiation and scaterring of waves*, Academic Press, London.

Debski, W. and Tarantola, A., 1995. Information on elastic parameters obtained from the amplitudes of reflected waves, *Geophysics*, **60**, 1426–1436.

DeGaetano, A. T., Cameron, M. D., and Wilks, D. S., 2001. Physical simulation of maximum seasonal soil freezing depth in the United States using routine weather observations, *Journal of Applied Meteorology*, **40**, 546–555.

Druskin, V. L. and Knizhnerman, L. A., 1994. Spectral approach to solving three-dimensional MaxwellŠs diffusion equations in the time and frequency domains, *Radio Science*, **29**(4), 937–953.

Druskin, V. L., Knizhnerman, L. A., and Lee, P., 1999. New spectral Lanczos decomposition method for induction modeling in arbitrary 3-D geometry, *Geophysics*, **64**(3), 701–706.

Du Fort, E. C. and Frankel, S. P., 1953. Stability conditions on the numerical treatment of parabolic differential equations, *Mathematical Tables and Other Aids to Computation (Mathematics of Computation)*, **7**, 135–152.

Edwards, N., 2005. Marine controlled source electromagnetics: principles, methodologies, future commercial applications, *Surveys in Geophysics*, **26**, 675–700.

Edwards, R. N. and Chave, A. D., 1986. A transient electric dipole-dipole method for mapping the conductivity of the seafloor, *Geophysics*, **51**, 984–987.

Eidesmo, T., Ellingsrud, S., MacGregor, L. M., Constable, S., Sinha, M. C., Johansen, S., Kong, F. N., and Westerdah, H., 2002. Sea Bed Logging (SBL), a new method for remote and direct identification of hydrocarbon filled layers in deepwater areas, *First Break*, **20**(3), 144–152.

Ellingsrud, S., Eidesmo, T., Johansen, S., Sinha, M. C., and MacGregor, L. M., 2002. Remote sensing of hydrocarbom layers by seabed logging (SBL): Results from a cruise offshore Angola, *The Leading Edge*, **21**(10), 972–982.

Evans, R. L., Constable, S. C., Sinha, M. C., and Cox, C. S., 1991. Upper crustal resistivity structure of the East Pacific Rise near 13°N, *Geophysical Research Letters*, **18**, 1917–1920.

Flosadóttir, Á. H. and Constable, S., 1996. Marine controlled-source electromagnetic sounding 1. Modeling and experimental design, *Journal of Geophysical Research*, **101**(B3), 5507–5517.

Fritsch, F. N. and Carlson, R. E., 1980. Monotone piecewise cubic interpolation, *SIAM Journal on Numerical Analysis*, **17**(2), 238–246.

Giles, M. B., Duta, M. C., Müller, J.-D., and Pierce, N. A., 2003. Algorithm developments for discrete adjoint methods, *AIAA JOURNAL*, **41**(2), 198–205.

Gisolf, D. and Verschuur, E., 2010. *The Principle of Quantitative Acoustical Imaging*, EAGE Publications BV.

Godunov, S. K., 1959. A difference scheme for numerical solution of discontinuous solution of hydrodynamic equations, *Mat. Sbornik*, **47**, 271–306, translated US Joint Publ. Res. Service, JPRS 7226, 1969.

Griffiths, D. J., 1999. *Introduction to electrodynamics*, Prentice Hall, Inc.

Gupta, P. K., Raiche, A. P., and Sugeng, F., 1989. Three-dimensional time-domain electromagnetic modelling using a compact finite-element frequency-stepping method, *Geophysical Journal International*, **96**(3), 457–468.

Gutknecht, H. H., 1993. Variants of BiCGStab for matrices with complex spectrum, *SIAM Journal on Scientific and Statistical Computing*, **14**(5), 1020–1033.

Haber, E., Ascher, U. M., and Oldenburg, D. W., 2002. 3D forward modelling of time domain electromagnetic data, *SEG Technical Program Expanded Abstracts*, **21**(1), 641–644.

Haber, E., Ascher, U. M., and Oldenburg, D. W., 2004. Inversion of 3D electromagnetic data in frequency and time domain using an inexact all-at-once approach, *Geophysics*, **69**(5), 1216–1228.

Haines, G. V. and Jones, A. G., 1988. Logarithmic Fourier transformation, *Geophysical Journal*, **92**, 171–178.

Harten, A., Osher, S., Enquist, B., and Chakravarthy, S. R., 1986. Some results on uniformly high-order accurate essentially non-oscillatory schemes, *Journal of Applied Numerical Mathematics*, **2**, 347–377.

Harten, A., Enquist, B., Osher, S., and Chakravarthy, S. R., 1997. Uniformly high order accurate essentially non-oscillatory schemes, III, *Journal of Computational Physics*, **131**(1), 3–47.

Hayley, K., Bentley, L. R., Gharibi, M., and Nightingale, M., 2007. Low temperature dependence of electrical resistivity: Implications for near surface geophysical monitoring, *Geophysical Research Letters*, **34**, L18402.

He, Z., Dong, W., and Lei, Y., 2007. Joint processing and integrated interpretation of EM and seismic data—an effective method for detecting complicated reservoir targets, *The Leading Egde*, **26**(3), 336–340.

Jackson, J. D., 1999. *Classical Electrodynamics, 3rd edition*, John Wiley & Sons, Inc.

Jönsthövel, T. B., Oosterlee, C. W., and Mulder, W. A., 2006. *Improving multi-grid for 3-D electro-magnetic diffusion on stretched grids*, In: (Wesseling, P., E. Oñate and J. Périaux, eds.) Proceedings, ECCOMAS European Conference on Computational Fluid Dynamics, Egmond aan Zee, The Netherlands, Sept 5–8, 2006, ISBN 90-9020970-0.

King, R. W., Owens, M., and Wu, T., 1992. *Lateral electromagnetic waves: Theory and applications to communications, geophysical exploration, and remote sensing*, Springer-Verlag New York, Inc.

Landrø, M., Veire, H. H., Duffaut, K., and Najjar, N., 2003. Discrimination beetwen pressure and fluid saturation changes from marine multicomponent time-lapse seismic data, *Geophysics*, **68**(5), 1592–1599.

Li, Y. and Constable, S., 2007. 2D marine controlled-source electromagnetic modelling: Part 2 – The effect of bathymetry, *Geophysics*, **72**(2), WA63–WA71.

Lien, M. and Mannseth, T., 2008. Sensitivity study of marine CSEM data for reservoir production monitoring, *Geophysics*, **73**(4), F151–F163.

Lions, J.-L. and Magenes, E., 1972. *Nonhomogeneous boundary value problems and applications*, Springer Verlag, Berlin.

Løseth, L. O., Pedersen, H. M., Ursin, B., Amundsen, L., and Ellingsrud, S., 2006. Low frequency electromagnetic fields in applied geophysics: Waves or diffusion?, *Geophysics*, **71**(4), W29–W40.

Maaø, F. A., 2007. Fast finite-difference time-domain modeling for marine-subsurface electromagnetic problems, *Geophysics*, **72**(2), A19–A23.

Maaø, F. A. and Nguyen, A. K., 2010. Enhanced subsurface response for marine CSEM surveying, *Geophysics*, **75**(3), A7–A10.

MacGregor, L. and Sinha, M., 2000. Use of marine controlled-source electro-magnetic sounding for sub-basalt exploration, *Geophysical Prospecting*, **48**, 1091–1106.

MacGregor, L. M. and Cooper, R., 2010. Unlocking the value of CSEM, *First Break*, **28**(5), 49–52.

MacGregor, L. M., Barker, N., Overton, A., Moody, S., and Bodecott, D., 2007. Derisking exploration prospects using integrated seismic and electromagnetic data — A Falkland Islands case study, *The Leading Egde*, **26**(3), 356–359.

Meju, M. A., Gallardo, L. A., and Mohamed, A. L., 2003. Evidence for correlation of electrical resistivity and seismic velocity in heterogeneous near-surface materials, *Geophysical Research Letters*, **30**(7), 1373–1376.

Mogilatov, V. and Balashov, B., 1996. A new method of geoelectrical prospecting by vertical electric current soundings, *Journal of Applied Geophysics*, **36**(1), 31–41.

Monk, P. and Süli, E., 1994. A convergence analysis of Yee's scheme on nonuniform grids, *SIAM Journal on Numerical Analysis*, **31**(2), 393–412.

Mulder, W. A., 2006. A multigrid solver for 3D electromagnetic diffusion, *Geophysical Prospecting*, **54**(5), 633–649.

Mulder, W. A., 2007. A robust solver for CSEM modelling on stretched grids, in *Proceeding 69th EAGE Conference & Exhibition*, Expanded Abstracts, D036.

Mulder, W. A., 2008. Geophysical modelling of 3D electromagnetic diffusion with multigrid, *Computing and Visualization in Science*, **11**(3), 129–138.

Mulder, W. A. and van Leer, B., 1985. Experiments with implicit upwind methods for the Euler equations, *Journal of Computational Physics*, **59**(2), 232–246.

Mulder, W. A., Wirianto, M., and Slob, E. C., 2008. Time-domain modeling of electromagnetic diffusion with a frequency-domain code, *Geophysics*, **73**(1), F1–F8.

Newman, G. A., Hohmann, G. W., and Anderson, W. L., 1986. Transient electromagnetic response of a three-dimensional body in a layered earth, *Geophysics*, **51**(8), 1608–1627.

Orange, A., Key, K., and Constable, S., 2009. The feasibility of reservoir monitoring using time-lapse masrine CSEM, *Geophysics*, **74**(2), F21–F29.

Oristaglio, M. L. and Hohmann, G. W., 1984. Diffusion of electromagnetic fields into a two-dimensional earth: A finite-difference approach, *Geophysics*, **49**(7), 870–894.

Peck, L. and O'Neill, K., 1997. Frost penetration in soil with an inclusion of sand: dependence on soil moisture content and winter severity, *Canadian Geotechnical Journal*, **34**, 368–383.

Pedersen, L. B., 1988. Some aspects of magnetotelluric field procedures, *Surveys in Geophysics*, **9**, 245–257.

Plessix, R.-E., 2006. A review of the adjoint-state method for computing the gradient of a functional with geophysical applications, *Geophysical Journal International*, **167**, 495–503.

Plessix, R.-E. and Bork, J., 2000. Quantitative estimation of VTI parameters from AVA responses, *Geophysical Prospecting*, **48**, 87–108.

Plessix, R-É. and Mulder, W. A., 2008. Resistivity imaging with controlled-source electromagnetic data: depth and data weighting, *Inverse Problems*, **24**(3), 034012.

Plessix, R.-E., Darnet, M., and Mulder, W. A., 2007. An approach for 3D multi-source multifrequency CSEM modeling, *Geophysics*, **72**(5), SM177–SM184.

Raiche, A. P. and Coggon, J. H., 1975. Analytic Green's tensors for integral equation modelling, *Geophysical journal of the Royal Astronomical Society*, **42**(3), 1035–1038.

Remis, R. F., 1998. *Reduced-order modeling of transient electromagnetic field*, Ph.D. thesis, Delft University of Technology.

Shu, C.-W., 1998. Essentially non-oscillatory and weighted essentially non-oscillatory schemes for hyperbolic conservation laws, in *Advanced Numerical Approximation of Nonlinear Hyperbolic Equations*, edited by A. Quarteroni, pp. 325–432, Springer.

Slob, E., Hunziker, J., and Mulder, W., 2010. Green's tensors for the diffusive electric field in a VTI half-space, *Progress in Electromagnetic Research*, **107**, 1–20.

Spies, B. R., 1983. Recent developments in the use of surface electrical methods for oil and gas exploration in the Soviet Union, *Geophysics*, **48**(8), 1102–1112.

Srnka, L. J., Carazzone, J. J., Eriksen, E. A., and Ephron, M. S., 2006. Remote reservoir resistivity mapping, *The Leading Egde*, **25**(8), 972–975.

Strack, K.-M., 1992. *Exploration with deep transient electromagnetic*, Elsevier, Amsterdam.

Strack, K.-M. and Pandey, P. B., 2007. Exploration with controlled-source electromagnetics under basalt cover in India, *The Leading Egde*, **26**(3), 360–363.

Strack, K.-M and Vozoff, K., 1996. Integrating long-offset transient electromagnetics (LOTEM) with seismics in an exploration environment, *Geophysical Prospecting*, **44**, 997–1017.

Talman, J. D., 1978. Numerical Fourier and Bessel transforms in logarithmic variables, *Journal of Computational Physics*, **29**, 35–48.

Tehrani, A. M. and Slob, E., 2010. Fast and accurate three-dimensional controlled source electromagnetic modelling, *Geophysical Prospecting*, **58**(6), 1133–1146.

van Albada, G. D., van Leer, B., and Roberts, W. W., 1982. A comparative study of computational methods in cosmic gas dynamics, *Astronomy and Astrophysics*, **108**(1), 76–84.

van der Vorst, H. A., 1992. Bi-CGSTAB: a fast and smoothly converging variant of Bi-CG for the solution of non-symmetric linear systems, *SIAM Journal on Scientific and Statistical Computing*, **13**(2), 631–644.

van Leer, B., 1979. Towards the ultimate conservative difference scheme. V. A second-order sequel to Godunov's method, *Journal of Computational Physics*, **32**(1), 101–136.

van Rienen, U., 2001. Frequency domain analysis of waveguides and resonators with FIT on non-orthogonal triangular grids, *Progress in Electromagnetics Research (PIER)*, **32**, 357–381.

Vasco, D. W., Keers, H., Khazanehdari, J., and Cooke, A., 2008. Seismic imaging of reservoir flow properties: Resolving water influx and reservoir permeability, *Geophysics*, **73**(1), O1–O13.

Vogel, C. R., 2002. *Computational Methods for Inverse Problems*, SIAM, Philadelphia.

Wang, T. and Hohmann, G. W., 1993. A finite-difference, time-domain solution for three-dimensional electromagnetic modeling, *Geophysics*, **58**(6), 797–809.

Ward, S. A. and Hohmann, G. W., 1987. Electromagnetic theory for geophysical applications, in *Electromagnetic Methods in Applied Geophysics – Theory, Vol. 1*, edited by M. N. Nabighian, pp. 131–311, Society of Exploration Geophysicists, Tulsa, Oklahoma.

Webb, S. C., Constable, S. C., Cox, C. S., and Deaton, T. K., 1985. A seafloor electric field instrument, *Journal of Geomagnetism and Geoelectricity*, **37**, 1115–1129.

Weiland, T., 1977. A discretization method for the solution of Maxwell's equations for six-components fields, *Electronics and Communications*, **31**(3), 116–120.

Wilt, M. and Alumbaugh, D., 1998. Electromagnetic methods for development and production: State of the art, *The Leading Edge*, **17**(4), 487–490.

Wirianto, M., Mulder, W. A., and Slob, E. C., 2009. A study of land CSEM reservoir monitoring in a complex 3D model, in *71st EAGE Conference & Exhibition SPE EUROPEC 2009, Extended Abstract*, p. X020, EAGE.

Wirianto, M., Mulder, W. A., and Slob, E. C., 2010. A feasibility study of land CSEM reservoir monitoring in a complex 3-D model, *Geophysical Journal International*, **181**(2), 741–755.

Wirianto, M., Mulder, W. A., and Slob, E. C., 2010. A feasibility study of land CSEM reservoir monitoring: the effect of the airwave, *Progress in Electromagnetic Research Symposium Online*, **6**(5), 440–444.

Wirianto, M., Mulder, W. A., and Slob, E. C., 2011. Exploiting the airwave for time-lapse reservoir monitoring with CSEM on land, *Geophysics*, **76**(3), A15–A19.

Wright, D., Ziolkowski, A., and Hobbs, B., 2002. Hydrocarbon detection and monitoring with a multichannel transient electromagnetic (MTEM) survey, *The Leading Edge*, **21**, 852–864.

Yee, K., 1966. Numerical solution of initial boundary value problems involving Maxwell's equations in isotropic media, *IEEE Trans. Antennas and Propagation*, **16**, 302–307.

Yilmaz, O., 2001. *Seismic Data Analysis: Processing, Inversion and Interpretation of Seismic Data (Vols. 1 & 2)*, Society of Exploration Geophysicists, Tulsa Oklahoma.

Zhdanov, M. S., 2002. *Geophysical Inverse Theory and Regularization Problem*, Elsevier, Amsterdam.

Zhdanov, M. S., 2010. Electromagnetic geophysics: Notes from the past and the road ahead, *Geophysics*, **75**(5), 75A49–75A66.

# Summary

## CONTROLLED-SOURCE ELECTROMAGNETICS FOR RESERVOIR MONITORING ON LAND

The main goal of exploration geophysics is to obtain information about the subsurface that is not directly available from surface geological observations. The results are primarily used for finding potential reservoirs that contain commercial quantities of hydrocarbons. A number of possible geophysical methods exists these days to achieve such a goal. One of them is the controlled-source electromagnetic (CSEM) method. CSEM data can provide resistivity maps of the subsurface. Because the bulk resistivity depends on the resistivity of the pore fluid, these maps may enable us to estimate the nature of the fluid content in the reservoir.

The CSEM method exploits electromagnetic fields to remotely characterize the nature of the fluid content in the pores. When a dipole current source is stuck into the ground or placed in the seawater, current flows from one pole to the other through the sediments, creating an electrical field in the subsurface. If highly resistive bodies are present in the subsurface, the electrical field measured at some distance from the source will be larger in amplitude than the field in the absence of these bodies. As hydrocarbon-bearing rock is highly resistive, one may link the larger amplitude to the presence of hydrocarbon reservoirs.

A logical consequence of this phenomenon is that the CSEM method may also be suited for monitoring a hydrocarbon reservoir during production. The reason is that water flooding or steam injection for oil production creates resistivity changes in the reservoir, and if those changes are large enough, we can expect differences in the CSEM response with time-lapse surveys. This consideration led us to further investigate the EM monitoring problem. We tried to answer two questions: are the time-lapse changes in the reservoir detectable, particularly in the presence of noise, and if so, could we use time-lapse signals to locate where the time-lapse changes happened in the subsurface?

In this thesis, we considered land CSEM and found that the resistivity change due to displacement of oil by brine can produce a small but measurable difference in the CSEM response. Interestingly, those response differences at the surface are confined to the lateral extent of resistivity changes in the subsurface, even in the presence of various kinds of repeatability noise. We found a simple and effective method to remove the repeatability noise due to the airwave. Finally, results obtained when incorporating non-linear EM inversion into the monitoring problem suggest that this application of the CSEM method has the potential to

play a significant role in the oil and gas industry.

# Samenvatting

## CONTROLLED-SOURCE ELECTROMAGNETICS FOR RESERVOIR MONITORING ON LAND

Het belangrijkste doel van exploratie geofysica is informatie over de ondergrond te verkrijgen die niet gehaald kan worden uit geologische observaties aan het oppervlak. De resultaten worden voornamelijk gebruikt om potentiële commercieel winbare olie- of gasreserves op te sporen. Er bestaan verschillende geofysische methoden om dit te bereiken. Een van deze methoden is de 'Controlled Source Electromagnetic' (CSEM) methode. Met CSEM data kan een elektrisch weerstandsprofiel van de ondergrond worden verkregen. Omdat de effectieve soortelijke weerstand van het gesteente afhankelijk is van de weerstand van de poriënvloeistof, kunnen deze profielen worden gebruikt om af te leiden om welke soort vloeistof het gaat.

De CSEM method maakt gebruik van elektromagnetische velden om van een afstand de aard van de vloeistofinhoud in de poriën van het ondergrondse gesteente te karakteriseren. Een dipool stroombron in de grond of in het zeewater doet een stroom lopen van de ene naar de andere pool door de sedimenten. Deze stroom veroorzaakt een elektrisch veld in de ondergrond. Als er een lokaal gesteentevolume is met hoge weerstand, dan is het elektrische veld dat op een bepaalde afstand van de bron wordt gemeten groter dan het veld dat gemeten zou zijn bij afwezigheid van dit gesteentevolume. Omdat gesteente dat olie of gas bevat een hoge weerstand heeft kan de grotere amplitude aan het voorkomen van olie en gas worden toegeschreven.

Een logisch gevolg is dat de CSEM methode ook voor de monitoring van een olie- of gasreservoir kan worden gebruikt. De reden hiervoor is dat injecteren van water of stoom voor olieproduktie een verandering in de weerstand tot gevolg heeft. Als deze veranderingen groot genoeg zijn, dan verwachten we ook veranderingen in CSEM metingen gemaakt op verschillende tijdstippen gedurende de produktie. Dit heeft ons er toe gebracht om het CSEM monitoring probleem verder te onderzoeken. We hebben twee vragen proberen te beantwoorden: zijn de verschillen na verloop van tijd meetbaar, in het bijzonder als er ook ruis op de metingen zit, en zo ja, kunnen we de signalen, gemeten op verschillende tijdstippen, gebruiken om te bepalen waar in de ondergrond de veranderingen in de tussenliggende periode hebben plaatsgevonden.

In dit proefschrift beschouwen we CSEM metingen op land en concluderen dat het weerstandsverschil ten gevolge van het verdrijven van olie door brak water

een kleine maar meetbare verandering in de CSEM metingen veroorzaakt. De veranderingen in de aan het oppervlak gemeten waarden vallen samen met de uitgestrektheid van de ondergrondse weerstandsverandering, zelfs als er verstoringen zijn door kleine verschillen bij het herhalen van de metingen. We hebben een eenvoudige en effectieve manier gevonden om verstoringen in het verschilsignaal, ten gevolge van de golf die door de lucht gaat, te onderdrukken. Tot slot suggereren resultaten, verkregen als we een niet-lineaire EM inversieprocedure in het monitoringprobleem introduceren, dat deze toepassing van de CSEM methode mogelijk een belangrijke rol in de olie-en gasindustrie zal kunnen gaan spelen.

# Ringkasan

## CONTROLLED-SOURCE ELECTROMAGNETICS FOR RESERVOIR MONITORING ON LAND

Fokus penelitian geofisika eksplorasi adalah melakukan pemetaan struktur batuan tanpa harus melakukan pembongkaran (*non-destructive method*). Hasilnya dimanfaatkan terutama untuk menentukan lokasi reservoir yang berpotensi mengandung minyak dan gas alam (migas). Sejumlah metoda telah dikembangkan untuk mencapai tujuan tersebut, salah satunya adalah metoda 'controlled-source electromagnetic' (CSEM). Data CSEM dapat memberikan peta resistiviti batuan. Dan, karena nilai resistiviti suatu batuan bergantung pada nilai resistiviti fluida yang terkandung di dalam pori, peta tersebut dapat digunakan untuk memperkirakan jenis fluida yang terkandung dalam reservoir.

Metoda CSEM memanfaatkan medan elektromaknetik untuk mengkarakterisasi fluida dalam pori batuan. Ketika dua kutub arus listrik disambung ke tanah atau dalam air laut, arus listrik akan mengalir dari satu kutub ke kutub lain. Aliran listrik ini kemudian menciptakan medan listrik yang terdistribusi dalam batuan. Ketika terdapat suatu benda yang sangat resistif di dalam lapisan batuan, medan listrik yang terukur pada sensor penerima akan memiliki amplituda yang lebih besar jika dibandingkan ketika tidak terdapat benda tersebut. Karena lapisan yang mengandung hidrokarbon bersifat sangat resistif, kita dapat memanfaatkan fenomena ini untuk menentukan keberadaan reservoir hidrokarbon.

Dengan memanfaatkan prinsip yang sama, CSEM juga dapat diaplikasikan untuk memonitor perubahan komposisi hidrokarbon yang terjadi karena proses produksi. Ide dasar aplikasi ini adalah falta bahwa proses eksploitasi, baik dengan injeksi air atau tekanan uap, dapat menciptakan perubahan resistiviti dalam reservoir, dan jika perubahan tersebut terjadi pada skala yang cukup besar, harapannya, respon terukur pada sensor penerima akan juga berubah. Hal ini melatarbelakangi penelitian untuk menyelidiki lebih lanjut tentang kemungkinan pemanfaatan metoda CSEM untuk memonitor perubahan komposisi hidrokarbon akibat proses eksploitasi. Dua pertanyaan dasar yang mengawali penelitian adalah: apakah perubahan respon CSEM, yang diakibat oleh perubahan komposisi reservoir, dapat terdeteksi terutama dengan kehadiran nois (*noise*), dan jika ya, dapatkah kita menggunakan signal tersebut untuk menentukan lokasi perubahan yang terjadi?

Dalam tesis ini, topik penelitian dibatasi dengan hanya membahas penggunaan metoda CSEM di darat (*Land CSEM*). Berdasarkan hasil-hasil simulasi numerik, teramati bahwa perubahan resistiviti yang terjadi karena proses produksi ternyata

dapat menghasilkan perubahanan pada signal CSEM. Menariknya, perubahan respon tersebut terukur di permukaan secara langsung dapat mengindikasikan posisi lateral perubahan resistiviti yang terjadi. Dalam tesis ini, ditunjukkan bahwa ketika mengaplikasikan inversi non-linear pada masalah monitoring ini, metode CSEM memiliki potensi besar untuk memainkan peran penting dalam industri migas.

# Acknowledgments

This thesis would not have been possible without the help and support from many people. Hence, I would like to take this opportunity to sincerely thank those who contributed — directly or indirectly — to this work.

The first words of gratitude go to my promotor and supervisor, Wim Mulder for giving me the opportunity to carry out this work with him. I am so grateful for having had his great guidance and his encouragement during this research, which made all work become enjoyable and fun. Wim has trustingly given me the necessary freedom, provided feedback and kindly nurtured my skills, which have no doubt improved because of him. In addition, Wim has been like a father to me, who has stood by me during happy and sad moments. I hope to enjoy your friendship for many more years. Thank you Wim!

I thank Evert Slob for great in-depth discussions, encouragement, suggestions and comments, for his critical mindset, and creative ideas, which have enriched and widened my understanding of the topic in this thesis. The discussions I had with Evert were always stimulating and very useful, especially for understanding the practical implications of the theory. Thank you Evert!

I wish to thank all committee members: Prof. Dries Gisolf, Prof. Peter van den Berg, Prof. Rob Arts, Prof. Kees Vuik, and Dr. Mathieu Darnet, for taking the time to read the manuscript and provide me with valuable feedback.

This research was carried out in the Delphi consortium. Therefore, I would like to thank all sponsors of the consortium for their interest and comments they gave at the sponsor meetings as well as for financially supporting this research. In particular, I would like to thank Prof. Guus Berkhout, Prof. Dries Gisolf, Eric Verschuur, and Gerrit Blacquiere for giving me the opportunity to join the Delphi team. I learned many things from them, not only about being a technical expert but also about passion and collaboration in research. The time I spent in Delphi was absolutely unforgettable.

I would like to extend my gratitude to Shell colleagues — Peter van der Sman, René-Edouard Plessix, Mathieu Darnet, Mark Rosenquist, Chris Shen, Xander Campman, Alex Kononov, Herman Darman, Corine Nijland, Arty Bhoendie, Yuanzhong Fan, Liam O'Suilleabhain, David Mejia, Guy Marquis — for the comfortable atmosphere and the pleasant time during my stay as an intern and, now, as a new colleague. I am so grateful for having this unique opportunity.

I owe particular thanks to Wono Setya Budhi and family, who have encouraged me to pursue this doctoral degree. I thank Xander Campman and Christina Dwi Riyanti for listening and helping me with everything I asked them for over

# ABOUT THE AUTHOR

MARWAN WIRIANTO was born on the 30th of August 1982 in Jakarta, Indonesia. He graduated from "SMU Bunda Hati Kudus" in Jakarta in 2000. In the same year, he started his study in Mathematics at the Department of Mathematics of Universitas Katolik Parahyangan Bandung. He obtained his BSc with honors in 2004 for the work on the modelling of crack detection. During this study, he also gave a number of lectures as a teaching assistant. Following the completion of his BSc study, he started his MSc study in Mathematics at the Department of Mathematics of Institut Teknologi Bandung, from where he obtained his MSc degree with honors in June 2006 for the work on the inversion problem of crack detection. After graduation he immediately joined the Department of Mathematics of Universitas Katolik Parahyangan Bandung as a staff member, teaching subjects in the area of real and complex analysis as well as partial differential equations.

In February 2007, Marwan joined Delft University of Technology in the Netherlands as a PhD student. His project entitled "TDEM for land surveys" investigates the possibility of using the CSEM method for monitoring hydrocarbon reservoirs on land. This study is a part of research projects in the Delphi consortium. His research lead to four journal papers and a number of published international conference abstracts. During his PhD time, he visited EM team in Shell International Exploration & Production, Rijswijk, as an intern in January 2010 for three months and in November 2010 for another three months, working on the development of electromagnetic techniques for hydrocarbon exploration.

In November 2011, Marwan joined the EM team in Shell Global Solutions International in Rijswijk, as a research geophysicist.